

**3D Failure Analysis of Fuel Cell Electrodes using Multi-Length  
Scale X-ray Computed Tomography**

**by**

**Anish Pokhrel**

B.Sc., University of Wisconsin-Stout, 2013

Thesis Submitted in Partial Fulfillment of the  
Requirements for the Degree of  
Master of Applied Science

in the

School of Mechatronics Systems Engineering  
Faculty of Applied Sciences

© **Anish Pokhrel**

**SIMON FRASER UNIVERSITY**

**Fall 2016**

All rights reserved.

However, in accordance with the *Copyright Act of Canada*, this work may be reproduced, without authorization, under the conditions for Fair Dealing. Therefore, limited reproduction of this work for the purposes of private study, research, education, satire, parody, criticism, review and news reporting is likely to be in accordance with the law, particularly if cited appropriately.

# Approval

**Name:** Anish Pokhrel  
**Degree:** Master of Applied Science  
**Title:** *3D Failure Analysis of PEM Fuel Cell Electrodes using Multi-Length Scale X-ray Computed Tomography*

## Examining Committee:

**Chair: Dr. Flavio Firmani**  
Lecturer, School of Mechatronics  
Systems Engineering

---

**Dr. Erik Kjeang**  
Senior Supervisor  
Associate Professor, School of  
Mechatronics Systems Engineering

---

**Dr. Woo Soo Kim**  
Supervisor  
Assistant Professor, School of  
Mechatronics Systems Engineering

---

**Dr. Karen Kavanagh**  
Internal Examiner  
Professor, Department of Physics

---

**Date Defended/Approved:** Sep 6, 2016

## **Abstract**

X-ray computed tomography (XCT), a non-destructive technique, is proposed for three-dimensional, multi-length scale characterization of complex failure modes in fuel cell electrodes. Similar to medical CT scanners, laboratory XCT enables low-intensity X-ray imaging of a specimen at different incident angles followed by reconstruction into three-dimensional views. Fuel cell materials are compatible with this technique as they are sufficiently transparent to X-rays. In this thesis, electrode failures are analyzed by comparative tomography data sets for conditioned beginning of test (BOT) and degraded end of test (EOT) membrane electrode assemblies subjected to cathode degradation. Cracks and thickness of the cathode catalyst layer (CCL) are analyzed at the micro length scale, followed by a complementary nano length scale analysis of the fine porous structure. Additionally, a novel image processing based technique is developed for nano scale segregation of pore, ionomer, and Pt/C dominated voxels in the degraded CCL. The results of this work reveal several failure modes of catalyst layers including but not limited to carbon corrosion, Pt agglomeration, and Pt migration. In summary, XCT based multi-length scale analysis enables detailed information needed for comprehensive understanding of the complex failure modes observed in fuel cell electrodes.

**Keywords:** Fuel cell; Electrode; Catalyst layer; Failure analysis; Degradation; Carbon corrosion

## **Dedication**

I would like to dedicate my thesis to my parents, without whose support I would not be where I am today. They supported my decision to study abroad and have helped me in every step of the way. In addition, my father is a Master's degree holder as well and inspired me to follow on his footsteps.

## **Acknowledgements**

Firstly, I would like to thank my senior supervisor Dr. Erik Kjeang for all his support, guidance, patience and persistence towards my research studies. His valuable inputs and directions have certainly made a huge impact on the outcome of my research.

I would also like to thank Dr. Woo Soo Kim for accepting my request to be on my supervisory committee and also in giving invaluable feedbacks on my thesis.

Also, I would like to express my gratitude to Mr. Francesco P. Orfino at FCREL, and Monica Dutta at Ballard Power Systems for their continuous support, guidance, and feedbacks on my research work. In addition, I would like to thank my fellow colleagues Yadvinder Singh, Robin White, Dr. Mehdi Andisheh-Tadbir, Dilip Ramani, Senthil Velan Venkatesan, and Dr. Tom Engl at FCREL for their support and co-operation during my research period.

I would like to thank my friends and family around the globe for all the good times, laughs, and patience whenever I was late to parties and events 😊.

Funding for this research was provided by the Natural Sciences and Engineering Research Council of Canada, Canada Foundation for Innovation, British Columbia Knowledge Development Fund, and Ballard Power Systems through an Automotive Partnership Canada grant. I would also like to thank 4D LABS at Simon Fraser University, Burnaby, Canada in providing technical assistance for FIB/SEM work.

# Table of Contents

Approval.....	ii
Abstract.....	iii
Dedication.....	iv
Acknowledgements.....	v
Table of Contents.....	vi
List of Tables.....	viii
List of Figures.....	ix
List of Acronyms:.....	xiii

<b>Chapter 1. Introduction .....</b>	<b>1</b>
1.1. Fuel cells .....	1
1.2. History of PEM fuel cells.....	1
1.3. PEM Fuel cell technology .....	3
1.3.1. Components of PEM fuel cell.....	5
1.3.1.1 Proton exchange membrane .....	5
1.3.1.2 Catalyst layer .....	6
1.3.1.3 Gas diffusion layers (GDL) .....	8
1.3.1.4 Bipolar plates.....	9
1.3.2 MEA assembly.....	9
1.4. Fuel cells' technical challenges for commercialization .....	10
1.5. Catalyst layer degradation .....	10
1.5.1. Ionomer degradation .....	11
1.5.2. Platinum degradation.....	11
1.5.3. Carbon degradation.....	12
1.5.4. Mechanical degradation.....	13
1.6. In-situ diagnostic tools .....	14
1.7. Catalyst layer failure analysis techniques and challenges.....	15
1.8. A technique to overcome challenges .....	16
1.9. Objective .....	17

<b>Chapter 2. EXPERIMENTAL PROCEDURE.....</b>	<b>19</b>
2.1. Scope of analysis .....	19
2.1.1. Baseline .....	20
2.1.2. Effect of upper potential limit.....	21
2.1.3. Effect of pre-existing cracks.....	21
2.1.4. Effect of catalyst support type.....	21
2.1.5. Effect of ionomer loading amount .....	21
2.2. Sample preparation .....	22
2.3. Morphological characterization techniques .....	23
2.4. Electrochemical diagnostics techniques .....	29

<b>Chapter 3. RESULTS AND DISCUSSION.....</b>	<b>31</b>
3.1. Baseline .....	31

3.1.1.	Micro length scale analysis .....	31
3.1.2.	Nano length scale analysis .....	34
3.2.	Effect of upper potential limit.....	46
3.2.1.	Micro scale analysis .....	46
3.2.2.	Nano scale analysis.....	48
3.3.	Effect of pre-existing cracks.....	54
3.3.1.	Micro scale analysis .....	55
3.3.2.	Nano scale analysis.....	57
3.4.	Effect of catalyst support type.....	62
3.4.1.	Micro scale analysis .....	62
3.4.2.	Nano scale analysis.....	64
3.5.	Effect of ionomer loading amount .....	69
3.5.1.	Micro scale analysis .....	69
3.5.2.	Nano scale analysis.....	71
<b>Chapter 4.</b>	<b>CONCLUSION .....</b>	<b>76</b>
<b>References.....</b>	<b>.....</b>	<b>82</b>

## List of Tables

TABLE 1: THE SCOPE OF ANALYSIS AND APPLIED CATHODE AST FOR MEA'S USED IN THE PRESENTED WORK. ....	20
TABLE 2: DIFFUSIVITY OF OXYGEN AND WATER VAPOR OF A HIGH CRACK CCL AT BOT AND A HIGH POTENTIAL DEGRADED EOT. ....	38
TABLE 3: DIFFUSIVITY OF OXYGEN AND WATER VAPOR AT EDGE AND CENTER OF THE HIGH POTENTIAL DEGRADED HIGH CRACK CCL ISLAND. ....	46
TABLE 4: DIFFUSIVITY OF OXYGEN AND WATER VAPOR IN CCL AT BASELINE BOT AND A LOW POTENTIAL DEGRADED EOT. ....	51
TABLE 5: DIFFUSIVITY OF OXYGEN AND WATER VAPOR OF A LOW CRACK CCL AT BOT AND A 1.3 V DEGRADED LOW CRACK EOT. ....	60
TABLE 6: DIFFUSIVITY OF OXYGEN AND WATER VAPOR OF A HSAC CCL AT BOT AND A DEGRADED HSAC EOT. ....	67
TABLE 7: DIFFUSIVITY OF OXYGEN AND WATER VAPOR OF A HIGH IONOMER CCL AT BOT AND HIGH IONOMER DEGRADED EOT.....	74

## List of Figures

FIGURE 1: BASIC OPERATION OF A PEM FUEL CELL.....	4
FIGURE 2: STRUCTURE OF NAFION [6]. .....	5
FIGURE 3: CATHODE CATALYST LAYER STRUCTURE INDICATING CARBON PARTICLES, PLATINUM PARTICLES, IONOMER FILM AND REMAINING PORE SPACE SANDWICHED BETWEEN PEM AND GDL. ....	8
FIGURE 4 : XCT IMAGE SHOWING CROSS SECTION OF A GDL INDICATING THE SUBSTRATE AND MPL. ....	8
FIGURE 5: A 10 $\mu$ m CUBE FOCUSED ION BEAM (FIB) LIFT OUT CATALYST LAYER SAMPLE PLACED ON THE TIP OF A 0.2 MM WIDE PIN WITH THE HELP OF A MANIPULATOR. ....	23
FIGURE 6: INTERNAL COMPONENTS OF ZEISS XRADIA 520 VERSA XCT SYSTEM. ....	24
FIGURE 7 : INTERNAL COMPONENTS OF ZEISS XRADIA 810 ULTRA XCT SYSTEM. ....	25
FIGURE 8 : GREY SCALE 2D IMAGES OF BASELINE BOT CCL STRUCTURE (A) BEFORE THRESHOLDING (B) AFTER THRESHOLDING AT NANO SCALE, WHERE WHITES ARE SOLIDS AND BLACKS ARE PORES.....	26
FIGURE 9: 3D RENDERING OF CATHODE CATALYST LAYERS AT A) BOT AND B) EOT AND 2D VIRTUAL CROSS-SECTIONS OF (C) BOT MEA AND (D) EOT MEA SHOWING THE EFFECTS OF CATHODE DEGRADATION.....	32
FIGURE 10: NORMALIZED CUMULATIVE CRACK AREA OF THE CATHODE CATALYST LAYER CRACK WIDTH IN THE BASELINE BOT AND EOT MEAs.....	33
FIGURE 11 : FIB LIFT OUT OF AN EOT CCL SAMPLE USING A MANIPULATOR FROM THE CENTER OF THE ISLAND, ALSO INDICATING CCL CRACK. ....	34
FIGURE 12: 3D AND 2D CROSS SECTIONAL REPRESENTATION OF THE CCL STRUCTURE INDICATING THE IMAGING LOCATION FROM THE PEM AND GDL INTERFACES AT BOT (A) & (C) AND AT EOT (B) & (D). 2D TEM IMAGES OF THE CATHODE CATALYST LAYER AT (E) BOT AND (F) EOT, WHERE BLACK IS PORE AND WHITE IS SOLID. ....	36
FIGURE 13: CATHODE CATALYST LAYER PORE SIZE DISTRIBUTION AT BOT AND EOT, INDICATING LARGER PORES AT EOT. ....	37
FIGURE 14: FUEL CELL POLARIZATION CURVES MEASURED IN SITU AT THE BOT AND EOT STATES INDICATING ACTIVATION, OHMIC AND MASS TRANSPORT LOSS REGIONS AT EOT.....	39
FIGURE 15: GREY SCALE HISTOGRAM OF THE CATHODE CATALYST LAYER PHASE SEGMENTATION WITH X-AXIS REPRESENTING GREY SCALE VALUES AND Y-AXIS REPRESENTING FREQUENCY.	

AIR PORTION IS REPRESENTED BY BLACK, IONOMER DOMINATED REGION REPRESENTED BY BLUE, AND Pt/C DOMINATED REGION IS REPRESENTED BY YELLOW.....	40
FIGURE 16: 3D STRUCTURE OF CATHODE CATALYST LAYER AT (A) BOT AND (B) EOT SHOWING Pt/C DOMINATED REGION AS YELLOW, IONOMER DOMINATED REGION AS BLUE, AND PORES AS BLACK. 2D IMAGE HIGHLIGHTING THE IONOMER DOMINANT PHASE ONLY FROM XCT AT (C) BOT, (D) EOT, AND FLUORINE ELEMENTAL MAPPING OBTAINED FROM EDX AT (E) BOT, (F) EOT INDICATING HIGHEST FLUORINE CONCENTRATION WITH RED FOLLOWED BY GREEN AND BLUE, AND 3D STRUCTURE HIGHLIGHTING THE Pt/C DOMINANT PHASE ONLY AT (G) BOT, AND (H) EOT.....	43
FIGURE 17: A FIB LIFT OUT OF A HIGH POTENTIAL DEGRADED CCL SAMPLE AT THE EDGE OF THE ISLAND.....	44
FIGURE 18: CATHODE CATALYST LAYER PORE SIZE DISTRIBUTION AT EDGE VS CENTER OF A HIGH POTENTIAL DEGRADED CCL ISLAND.....	45
FIGURE 19: 3D RENDERING OF 1.2 V DEGRADED CATHODE CATALYST LAYER AT A) AND 2D VIRTUAL CROSS-SECTIONS OF 1.2 V DEGRADED EOT MEA AT (B) SHOWING THE EFFECTS OF CATHODE DEGRADATION.....	47
FIGURE 20: NORMALIZED CUMULATIVE CRACK SURFACE AREA OF THE CATHODE CATALYST LAYER CRACK WIDTH IN BASELINE BOT, 1.2 V DEGRADED EOT, AND 1.3 V DEGRADED EOT.....	48
FIGURE 21: A 3D STRUCTURE OF THE 1.2 V POTENTIAL DEGRADED EOT CCL INDICATING PEM AND GDL INTERFACES AT (A) AND A 2D REPRESENTATION OF THE CCL AT (B) SHOWING THE EFFECT OF DEGRADATION.....	49
FIGURE 22: CATHODE CATALYST LAYER PORE SIZE DISTRIBUTION AT BASELINE BOT, 1.2 V DEGRADED EOT, AND 1.3 V DEGRADED EOT.....	50
FIGURE 23: A FUEL CELL POLARIZATION CURVE FOR BASELINE BOT, 1.2 V DEGRADED EOT, AND 1.3 V DEGRADED EOT MEA'S SHOWING HIGHER VOLTAGE DROP AT 1.3 V EOT IN COMPARISON TO 1.2 V EOT.....	52
FIGURE 24: A 1.2 V DEGRADED 3D PHASE SEGMENTED CCL STRUCTURE AT (A), 2D REPRESENTATION OF THE STRUCTURE INDICATING IMAGING LOCATION FROM THE PEM AND GDL INTERFACES AT (B), 2D REPRESENTATION OF THE IONOMER DOMINATED PHASE AT (C), AND 2D REPRESENTATION OF THE Pt/C DOMINATED PHASE AT (D), WHERE BLUE IS IONOMER DOMINATED, YELLOW IS Pt/C DOMINATED, AND BLACK IS PORES.....	53
FIGURE 25: 3D RENDERING OF CATHODE CATALYST LAYERS AT A) LOW CRACK BOT MEA, B) LOW CRACK DEGRADED EOT MEA AND 2D VIRTUAL CROSS-SECTIONS OF (C) LOW CRACK BOT	

MEA AND (D) LOW CRACK DEGRADED EOT MEA SHOWING THE EFFECTS OF CATHODE CORROSION. ....	55
FIGURE 26: NORMALIZED CUMULATIVE CRACK SURFACE AREA OF THE CATHODE CATALYST LAYER CRACK WIDTH IN LOW CRACK BOT AND LOW CRACK DEGRADED EOT MEA. ....	56
FIGURE 27: A 3D STRUCTURE OF THE CCL INDICATING THE PEM & GDL INTERFACES, POROSITY MEASUREMENT LOCATIONS, AND POROSITY CHART AT LOW CRACK BOT (A) & (C) AND AT LOW CRACK DEGRADED EOT (B) & (D). PITM BAND (INDICATED BY BLUE BOX) AT (E) IS FORMED IN THE MEMBRANE OF THE LOW CRACK DEGRADED EOT CCL AFTER CATALYST LAYER DEGRADATION. ....	58
FIGURE 28: CATHODE CATALYST LAYER PORE SIZE DISTRIBUTION AT LOW CRACK BOT AND 1.3 V DEGRADED LOW CRACK EOT. ....	59
FIGURE 29: A FUEL CELL POLARIZATION CURVE COMPARISON AT LOW CRACK BOT AND LOW CRACK DEGRADED EOT SHOWING THE EFFECT OF REDUCTION IN CCL ECSA AND DIFFUSIVITY ON THE PERFORMANCE OF THE FUEL CELL.....	61
FIGURE 30: 3D RENDERING OF CATHODE CATALYST LAYERS AT A) HSAC BOT MEA, B) HSAC DEGRADED EOT MEA AND 2D VIRTUAL CROSS-SECTIONS OF (C) HSAC BOT MEA AND (D) HSAC DEGRADED EOT MEA SHOWING THE EFFECTS OF CATHODE CORROSION. ....	63
FIGURE 31: NORMALIZED CUMULATIVE CRACK AREA OF THE CATHODE CATALYST LAYER CRACK WIDTH IN HSAC BOT AND HSAC DEGRADED EOT MEA SAMPLE. ....	64
FIGURE 32: FIB LIFT OUT USING A MANIPULATOR FROM THE CENTER OF CCL ISLAND FOR HSAC DEGRADED EOT. ....	65
FIGURE 33: A 3D STRUCTURE OF CCL SUB DOMAIN INDICATING THE PEM AND GDL INTERFACES AT (A) HSAC BOT AND AT (B) HSAC DEGRADED EOT. ....	66
FIGURE 34: CATHODE CATALYST LAYER PORE SIZE DISTRIBUTION AT HSAC BOT AND LOW POTENTIAL DEGRADED HSAC EOT SHOWING LARGER PORES AT EOT.....	67
FIGURE 35: A FUEL CELL POLARIZATION CURVE AT HSAC BOT AND DEGRADED HSAC EOT SHOWING THE EFFECT OF COLLAPSING OF THE CL STRUCTURE ON THE PERFORMANCE OF FUEL CELL. ....	68
FIGURE 36: 3D RENDERING OF CATHODE CATALYST LAYERS AT A) HIGH IONOMER BOT SAMPLE, B) HIGH IONOMER DEGRADED EOT SAMPLE AND 2D VIRTUAL CROSS-SECTIONS OF (C) HIGH IONOMER BOT MEA AND (D) HIGH IONOMER DEGRADED EOT MEA SHOWING THE EFFECTS OF CATHODE CORROSION. ....	70

FIGURE 37: NORMALIZED CUMULATIVE CRACK SURFACE AREA OF THE CATHODE CATALYST LAYER CRACK WIDTH IN HIGH IONOMER BOT AND HIGH IONOMER DEGRADED EOT MEA.....	70
FIGURE 38: FIB LIFT OUT SAMPLE OF HIGH IONOMER BOT CCL FROM THE CENTER OF CCL ISLAND. ....	71
FIGURE 39: A 3D STRUCTURE OF THE CCL INDICATING THE PEM AND GDL INTERFACES AND POROSITY MEASUREMENT LOCATION AT HIGH IONOMER BOT (A) & (C) AND AT HIGH IONOMER DEGRADED EOT (B) & (D).....	72
FIGURE 40: PORE SIZE DISTRIBUTION OF BOT CCL AND 1.2 V DEGRADED EOT CCL WITH HIGH IONOMER LOADING. ....	73
FIGURE 41: A FUEL CELL POLARIZATION CURVE AT HIGH IONOMER BOT MEA AND HIGH IONOMER DEGRADED EOT MEA SHOWING THE EFFECT OF REDUCTION IN CCL ECSA ON THE PERFORMANCE OF THE FUEL CELL. ....	74

## List of Acronyms:

**ACL**-Anode catalyst layer

**AST**-Accelerated stress test

**BOT**-Beginning of life

**CCL**-Cathode catalyst layer

**CCM**-Catalyst coated membrane

**CL**-Catalyst layer

**ECSA**-Electrochemical surface area

**EOT**- End of life

**FIB**-Focused ion beam

**FoV**-Field of view

**GDL**-Gas diffusion layer

**HRES**-High resolution

**LSAC**-Lower surface area carbon

**MEA**-Membrane electrode assembly

**MIP**-Mercury intrusion porosimetry

**MPL**-Micro porous layer

**MSAC**-Medium surface area carbon

**OCV**-Open circuit voltage

**PEM**-Proton exchange membrane

**PITM**-Platinum in the membrane

**PSD**-Pore size distribution

**Pt/C**-Platinum and carbon

**ROI**-Region of Interest

**SEM**-Scanning electron microscope

**SFU**-Simon Fraser University

**STXM**- Scanning transmission x-ray microscopy

**XCT**- X-ray computed tomography

# Chapter 1.

## Introduction

### 1.1. Fuel cells

A fuel cell is an electro-chemical cell or device that converts chemical energy stored in fuels such as hydrogen and supplied oxidant into electrical energy. A fuel cell works in a similar way as a battery, except it has a continuous flow of fuel and oxidant [1]. In the case of a battery, the reactants are enclosed and slowly depleted, which causes the battery to discharge. In other words, a battery with flow channels for a continuous supply of fuel and oxidant in and by-product out would mimic an operating fuel cell [1]. The five most common types of fuel cells are polymer electrolyte membrane fuel cells (PEM fuel cells or PEMFCs), alkaline fuel cells (AFCs), phosphoric acid fuel cells (PAFCs), molten carbonate fuel cells (MCFCs) and solid oxide fuel cells (SOFCs). However, low temperature operation, high power density, and a more compact system makes PEM fuel cells ideal for smaller scale applications such as transportation, stationary power stations, and portable devices, and is becoming increasingly popular and outpacing other types of fuel cells.

### 1.2. History of PEM fuel cells

Fuel cells history can be dated back to 1839, when a physicist named Sir William Grove found that electrolysis could be performed in reverse with the help of a catalyst to produce electricity [2]. Three years later he developed a stack of 50 fuel cells and named it “gaseous

voltaic battery” and is thus recognized as “the father of the fuel cell”. However, according to the Department of Energy of the United States [3], German chemist named Christian Friedrich Schonbein conducted the first scientific research on the phenomenon of a fuel cell in 1838. In 1950, Francis T. Bacon, an Englishman developed a 40-cell stack which was capable of producing 5 KW of power. He developed a fuel cell during the World War II to be used in submarines of the Royal Navy. The invention of a PEM fuel cell is dated back to the early 1960s at General Electric (GE) by Thomas Grubb and Leonard Niedrach, who started using sulfonated polystyrene membranes, but later replaced them by Nafion® membranes which proved to be superior in performance and durability. A \$1.1 million in funding was provided by the U.S. Army for GE’s PEM fuel cell program which led to work with the newly formed National Aeronautics and Space Administration (NASA) and the development of PEM fuel cells that powered several Gemini missions. In 1970s and 1980s, Los Alamos National Laboratory, with a very limited funding was the sole organization in the United States working on PEM fuel cell research and development. Later in 1983, Ballard Power Systems received the first Canadian government grant for PEM fuel cell research. The PEM fuel cell related patents owned by GE had expired by then which opened up gates for other companies to use the technology to their advantage.

In the late 2000s, hydrogen and natural gas fuelled PEM fuel cells units were sold in parts of Africa and India, providing primary backup power to mobile phone masts. Later in 2007, thousands of PEM fuel cells were commercialized in leisure applications such as boats and campervans with written warranties and service capability. Currently, a lot of universities and institutions all over the world are involved in PEM fuel cell research and development. In the past 30 years, fuel cell research and development has escalated over time as significant number of fuel cell related patents have been registered [1].

A lot of new and key innovations such as low platinum catalyst loading, novel membranes, newer bipolar plates, more stable catalyst support has resulted in lower cost,

improved durability, and higher fuel cell efficiency which is ultimately making the applications of PEM fuel cells more practical. The commercialization of PEM fuel cell technology in cars and buses came closer to reality when a vehicle fuelling infrastructure in the form of a hydrogen highway project was proposed in British Columbia, Canada in March 13, 2007. The Canadian Prime Minister, Stephen Harper announced a funding of almost \$200 million CAD for environmental projects in B.C. including the hydrogen highway. A fleet of 20 fuel cell buses were operated during the 2010 Olympic and Paralympic winter games in Whistler and continued running for four years. While in Germany, as of 2015, there were 18 public hydrogen fuelling stations under the clean energy partnership (CEP) project umbrella [4]. In addition, a private sector initiative, named H2 Mobility announced that by 2023, it will expand the network of hydrogen fuelling stations in Germany from 18 to 400.

### **1.3. PEM Fuel cell technology**

A PEM fuel cell consists of a proton exchange membrane (PEM), catalyst layers (CL), and gas diffusion layers (GDL) sandwiched between bipolar plates. The PEM is at the heart of a fuel cell and is mostly impermeable to gases but conducts protons, hence the name proton exchange membrane. The membrane, acting as an electrolyte, is squeezed between two porous and electrically conductive electrodes, typically made of carbon cloth or carbon fibers, called as GDL. In between the PEM and GDL, a layer with catalyst particles, typically platinum supported on carbon is present, and is the catalyst layer. A typical schematic and basic principle of a PEM fuel cell operation is shown in Figure 1.

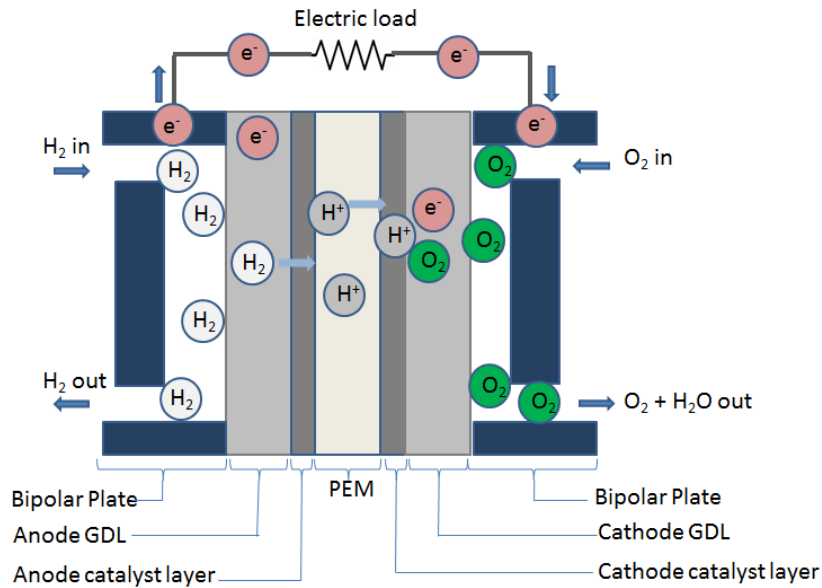
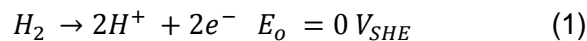


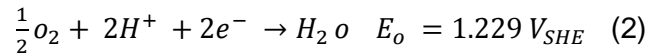
**Figure 1: Basic operation of a PEM fuel cell.**

The electrochemical reactions take place in the catalyst layers; which consists of a collection of agglomerates [5] composed of carbon supported platinum particles surrounded by ionomer (proton conducting polymer) and interstitial pores. Hydrogen oxidation reaction (HOR) occurs at the anode catalyst layer when hydrogen flowing through the pores comes in contact with the platinum catalyst surface. The hydrogen gas is then dissociated into hydrogen ions as shown by Equation 1, which diffuses through the polymer electrolyte membrane to the cathode, whereas the electrons reach the cathode through an external circuit. At the cathode, an oxygen reduction reaction (ORR) occurs when oxygen diffuses through the catalyst layer to the platinum reaction sites and dissociates into ions and reacts with the hydrogen ions and the electrons to form water as shown by Equation 2. The product water diffuses back through the pores and is transported out of the catalyst layer by evaporation and capillary action [5]

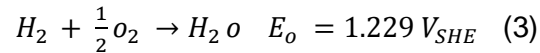
**Hydrogen Oxidation Reaction (HOR):**



### Oxygen Reduction Reaction (ORR):



### Overall Reaction:



## 1.3.1. Components of PEM fuel cell

### 1.3.1.1 Proton exchange membrane

The membrane is the core component of PEM fuel cells, which acts as an electrolyte and separates the anode and cathode side of the membrane electrode assembly (MEA), and prevents mixing of the two gases or any electrical shorts. It is impermeable to gases whereas it conducts protons to the reaction sites in the cathode catalyst layer through its sulfonic groups. An ideal PEM should have excellent proton conductivity, chemical and thermal stability, strength, flexibility, low gas permeability, low water drag, low cost, and good availability [2]. The membranes are usually polymers which are modified to include ions, such as sulfonic groups. The most widely used membranes today is Nafion® (

Figure 2), manufactured by a company named DuPont.

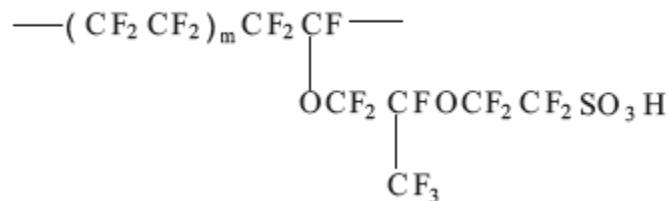


Figure 2: Structure of Nafion [6].

The Nafion polymer has an aliphatic perfluorinated backbone with ether-linked side chains ending in sulfonate cation exchange sites. It is a copolymer of tetrafluoroethylene and sulfonyl fluoride vinyl ether with a semi-crystalline structure [2]. The structure of Nafion has a close resemblance to Teflon and provides an extended stability in oxidative or reductive conditions. When the Nafion is dry, it has reverse micelle morphology which consists of dispersed ionic clusters in a continuous tetrafluoroethylene phase [2]. In a fuel cell, when the membrane absorbs water, the ionic domain swells and forms proton conducting channels. The conductivity of protons depends on the water content; however as the water content increases the concentration of protons diminishes.

#### **1.3.1.2 Catalyst layer**

The catalyst layer is where the electrochemical reactions take place. The carbon supported platinum particles in the catalyst layer are typically embedded in the ionomer, which helps in proton and water transport to and from the active sites respectively. The pore size and structure of the catalyst layer are critically important for adequate mass transport of reactant gases and product water to and from the active sites. The pore size distribution depends on the fabrication process and catalyst layer composition. For example, a more uniform pore distribution has been achieved for the screen printing method which disperses catalyst agglomerates more uniformly than the spraying method, contributing to an improved mass transport of fuel gases and by-product water [7]. It has been shown that the addition of ethylene glycol to the catalyst slurry formulation helps in enhancing the formation of secondary pores in the catalyst layer, which improves performance [8]. Mercury intrusion porosimetry (MIP) is a widely used tool to determine pores size distribution and porosity in the catalyst layer [9] [10] within a pressurized chamber by forcing mercury into the pores of porous catalyst structure. The Washburn equation (Equation 4) is used to relate the applied pressure to the pore diameter using the non-wetting property of mercury.

$$d = -\left(\frac{1}{p}\right) 4\sigma \cos\theta \quad (4)$$

where  $d$  is the pore diameter,  $p$  is the applied pressure,  $\sigma$  is the surface tension, and  $\theta$  is the contact angle. Hence, the volume of mercury penetrated in the pores is measured directly as a function of applied pressure [9].

Platinum is the most widely used catalyst and is supported by carbon based powder such as Vulcan XC72<sup>®</sup>. The platinum catalysts are small particles circa 5 nm dispersed around the surface of larger carbon particles so that a high proportion of surface area will be in contact with the reactant. In the past, platinum catalyst was loaded onto carbon support at 28 mg/cm<sup>2</sup> making catalyst layer very costly but recently with research and development, the Pt loading is down to about 0.4 mg/cm<sup>2</sup> [11]. The catalyst layer also consists of recast Nafion ionomers which acts as a binder and also a proton transport conductor. Some of the catalyst layer also contains PTFE impregnation which is hydrophobic and helps in removing water from the active sites. The ionomers are typically combined in a dispersing solvent with carbon supported Pt catalyst and are deposited onto a membrane or a gas diffusion layer forming a porous structure as shown by Figure 3. The carbon support provides the electronic pathways for electrical current flow to and from the active sites; the ionomer provides the pathways for transport of protons and the pores facilitate the transport of gases and water in and out of the active sites.

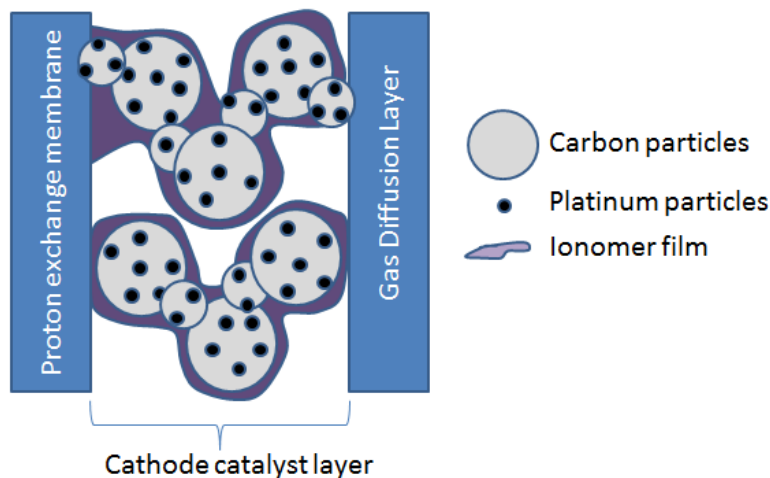


**Figure 3: Cathode catalyst layer structure indicating carbon particles, platinum particles, ionomer film and remaining pore space sandwiched between PEM and GDL.**

### 1.3.1.3 Gas diffusion layers (GDL)

The GDL is a carbon-based dual layer composed of macro-porous substrate containing carbon fibers, binders, PTFE, and a thin micro-porous layer (MPL) made up of carbon nanoparticles and PTFE as shown in Figure 4. GDL's are the pathways for reactant gases such as H<sub>2</sub>, Air/O<sub>2</sub> into the catalyst layer and water out of the catalyst layer. PTFE, also known as Teflon by DuPont, is pre coated in the GDL making it hydrophobic so that the water can escape out. The GDL also acts as a structural support and is an electrical conductor between the catalyst layer and current collector plates.

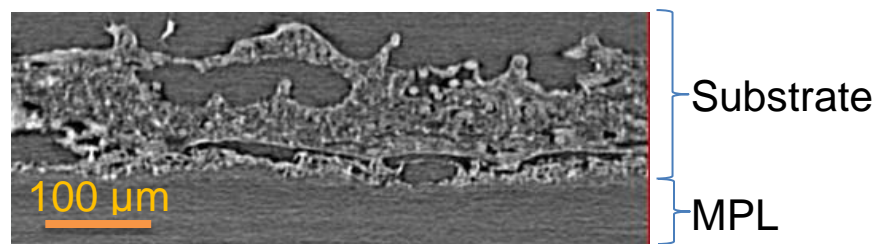


**Figure 4 : XCT image showing cross section of a GDL indicating the substrate and MPL.**

The smaller pore sizes and hydrophobic nature of the MPL aids in liquid water management in the fuel cell by not letting the water accumulate at the CL-GDL interface. The MPL also forces the water to permeate into the membrane by capillary pressure through the hydrophilic pores in the catalyst layer, which helps in membrane hydration and thus proton conductivity. In addition, MPL reduces the overall contact resistance between the GDL substrate and the catalyst layer, enhancing the electrical and thermal conductivity [12] .

#### **1.3.1.4 Bipolar plates**

Bipolar plates also known as current collectors are graphite or metal based plates, which delivers reactant gases to the gas diffusion electrodes via flow channels, electrically connect the cells, facilitate the heat from the cells to the cooling zone, and mechanically support the MEA structure. Since bipolar plates operate in constant contact with the acidic water generated in the fuel cell, they have to be chemically stable and corrosion resistant. In addition, the material used in bipolar plates must be able to withstand a temperature of 80°C or more. An example of how a bipolar plate is used in PEM fuel cells is shown in Figure 1.

#### **1.3.2 MEA assembly**

An MEA can be assembled in two ways, applying catalyst layer to the GDL followed by addition of the membrane, and is called gas diffusion electrode (GDE) based MEA or applying catalyst layer to the membrane followed by adding GDL, which is called catalyst coated membrane (CCM) based MEA. The CCM based MEA offers higher performance than the GDE based MEA due to better interfacial properties [13] [14]. The direct catalyst coating method used for manufacturing CCM is simpler and more efficient than the indirect coating method used for manufacturing CCM which involves decal transfer, coating the catalyst on a substrate and transferring it to the membrane. However, coating catalyst on the membrane directly could cause deformation and cracks in the catalyst layer since membrane can swell during the process. In a study, membrane was soaked in ethylene glycol first and then catalyst slurry was sprayed on the top [15], which showed a reduction of resultant stress on the catalyst layer. Catalyst coating can be done using spraying, screen printing, or rolling techniques. Finally, using a hot pressing technique, GDL is added to the CCM. The membrane will dry out during the hot pressing technique but will be rehydrated adequately after humidified gases are passed in the fuel cell stack during conditioning [16]. A good contact between the GDL, catalyst layer,

and the membrane is desired for low contact resistance and maximum catalyst utilization during operation of the cell.

## **1.4. Fuel cells' technical challenges for commercialization**

Currently, the high cost of fuel cells, currently estimated at \$200 per kW [17] is one of the major obstacles in the way of commercialization. According to US Department of Energy (DOE), a target of \$40 per kW is deemed appropriate for fuel cells to be competitive for automotive application [18]. The platinum based electrodes and bipolar plates are the most expensive part of a fuel cell stack. Thus, a substantial breakthrough in the reduction of cost for these components is desirable to help achieve the DOE target.

The commercial durability requirements of polymer electrolyte fuel cells vary significantly and range from 8,000 hours for cars to 40,000 hours of continuous operation for stationary applications [18] [19]. Currently, achieving fuel cell lifetime targets is a challenge in part due to electrode and membrane degradation and associated fuel cell performance losses over time. This lifetime duration can be improved by understanding degradation mechanisms, identifying failure modes, and applying mitigation strategies.

## **1.5. Catalyst layer degradation**

Reducing fuel cell electrode degradation is a critical need for longer term commercialization, requiring an in-depth study, and hence will be pursued in the presented work. Catalyst layer degradation can be summarized as a degradation of the individual solid phases of the catalyst layers; i.e. ionomer, platinum, and carbon. In order to obtain a comprehensive understanding of catalyst layer degradation, it is very important to categorize and study them independently.

### **1.5.1. Ionomer degradation**

The ionomer plays an important role in the catalyst layer by transporting protons and providing pathways for removal of water out of the active sites. The distribution of ionomer and its content after degradation can directly impact transport properties of the catalyst layer, affecting fuel cell performance. The ionomer degradation in the catalyst layer is caused by hydrogen peroxide, hydroxyl radicals and other contaminants by attacking the perfluorosulfonic acid (PFSA). The presence of platinum close to the ionomer will scavenge some of the contaminants hence ionomer contamination is likely to be less significant than in the membrane [20]. However, the generation of water in the ionomer might cause the ionomer to degrade more than the membrane [21].

### **1.5.2. Platinum degradation**

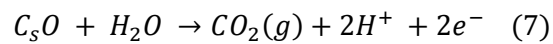
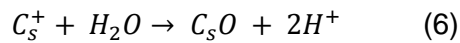
The platinum degradation in the catalyst layers is caused by platinum agglomeration and particle growth, platinum loss and migration, and contamination of the active sites [2]. Platinum agglomeration, a failure mechanism in the catalyst layer, occurs after platinum particles get detached from the carbon support due to carbon corrosion and combine to form larger platinum particles to reduce the high surface energy [22]. Additionally, some of the smaller platinum particles dissolve, diffuse, and redeposit into larger particles via Ostwald ripening [23] [24], resulting in a reduced electrochemical surface area (ECSA) which causes a fuel cell voltage drop.

Some of the dissolved platinum in the catalyst layer also migrates to the PEM where it is deposited in the form of a platinum band and is described in the literature as platinum in the membrane (PITM) [25]. The redistribution of platinum particles in the membrane involves a process of platinum dissolution, formation of  $Pt^{Z+}$  species, migration into the membrane, and reduction of Pt particles by  $H_2$  [22]. In contrast to fuel cell voltage drop from the migrated

platinum particles, PITM has been observed to have a positive impact on membrane durability by aiding in removal of H<sub>2</sub>O<sub>2</sub> and converting cross over gases into water [25]. Contaminants present in the fuel and/or air such as: CO, CH<sub>4</sub>, CO<sub>2</sub>, NH<sub>3</sub>, NO, and system derived contaminants (metallic ions or silicon) can cause platinum surface poisoning; for example, by forming a CO layer limiting the adsorption of H<sub>2</sub> onto the active Pt area and decreasing the activity of the catalyst layer [22].

### 1.5.3. Carbon degradation

The carbon support in the catalyst layers, over time, suffers from severe microstructural degradation. When PEM fuel cells are operated at high temperatures for a prolonged period, at high water content, low pH, and high oxygen concentration, the carbon support is prone to degrade both physically and chemically [22], giving rise to carbon oxidation or carbon corrosion, a dominant catalyst layer failure mechanism. The carbon oxidation can be incomplete as shown by equations 5, and 6 forming carbon oxygen species, or can be complete as shown by equation 7 forming carbon dioxide [26].



Among factors such as potential, relative humidity, and carbon surface area, higher potential is the most aggressive factor to induce carbon corrosion. For example, significant surface oxidation of Vulcan carbon support has been observed at potentials greater than 1.0 V at room temperature [27]. Carbon corrosion can also occur during normal operating potentials, at the air and hydrogen boundary, and from fuel starvation at the anode. However, carbon corrosion is minimal under normal operating potential. During the fuel cell start up and shut down cycle, the presence of oxygen at the anode due to gas crossover through the membrane

and the formation of oxygen and hydrogen boundary at anode will create a carbon oxidation reaction at the cathode resulting in carbon corrosion [22]. Finally, fuel starvation at the anode increases the anode potential to a higher value than the cathode thus inducing carbon corrosion as well [28].

In literature, carbon corrosion has been investigated using focused ion beam and scanning electron microscopy (FIB/SEM) by studying the changes in pore structure and porosity after a MEA was subjected to potential cycling (24,000 cycles, 0.6 V-OCV) and start/stop cycling (1,000 cycles) stress tests [29]. The potential cycled cathode maintained the initial fuel cell performance [29], whereas the start/stop cycling showed a significant amount of carbon corrosion leading to a poor fuel cell performance. In a separate study, substantial thinning of the cathode catalyst layer was seen after an MEA was subjected to a higher upper potential cycling [30]. It was observed that the primary failure mechanism shifted from platinum dissolution to carbon corrosion at potentials higher than 1.2 V.

#### **1.5.4. Mechanical degradation**

Mechanical damage also causes catalyst layer degradation and can appear as flaws or mud-cracks, and delamination between the carbon-catalyst agglomerate and the electrolyte. The humidity and temperature cycles in the fuel cells due to its operating conditions results in mechanical damage or degradation in the catalyst layer [31]. The degradation is more severe during frequent start up and shutdown of fuel cells since the frequency of humidity and temperature cycle is relatively higher, resulting in earlier delamination between the Nafion and Pt/C agglomerate, and forming cracks [31]. The cracks on the catalyst surface can lead to increased resistance within catalyst layers, flooded areas, and areas susceptible to catalyst erosion [32]. A previous research study has shown that catalyst layers with higher catalyst crack area show higher carbon corrosion degradation [33].

## 1.6. In-situ diagnostic tools

Polarization curve and cyclic voltammetry are frequently used electrochemical methods for catalyst layer failure analysis and degradation diagnostics [34][35]. A polarization curve is used to describe fuel cell performance and observe voltage decay as a function of current. A polarization curve is obtained by recording the current as a function of cell potential or vice-versa. The polarization curve for a fuel cell has mostly three major regions; activation polarization at low current densities, ohmic polarization at intermediate current densities, and finally mass transport polarization at high current densities [36]. At low current densities, the majority of the voltage loss is due to the slow kinetics of the ORR, while at intermediate current densities, the voltage loss is caused by ohmic resistance due to resistance in the flow of ions through the membrane and electrons through the electrode. And lastly, at high current densities, mass transport effect is dominant due to poor transport of the reactant gases through the pore structure of GDLs and catalyst layers, which can be attributed to water flooding [37] [38]. Water flooding is caused due to excessive buildup of water from the ORR at cathode, and is generally seen at higher current densities. In addition to mass transport losses by hindering the flow of gases into the active catalyst sites, water flooding could also aid in carbon corrosion. However, occurrence of water flooding and high cathode potential at the same time is less likely to happen.

Cyclic voltammetry (CV) is an electrochemical technique used to characterize electrochemical reaction and electrode surface adsorption. CV is commonly used to measure electrochemical surface area (ECSA) of catalyst layers [39]. It is done so by first sweeping the cell potential to low and high back and forth with a fixed sweep rate while recording the current. A current vs voltage plot is obtained, where area under the hydrogen adsorption peak is used to calculate the ECSA of the electrode. Electrochemical impedance spectroscopy (EIS) is used in

electrochemistry to study complex phenomena such as corrosion or kinetics of electrode reaction [34]. In fuel cell, EIS is used to differentiate between the contributions of the interfacial charge transfer and the mass transport resistances in the catalyst layers and diffusion layers. EIS is used to calculate the double layer capacitance, which appears at the interface of conductive electrode and an electrolyte. In electrochemical system such as fuel cells, double layer charge forms due to diffusion effect, applied voltage, and from the reaction between electrons and ions in the electrode and electrolyte respectively. The double layer capacitance is directly proportional to the contact surface area between the electrode (carbon, platinum) and the electrolyte [40]. Hence measuring double layer capacitance values before and after degradation can help identify possible ECSA loss and carbon oxidation.

## **1.7. Catalyst layer failure analysis techniques and challenges**

The structural characterization of the catalyst layers in the MEA is very important in order to understand failure modes and degradation mechanisms in fuel cells. Scanning electron microscopy (SEM) is a widely used technique to characterize catalyst layer structure and thickness [32] [41] [42] at the micro scale. The resolution of SEM varies anywhere between 1 nm and 100 nm depending on the instrument. SEM requires the user to physically cut and embed the sample into epoxy and polish the surface, yielding a 2D cross section image of the MEA. Sample preparation is more challenging as the MEA degrades and the catalyst layers intermingle with other layers in the MEA and become difficult to separate. Even if the layers were to separate, the samples might be altered chemically and structurally. SEM has been used to show cracks in the catalyst layer which are caused by the MEA manufacturing processes (solvent evaporation, poor membrane handling, bending or stretching of the MEA) or electrolyte swelling during hydrated fuel cell operation [32]. A typical catalyst layer crack size of  $\sim 2 \mu\text{m}$  for a BOT MEA was measured with a field of view of  $68 \mu\text{m}$  whereas catalyst and ionomer clusters

of  $\sim 200$  nm with a field of view of  $\sim 4$   $\mu\text{m}$  was also measured [32]. However, the SEM operates in vacuum, which will cause dehydration of the ionomer in the catalyst layer, resulting in morphological artifacts [43].

A study using IL (Identical location)-SEM revealed a significant increase in Pt particle size from 10 nm to 200 nm after an MEA was subjected to start-stop conditions (50,000 cycles from 0.2 V to 1.4 V) [44]. However, at such high upper potential where carbon oxidation is dominant [45], no significant carbon corrosion was observed using IL-SEM, indicating the limitation of a 2D characterization technique. In addition, temporary or permanent damage in the surface structure of a sample can occur from the charged particles used in electron imaging techniques such as SEM and transmission electron microscopy (TEM) [46]. TEM is a widely used technique to characterize catalyst layer nano structure and measure particle size distribution [23] [47] with a typical resolution of 0.2 nm. TEM works by illuminating the sample being imaged with an electron beam inside a high vacuum chamber, and then detects the electrons transmitted through the sample, resulting in a 2D image. It is capable of detecting detailed micro structure by means of high resolution and high magnification imaging. A TEM with a spatial resolution of 0.2 nm was used to investigate catalyst particle distribution on a carbon black support, measuring catalyst particles ranging from 1.5 nm to 5 nm [48]. However, conventional TEM has a limited depth-resolution, since the electron scattering originates from a three-dimensional object but the structural information along the beam is superimposed into a two-dimensional plane.

## **1.8. A technique to overcome challenges**

A technique which helps overcome these challenges and allows one to study the catalyst layer structure and properties non-invasively is X-ray computed tomography (XCT). XCT enables reconstruction of three-dimensional images for more comprehensive analysis than

what is possible from two-dimensional views. In addition, sample preparation is minimal in general using XCT [49], yielding an entire reconstructed MEA for 3D measurement and analysis [50]. XCT is developed using laboratory X-ray sources with photon flux of  $10^9$ – $10^{10}$  photons  $s^{-1}$   $cm^{-2}$  [51] in contrast to synchrotron, which uses photon flux of several orders in magnitude higher compared to XCT. For example, a decrease in fuel cell performance and loss in mechanical strength of ionomer in the catalyst layer was observed after synchrotron radiation [52]. In another study using synchrotron computed tomography, beam induced degradation of fuel cell materials was observed which can lead to artifacts in the final 3D reconstruction [53]. However, using XCT no measurable change in fuel cell performance was seen after 20 hours of exposure; which was attributed to lower photon flux from XCT compared to synchrotron [51]. In addition, availability of synchrotron facility is limited and its regular access is constrained by increasing demands and high cost. At the micro length scale, XCT has been used to visualize the morphology and uniformity of fuel cell electrodes prepared by different fabrication methods [50], while at the nano length scale, XCT has been used to extract the volumetric distribution of the effective secondary pores, carbon support agglomerate diameters, and pore size distribution in the catalyst layer [10]. In order to attain a comprehensive understanding of catalyst layer failure modes, an investigation at both of these length scales is desirable.

## 1.9. Objective

The objective of the present work is to qualify the multi-length scale approach enabled by the XCT technique for 3D failure analysis of *in situ* degraded fuel cell electrodes. Analysis and comparison of beginning of test (BOT) and end of test (EOT) MEA images of various degraded electrodes at the micro and nano scales is expected to provide an extensive understanding of catalyst layer degradation in fuel cells which complements *in situ* diagnostics such as fuel cell performance, ECSA, and impedance measurements. Catalyst layer cracks and

thickness are analyzed at the micro scale, whereas the detailed catalyst layer structure is analyzed at the nano scale. In addition, an image processing based technique for phase segregation is developed, which allows for investigation of the pore, ionomer, and Pt/C dominated phase distributions and their respective roles in the catalyst layer failure mode.

## Chapter 2.     **EXPERIMENTAL PROCEDURE**

### **2.1. Scope of analysis**

At first, a baseline study on a conditioned BOT and a high potential degraded EOT MEA is performed to qualify the multi-length scale approach XCT technique for 3D failure analysis of *in situ* degraded fuel cell electrodes. The nano-XCT results are compared with MIP, SEM and TEM results for support and validation. Additionally, a parametric study using the same approach is performed to investigate the effect of changes in stressors, composition, and morphology of the catalyst layer on the degradation process and failure modes.

In general, the MEAs used in this work were made with a Nafion<sup>®</sup> NR211 catalyst coated membrane (CCM) with 45 cm<sup>2</sup> active area at a Pt-loading of 0.4 and 0.1 mg cm<sup>-2</sup> on the cathode and anode respectively. The gas diffusion layers (GDL) were made by a company named Avcarb. MEAs were prepared by bonding cathode and anode GDLs to the CCM in a compaction press. The assembled fuel cell was first conditioned using hydrogen on anode and air on cathode to steady state at 75°C, 100% relative humidity (RH), and at 1.3 A cm<sup>-2</sup> current density overnight to activate the fuel cell for better performance [54], and will be referred as BOT MEA. The BOT MEA was subjected to an upper and lower potential square wave cycling cathode degradation accelerated stress test (AST) in hydrogen/air at 80°C and 100% RH. The specifics of each MEA's composition and AST protocol used for this study are presented in Table 1 and discussed below:

S.No	Scope	MEA	Cathode AST
1(a)	Baseline	BOT high crack	
1(b)	Baseline	EOT high crack at center of island	1.3 V upper potential limit (UPL) w 4700 cycles
1(c)	Baseline	EOT high crack at edge of island	1.3 V UPL w 4700 cycles
1(d)	Effect of upper potential limit	EOT high crack	1.2 V UPL w 4700 cycles
2(a)	Effect of pre-existing crack	BOT low crack	
2(b)	Effect of pre-existing crack	EOT low crack	1.3 V UPL w 4700 cycles
3(a)	Effect of ionomer loading amount	BOT high ionomer loading	
3(b)	Effect of ionomer loading amount	EOT high ionomer loading	1.2 V UPL w 4700 cycles
4(a)	Effect of catalyst support type	BOT HSAC support	
4(b)	Effect of catalyst support type	EOT HSAC support	1.2 V UPL w 4700 cycles

**Table 1: The scope of analysis and applied cathode AST for MEA's used in the presented work.**

### 2.1.1. Baseline

A BOT MEA with a graphitic lower surface area carbon (LSAC) support, a 50/50 wt% Pt/C catalyst, and 23 wt% Nafion<sup>®</sup> ionomer was used, yielding a high crack catalyst layer surface. The BOT conditioned MEA was subjected to cathode degradation through 4,700

voltage cycles with a 1.3 V upper potential limit for 60 sec and a 0.6 V lower potential limit for 30 sec [14].

### **2.1.2. Effect of upper potential limit**

An identical BOT MEA as described in Section 2.1.1 was subjected to similar cathode degradation AST as detailed in Section 2.1.1 except with a 1.2 V upper potential limit.

### **2.1.3. Effect of pre-existing cracks**

An otherwise identical BOT MEA as described in Section 2.1.1 but with a cathode catalyst layer with a relatively lower frequency of cracks. The BOT MEA was subjected to identical cathode degradation AST as detailed in Section 2.1.1.

### **2.1.4. Effect of catalyst support type**

An otherwise identical BOT MEA as described in Section 2.1.1 with a high surface area carbon (HSAC) support was subjected to identical cathode degradation AST as discussed in Section 2.1.2.

### **2.1.5. Effect of ionomer loading amount**

An otherwise identical BOT MEA as described in Section 2.1.1 with 50 wt% Nafion<sup>®</sup> ionomer loading was subjected to identical cathode degradation AST as discussed in Section 2.1.2.

## 2.2. Sample preparation

The BOT and EOT MEA samples prepared for micro scale analysis were cut with a scalpel and measured 1 cm x 1 cm. The sample size was determined by a trade-off between achieving high X-ray signal to noise ratio with a smaller sample while maintaining a statistically significant size for experimentation. The cathode catalyst layer samples for nano scale analysis were prepared by first separating the CCM from the MEA by hand and subsequently using an FEI Helios Nano Lab 650 Focused Ion Beam (FIB) system to perform lift-out. The FIB technique uses a finely focused ion beam to cut a specimen cross section at the desired location. The BOT and EOT catalyst layer samples were cut using a focused Ga<sup>+</sup> beam at an acceleration voltage of 30 kV and 2.5 nA current. The samples were then lifted out from a crack free location and were 10 μm x 10 μm x full thickness in size. It was determined that the catalyst layer samples needed to be smaller than the field of view (FoV) of nano XCT in order to achieve higher signal to noise ratio and eliminate artifacts from the reconstruction. For example, a streaking and shading artifact has been observed in CT scan for samples bigger than the FoV, since part of the sample outside the Fov is projected onto the sample inside the FoV [55]. On the other hand, no artifacts were reported for the sample with size smaller than the FoV of XCT [56]. The lift out sample was then placed on the tip of a 0.2 mm pin as shown in Figure 5. The samples for a complementary supporting analysis using TEM was obtained by embedding the CCM in an epoxy resin and slicing it to thin films (~70-90 nm) using a Leica EM UC6 ultra microtome to reveal the cross-section and were collected on copper grids for imaging.

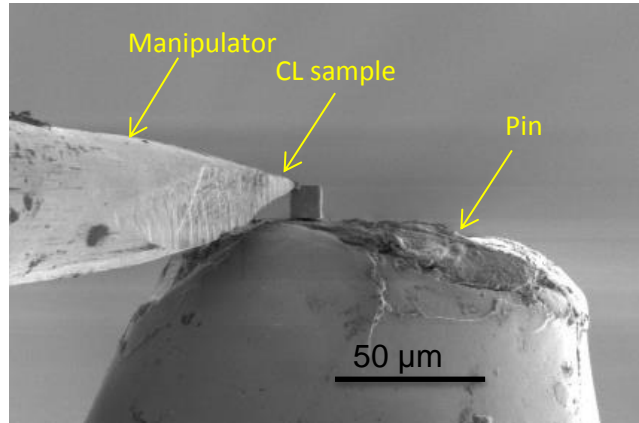


**Figure 5: A 10  $\mu\text{m}$  cube focused ion beam (FIB) lift out catalyst layer sample placed on the tip of a 0.2 mm wide pin with the help of a manipulator.**

### **2.3. Morphological characterization techniques**

The proposed three-dimensional, non-destructive multi-length scale visualization approach utilized a ZEISS Xradia 520 Versa XCT system (Versa) at the micro length scale and a ZEISS Xradia 810 Ultra XCT system (Ultra) at the nano length scale. In a XCT system, the intensity of X-ray photons detected by the detector at each pixel within the FoV is assigned a grey level value, and a 2D radiograph is created. The assigned grey level value corresponds to X-ray attenuation which is proportional to the amount of x-rays absorbed and scattered by each pixel. X-ray attenuation is material specific and is a function of density and the effective atomic number. Subsequently, the 2D radiograph is collected at regularly spaced angles about a specified rotational axis to yield a tomography set which when processed yields a complete 3D rendering of the sample under study. The 3D reconstruction for all tomography data sets used the ZEISS XMReconstructor software followed by viewing on the TXM 3Dviewer software also supplied by ZEISS. The spatial resolution at the micro scale of the Versa is 700 nm with a variable FoV while that for the Ultra at the nano scale is 50 nm in a FoV of 16  $\mu\text{m}$ .

The full BOT and EOT MEAs were first visualized with micro scale resolution on the Versa XCT system as shown in Figure 6 in order to analyze the overall structural impact of

cathode degradation. The mounted sample for the Versa was clamped in a clip type holder and, after initializing the X-ray source at 80 kV and 7 W using a tungsten target, a region of interest (ROI) was chosen to establish an axis of rotation. This was accomplished by imaging the sample at  $0^\circ$  and at  $-90^\circ$ ; then, the system was allowed to stabilize for about 1 hour prior to data acquisition

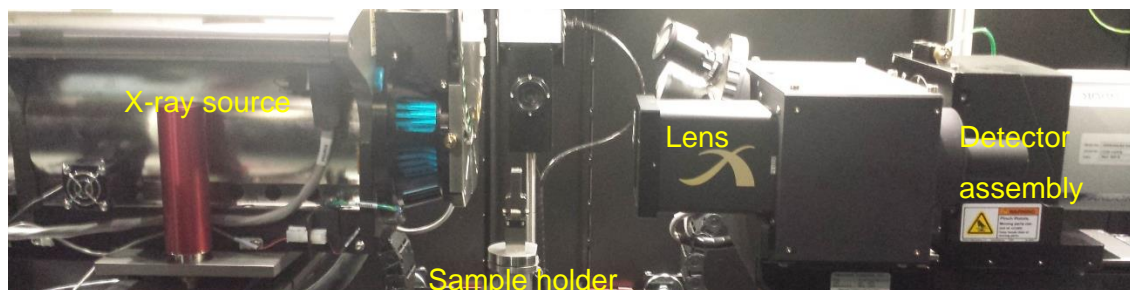


**Figure 6: Internal components of ZEISS Xradia 520 Versa XCT system.**

Each tomography data set was acquired at 20 seconds exposure per projection with 1,601 projections for an experimental time of about 9 hours per sample. Although the FoV used for these tomography data sets was limited in size, the selected region was observed to be representative of the overall structure of the catalyst layer after carefully examining the entire MEA. A 2D map of the cracks was created by flattening the 3D reconstructed structure of the undulated catalyst layer along its thickness in MATLAB and used to evaluate the total projected surface area occupied by the cracks. The projected surface area fraction occupied by a crack with a specific width was calculated and incrementally added by filling the crack space with disks of increasing diameter. The crack surface areas were normalized to the crack surface area of the largest crack and a crack width versus cumulative crack surface area graph was generated using Microsoft Excel. The catalyst layer thickness was measured using Image Pro [20].

The small catalyst layer samples prepared by FIB lift-out and placed on a pin were mounted on the rotating stage of the Ultra XCT system for nano length scale analysis as shown in Figure 7. The Ultra XCT system generates a monochromatic X-ray beam of 5.4 keV using a chromium target, which is the lowest X-ray beam energy and highest resolution currently available with commercial systems. The Ultra XCT has an anode water cooling loop to allow for proper cooling.

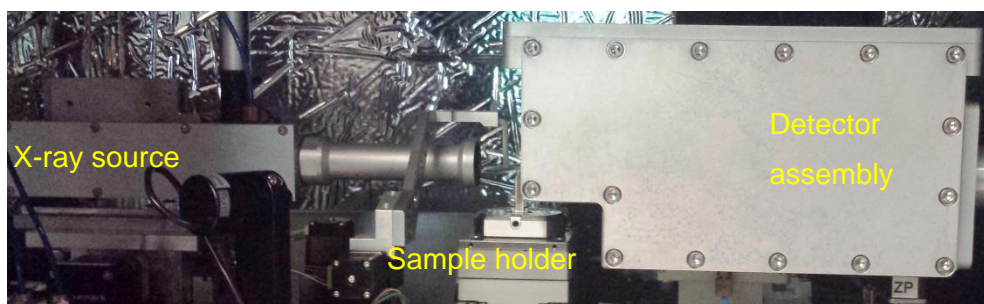


**Figure 7 : Internal components of ZEISS Xradia 810 Ultra XCT system.**

The preferred mode of operation was the high resolution (HRES) absorption contrast mode with a field of view of 16  $\mu\text{m}$ . A mosaic technique was used to locate the ROI by acquiring a matrix of images with field of views stitched around the center; thus, providing an overview of the sample and its surroundings. Then, an ROI was chosen and the axis of rotation was fixed by imaging a sample detail at 0° and at -90°. The next step required the acquisition of 40 2D reference radiographs to correct for background in the final 3D reconstruction. Finally, each tomography data set was acquired at 200 seconds exposure per projection with 901 projections for an experimental time of about 52 hours per sample.

The reconstructed 3D data sets were exported to Avizo<sup>®</sup>, which is a software application that enables interactive visualization and computation on 3D data sets. Avizo<sup>®</sup>'s "resample transformed image" function was used to align the 3D data set with Avizo<sup>®</sup>'s localized axes followed by post-acquisition 3D image analysis using an interactive thresholding technique to segregate air from the solid phase. Figure 8 shows 2D raw grey scale images for a baseline

BOT CCL data set, discussed in Section 2.1.1 above, where a comparison before and after thresholding shows the effect of the air segmentation on the resulting catalyst layer structure. As expected, after thresholding, the overall structure of the material was retained, while voxels that contain a mix of pore and solid phase (with features smaller than the instrument resolution) were converted into either pore or solid, depending on the local grey scale value.

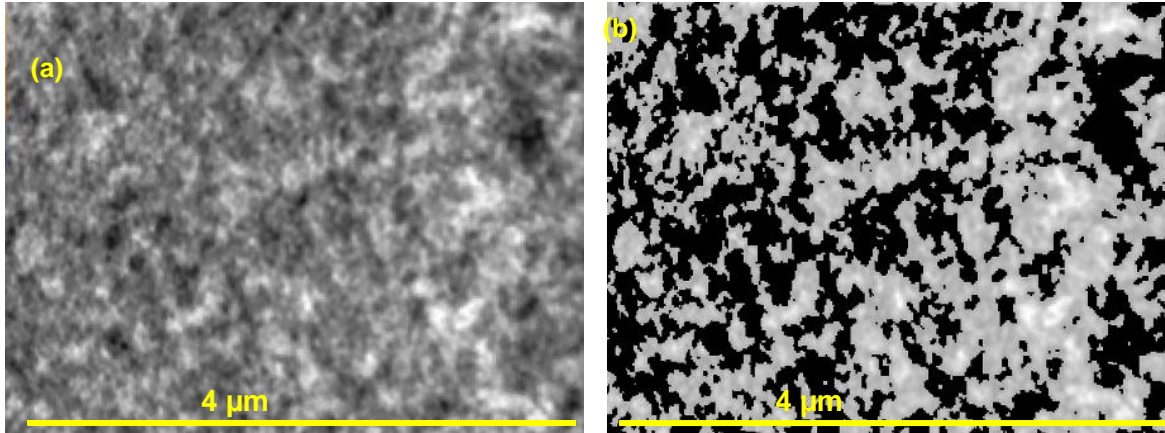


**Figure 8 : Grey scale 2D images of baseline BOT CCL structure (a) before thresholding (b) after thresholding at nano scale, where whites are solids and blacks are pores.**

The volume fraction function in Avizo<sup>®</sup> was used to calculate the solid volume fraction and porosity of the entire FIB lift out sample and a representative 3D sub-domain was chosen for further analysis. Once the solid and pore phases were identified, the data sets were exported to a binary grid of pore and solid cells and used for further analysis with numerical algorithms previously developed by our group [57][58] and a modified version of the pore scale model originally developed at the University of Victoria [57][58][59][60]. The pore size distribution was obtained by calculating the total volume of the void contained inside spheres with different specific diameters inserted into the pore space.

Numerical simulations were conducted to calculate the effective diffusivity of oxygen and water vapor in the three principal through-plane and in-plane directions of the catalyst layer. The structural matrix obtained from the nano scale XCT data was used as the computational

domain. The numerical model [58] applies a gradient of working gas concentration in each direction at a time, and solves Fick's second law of diffusion at steady state as shown in equation 4, for example for calculating the effective diffusivity of O<sub>2</sub>:

$$\nabla \cdot (-D_{O_2} \nabla c_{O_2}) = 0 \quad (4)$$

Local diffusion coefficient ( $D_{O_2}$ ) is calculated using Bosanquet equation to account for both molecular diffusion ( $D_F$ ) and Knudsen diffusion ( $D_K$ ) as seen in equation 5. The Knudsen diffusion was calculated using equation 6:

$$D_{O_2} = (D_F^{-1} + D_K^{-1})^{-1} \quad (5)$$

$$D_K = \frac{d_{pore}}{3} \sqrt{\frac{8R_g T}{\pi M}} \quad (6)$$

, where  $d_{pore}$  is the pore diameter,  $M$  is the molecular weight of the gas species,  $R_g$  is the gas constant, and  $T$  is the temperature in Kelvin. The Knudsen effect was included to account for the collisions between gas molecules and pore walls which occur in nanoporous materials such as the present catalyst layer structures. Once equation 4 is solved the effective diffusion coefficient is calculated using the following formula:

$$D_{eff} = \frac{|J_{O_2, i}| l_i}{\Delta C_{O_2}} \quad (7)$$

, where  $J_{O_2}$  is the oxygen flux,  $i$  is the direction of simulation,  $l$  is the distance through which the gradient was applied, and  $\Delta C_{O_2}$  is the oxygen concentration drop across the 3D domain. A similar process is repeated for the calculation of effective diffusivity for water vapor. The relative gas diffusivities (relative to bulk diffusion) were also calculated and found to have a unique value for each gas due to the significance of Knudsen diffusion. Finally, the solid phase was further segregated into pore, ionomer, and Pt/C dominated phase using Avizo<sup>®</sup>'s multi thresholding function and will be discussed in detail in Section 3.1.2.1.1.

A supporting TEM analysis to compliment XCT findings was done by recording the cathode catalyst layers at high resolution using a Tecnai Osiris TEM instrument from FEI, equipped with a Gatan Ultrascan 1000XP-P 2k x 2k pixel charge-coupled device camera at 200 KeV. The dark field images are achieved by first tilting the electron beam off axis and subsequently using the objective aperture to select diffracted electron beams. This will allow only the diffracted electron beams to reach the image plane. Since the diffracted beams have strongly interacted with the sample, very useful information can be extracted using dark field images. The images were analyzed using Digital Micrograph software from Gatan Microscopy Suite. Elemental maps were recorded using a Gatan Ultrascan CCD camera equipped with analytical TWIN objective lens integrated with Super-X energy dispersive X-ray (EDX) detection system based on silicon drift detector technology. The micro analysis of the acquired EDX spectra was carried out using Quantax Esprit 1.9 software from Bruker.

The size of platinum particles in the catalyst layer was measured using X-ray diffraction (XRD) technique. Powder samples of the cathode catalyst layer were scraped from the catalyst coated membrane (CCM) and submitted to an external lab for XRD analysis, where the samples were then gently stirred in an alumina mortar and smeared on a zero-background quartz plate with ethanol. Step-scan X-ray powder-diffraction data were collected over the range 6-103°2θ (0.04°2θ step, 1.5 sec/step) with CoK $\alpha$  radiation (1.7902 Å) on a Siemens (now Bruker AXS) D5000 Bragg-Brentano diffractometer equipped with an Fe monochromator foil, 0.6 mm (0.3°) divergence slit, incident and diffracted-beam Soller slits and a VANTEC-1 strip detector. The long fine-focus Co X-ray tube was operated at 35 kV and 40 mA, using a take-off angle of 6 degrees. The average platinum crystallite size was determined using the Scherrer Equation,

$$D = \frac{K\lambda}{\beta \cos\theta} \quad (8)$$

,where  $D$  is the diameter of the crystallite,  $\beta$  is the width of the peak at half maximum intensity of a specific phase (hkl) in radians,  $K$  is the Scherrer constant equal to 0.9,  $\lambda$  is the wavelength of incident x-rays and  $\theta$  is the center angle of the peak.

## 2.4. Electrochemical diagnostics techniques

The *in situ* diagnostics such as fuel cell performance curve, ECSA, and impedance were measured before and after accelerated stress testing. Polarization curve for fuel cell performance analysis were acquired at 75°C and 100% relative humidity with pure oxygen and air. The cell polarization was carried out at constant gas flow rates and was taken from high to low current density. Points are held for a few minutes to allow for the voltage to stabilize. The polarization curve is obtained by plotting the steady voltage response to the operational current.

CV scans were acquired using a Solatron SI1287 potentiostat, and then the scans were used to calculate the ECSA. Hydrogen present at the anode acted as the reference electrode as the cathode potential was cycled between 0.1–1.2 V RHE at 20 mV/s. The ECSA was determined by CO stripping, assuming a charge density of 420  $\mu\text{C}/\text{cm}^2$  to break the linear Pt-CO bond.

EIS measurements were acquired by applying a 10 mV AC perturbation signal on a 0.45 V RHE DC bias potential [61]. A SI1287 Solatron potentiostat and a 1250 Solatron Hi Frequency Response analyzer were used in a 4-electrode configuration with a frequency sweep between 50 kHz to 0.05 Hz. In order to eliminate any pseudo-capacitive effects that result from hydrogen and oxygen adsorption-desorption, a bias potential was applied. In order to calculate the impedance and capacitance, Z-plot and Z-view software were used to conduct and analyze the EIS spectra. Measurements were taken in a nitrogen and hydrogen atmosphere on the

cathode and anode, respectively. Finally, the EIS spectra were fit to an equivalent circuit representing a transmission line network of the catalyst layer.

## Chapter 3.     **RESULTS AND DISCUSSION**

The proposed 3D, multi-length scale failure analysis approach for fuel cell electrodes follows a sequential two step analysis where the catalyst layer thickness and crack distribution were investigated at the micro scale, while the detailed catalyst layer structure was investigated at the nano scale. The catalyst layer structure at the nano scale for the baseline samples was further analyzed via phase segmentation to identify component phase distributions and fractional differences induced by catalyst layer degradation. Additionally, a parametric study using a similar approach was performed to investigate the effect of stressors, composition, and morphology of the catalyst layer on the degradation process and failure modes.

### **3.1. Baseline**

A high catalyst layer crack BOT MEA subjected to a high potential AST is studied and compared and will be used as a baseline to compare and study other AST degraded MEAs. The catalyst layer structure at nano scale is verified against TEM results from identical samples obtained by Senthil Velan Venkatesan at Simon Fraser University.

#### **3.1.1. Micro length scale analysis**

The full BOT and EOT MEAs were first visualized with micro scale resolution in order to analyze the overall structural impact of cathode degradation. A comparison of the virtually extracted 3D views of the BOT and EOT cathode catalyst layers (CCLs) is provided in **Error! Reference source not found.** (a) and (b), respectively. The initial mud cracks [31] are

observed in the BOT image which may be due to stress and strain during the manufacturing process attributable to solvent evaporation [62]. However, in the EOT image, mud cracks appear to be more prevalent, and the remaining catalyst layer material can be observed to form island structures. An island structure can be defined as an isolated catalyst layer structure, surrounded by cracks. When comparing to the BOT image, it is evident that the edges of the island structures in the EOT catalyst layer are slightly protruding with respect to a more recessed center.

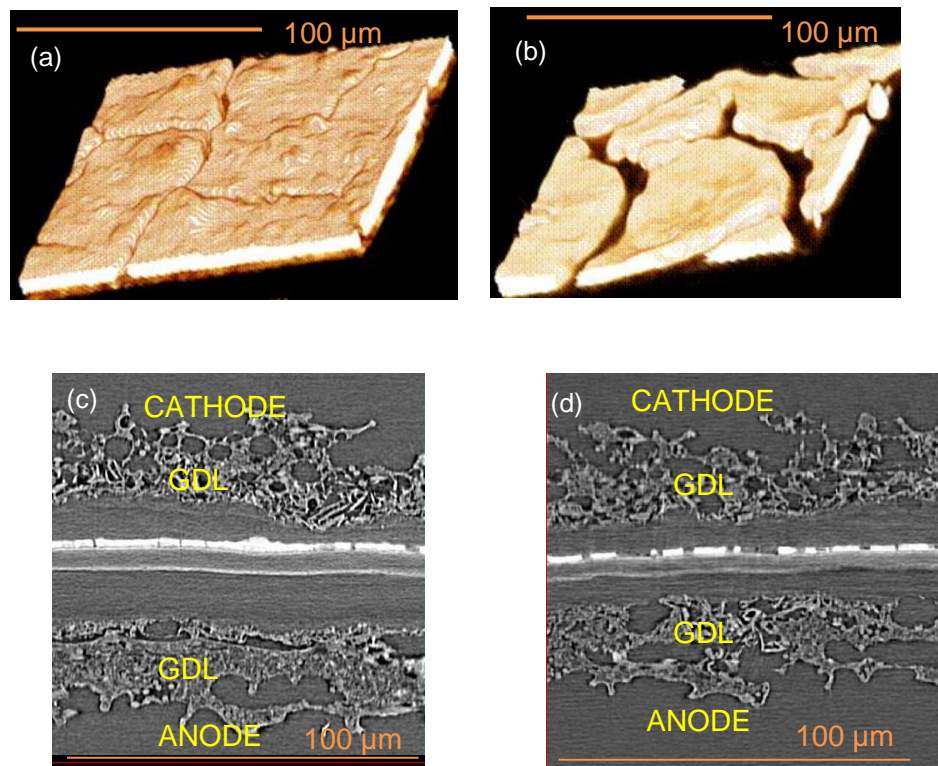


**Figure 9: 3D rendering of cathode catalyst layers at a) BOT and b) EOT and 2D virtual cross-sections of (c) BOT MEA and (d) EOT MEA showing the effects of cathode degradation.**

The total crack surface area fraction was measured to be 6% and 30% for the BOT and EOT CCLs, respectively; a 5x increase in crack area for the EOT sample. The distribution of the crack widths presented in Figure 10 shows a considerable increase in the crack width from BOT to EOT, with typical widths of ~5 and ~11 μm, respectively.

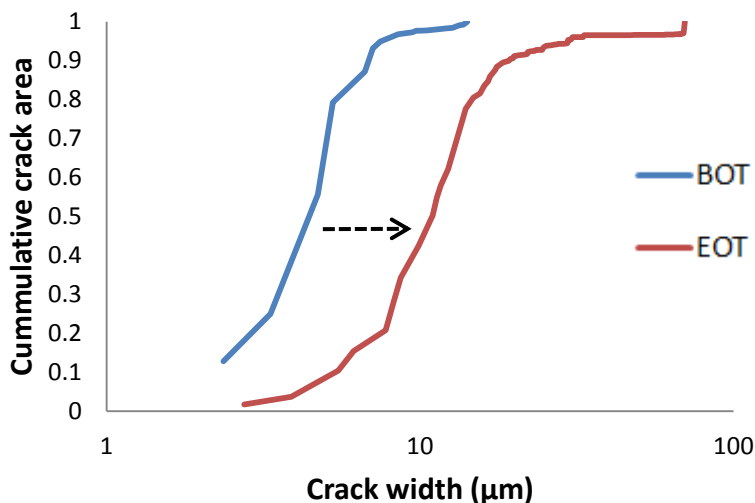


**Figure 10: Normalized cumulative crack area of the cathode catalyst layer crack width in the baseline BOT and EOT MEAs.**

It is thus determined that both the width and length of pre-existing mud cracks increase substantially during cathode degradation. **Error! Reference source not found.** (c) and (d) shows a cross-sectional view of the reconstructed images of the full BOT and EOT MEAs, where the thin, bright anode and cathode catalyst layers can be seen at the center, flanked by the thicker GDLs, and separated by the membrane. The gaps seen between the GDLs and the CCM indicate that the GDLs were partially detached from the catalyst layers possibly due to membrane contraction during drying. The cathode catalyst layer in the EOT MEA shows an uneven layer with large voids throughout its thickness, which are indicative of cracks, as previously observed. The BOT and EOT CCL measured thicknesses were  $14 \pm 2 \mu\text{m}$  and  $6 \pm 2 \mu\text{m}$ , respectively; resulting in 57% thinning. The catalyst layer thinning implies that the carbon support has been corroded and the platinum has been concentrated or detached and no longer has a support. In addition, the brighter surface areas seen in the EOT sample as shown in **Error! Reference source not found.** (b) may be an indication of increased volumetric platinum concentration after carbon corrosion and thinning [63]. The present results reliably demonstrate that catalyst layer crack growth and thinning can occur in parallel with comparable rates during

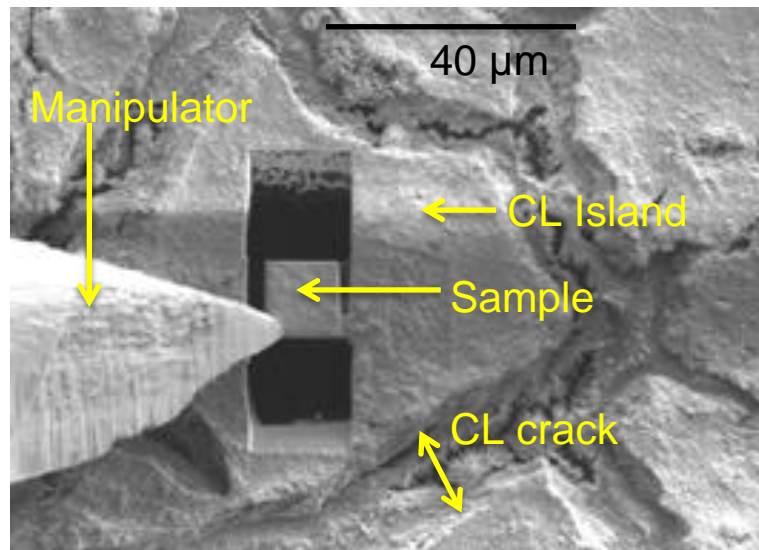
cathode degradation. This can be attributed to a joint catalyst layer failure mode in the form of bulk carbon corrosion and local erosion [32] from water flooding in the catalyst layer cracks.

### 3.1.2. Nano length scale analysis

The second step of the proposed multi-length scale failure analysis approach complements the micro-scale analysis by studying a FIB lift out of the CCL island using nano-scale resolution in order to analyze the structural changes due to cathode degradation.

#### 3.1.2.1. Center of CCL Island

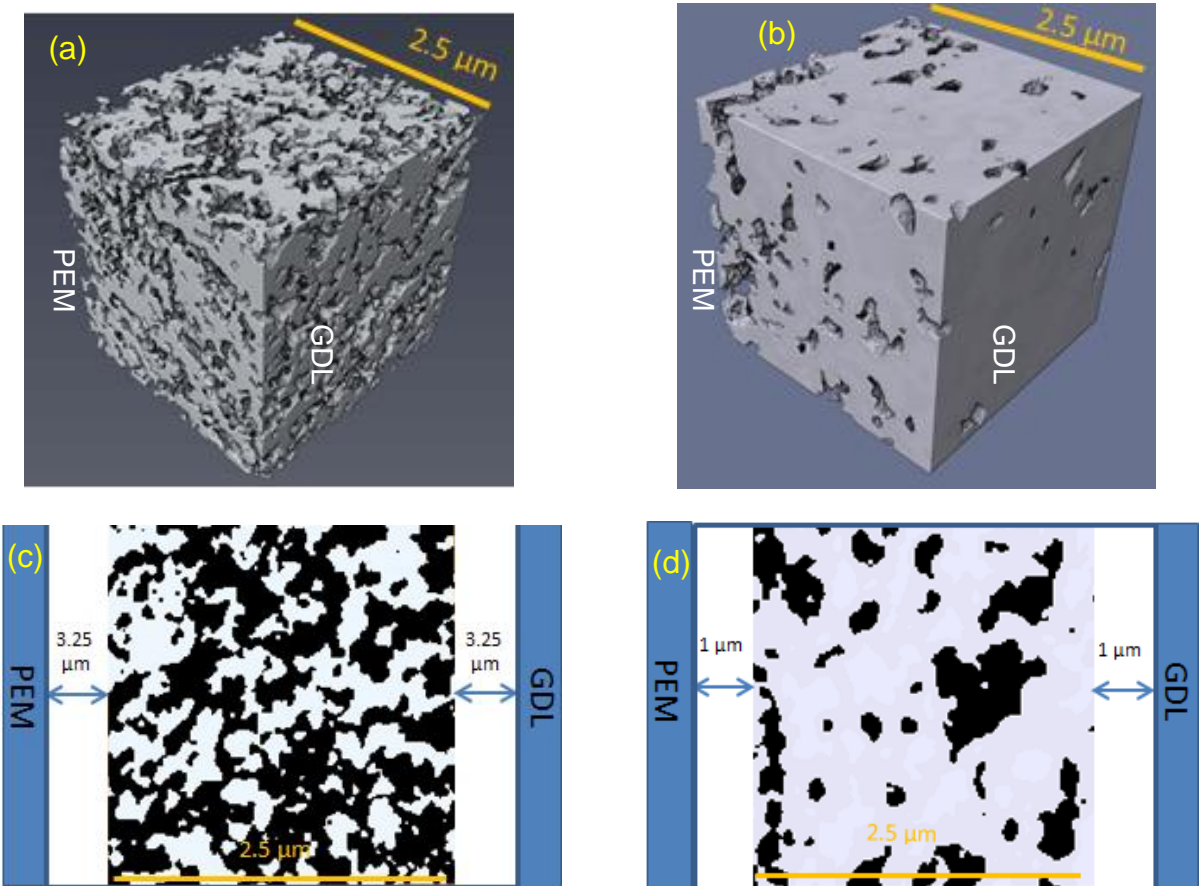
The HRES absorption contrast mode was used to acquire tomography data sets of the FIB lift out sample from the center of catalyst layer island as shown in Figure 11.



**Figure 11 : FIB lift out of an EOT CCL sample using a manipulator from the center of the island, also indicating CCL crack.**

Thus, a 3D sub-domain of the BOT CCL structure was obtained, revealing a homogenous network of pores and solids as seen in Figure 12 (a). A 2D cross-sectional view of the thresholded, reconstructed sub-domain is shown in Figure 12 (c), which also indicates the

location of the sub-domain inside the CCL with respect to the locations of the adjacent PEM and GDL interfaces. A uniform distribution of pores and solids is observed across the CCL sub-domain. A similar procedure yielded a thresholded (solid, pore) 3D sub-domain of the EOT CCL structure, which features a more compact structure compared to the BOT CCL, as shown in Figure 12 (b). Additionally, the EOT CCL structure contains a network of pores and solids which is relatively inhomogeneous.



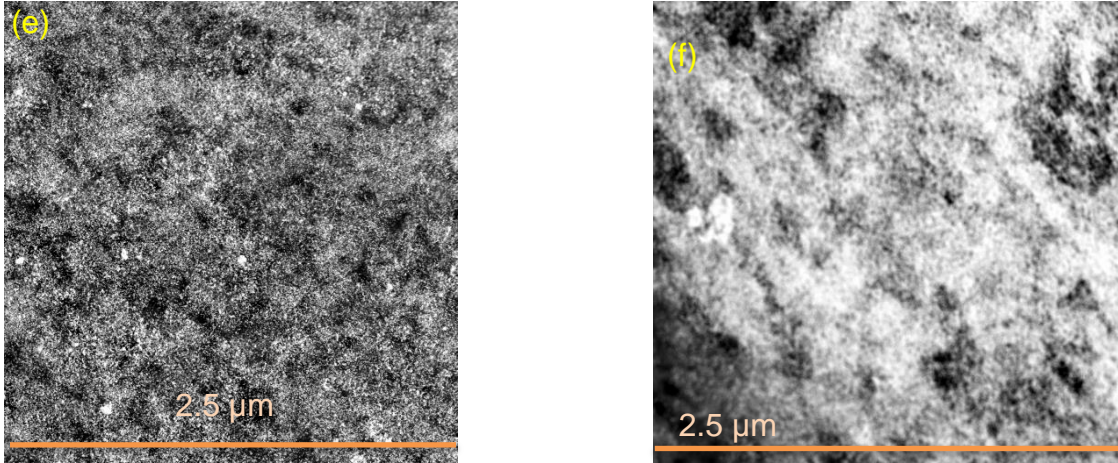


**Figure 12: 3D and 2D cross sectional representation of the CCL structure indicating the imaging location from the PEM and GDL interfaces at BOT (a) & (c) and at EOT (b) & (d). 2D TEM images of the cathode catalyst layer at (e) BOT and (f) EOT, where black is pore and white is solid.**

The 2D cross-sectional view provided in Figure 12 (d) further reveals more isolated and larger pores as well as a denser solid phase network in the EOT structure compared to the BOT structure. The 2D views of the cathode catalyst layer at BOT and EOT are in good visual agreement with TEM dark field images in Figure 12 (e) and (f). A homogeneous distribution of pore (black) and solid (white) phases can be observed at the BOT TEM image, whereas bigger pores and comparatively concentrated solid phases are observed in the EOT TEM image, which supports nano-XCT findings.

The solid volume fraction of the 3D sub-domain for the BOT CCL was found to be 46% with a corresponding pore volume fraction or porosity of 54%. Using the same method, the EOT CCL was found to have 77% solid volume fraction and 23% porosity. The BOT CCL porosity is in good agreement with a supporting measurement by MIP, resulting in 53% porosity. It is thus evident that substantial pore space was lost during the cathode degradation process, indicating that the CCL structure has collapsed due to loss of solid phase integrity from carbon corrosion. The substantial CCL thinning measured from the micro scale analysis also supports this finding. The comparison of the pore size distributions of the BOT and EOT CCLs indicates that the EOT

material contains larger pore sizes, as shown in Figure 13. Larger pores were not expected since the catalyst layer had collapsed; however, larger pores may have formed prior to and after collapsing from carbon corrosion and Pt dissolution, i.e., loss of solid phase material.

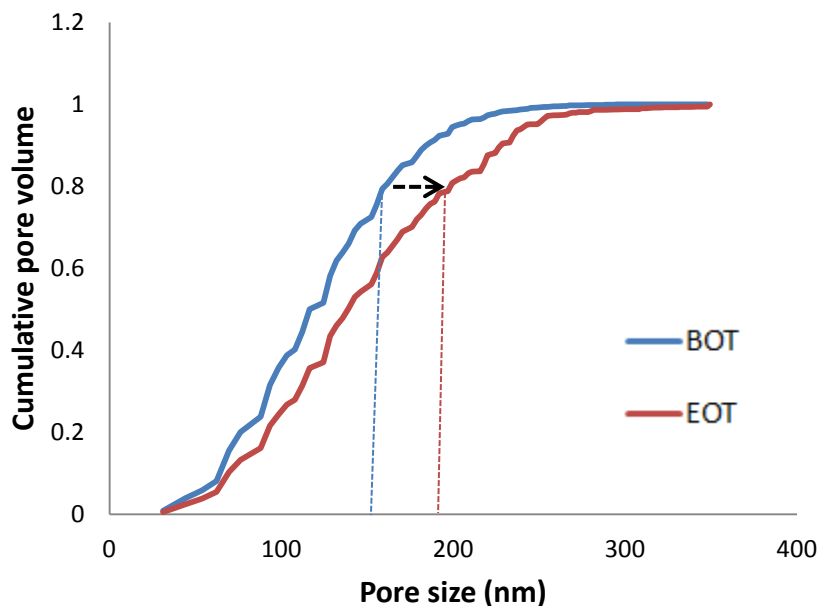


**Figure 13: Cathode catalyst layer pore size distribution at BOT and EOT, indicating larger pores at EOT.**

The numerical simulations as discussed in Section 2.3 were used to calculate the effective diffusivity of oxygen and water vapor in the three principal through-plane and in-plane directions of the catalyst layer sub domain. In the BOT CCL, the effective diffusivity of oxygen and water vapor was found to be isotropic whereas in the EOT CCL it was found to be anisotropic with respect to the through-plane and in-plane directions, as shown by the results reported in Table 2. It can be observed that all EOT diffusivity values are lower than for BOT due to the lower porosity and more isolated pores: overall, the EOT in-plane diffusivities are an order of magnitude lower than at BOT, while the through-plane diffusivities at EOT are two orders of magnitude lower than at BOT.

	$D_{eff}$ (Effective diffusivity) $10^{-7} \text{ (m}^2 \text{ s}^{-1}\text{)}$		$D_{eff,O_2}/D_{O_2,air}$ (Relative diffusivity)	
	BOT	EOT	BOT	EOT
Oxygen	20	2.6 (In-plane) 4.6 (In-plane) 0.5 (Through-plane)	0.09	0.01 0.02 0.002
Water vapor	23	2.9 (In-plane) 5.2 (In-plane) 0.6 (Through-plane)	0.09	0.01 0.02 0.002

**Table 2: Diffusivity of oxygen and water vapor of a high crack CCL at BOT and a high potential degraded EOT.**

The more severe reduction in the through-plane direction is most likely due to the collapsing of the cathode catalyst layer structure from carbon corrosion. Hence, the diffusion transport phenomenon is affected the most in the through-plane direction, which is generally the most important principal direction of reactant and product transport during fuel cell operation. The reduction in diffusivity of the gases will result in fuel cell performance losses at EOT, noticeably at higher current densities as seen in Figure 14, where the voltage drop in the degraded EOT MEA is significantly higher than the pristine BOT MEA.

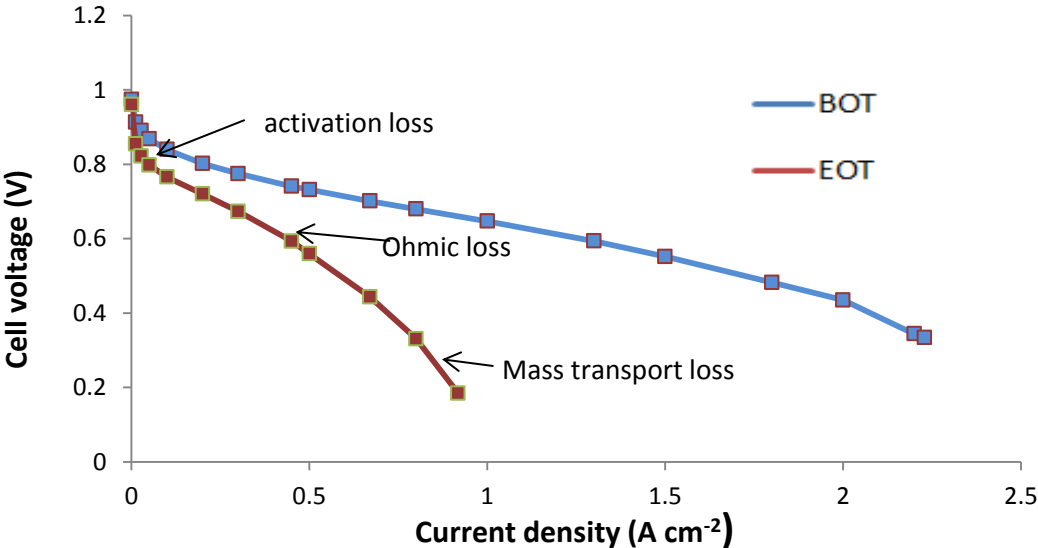


**Figure 14: Fuel cell polarization curves measured in situ at the BOT and EOT states indicating activation, ohmic and mass transport loss regions at EOT.**

### **3.1.2.1.1. Cathode catalyst layer segmentation**

In the context of fuel cell electrode degradation and failure analysis, each individual material in the catalyst layer (carbon, Pt, and ionomer) is susceptible to decay; hence, it is important to identify and quantify these materials independently of one another. An XCT based approach for nano scale phase segregation of carbon and PTFE in the micro porous layer (MPL) was recently reported by our group [56], and in the present work, a similar methodology was followed to perform a 3D phase segmentation of the catalyst layer. The phase segmentation of the 3D catalyst layer structure, which to the authors' knowledge has not been previously reported, was performed for the BOT and EOT CCLs using Avizo<sup>®</sup> and three different phases were identified as pore, Pt/C, and ionomer dominated phases. The carbon support and catalyst particles were combined as a single Pt/C phase because single platinum particles, *circa* 5 nm in size, are not resolved at a system resolution of 50 nm. The known composition of the BOT CCL was 38.5 wt% platinum, 38.5 wt% carbon, and 23 wt% ionomer, which was converted to volume fractions by dividing by the respective material density. The calculated volume fraction was normalized to the 3D sub-domain obtained in Section 3.2 by first adding the calculated volume fractions, then dividing the total volume fractions by 46% to get the total volume of the 3D sub-domain, and lastly dividing the calculated volume fractions by the total volume of the 3D sub-domain. This resulted in 26% Pt/C dominated and 21% ionomer dominated volumes with a ratio of 1.23:1, respectively. The grey scale histogram of the reconstructed 3D sub-domain was segmented using Avizo<sup>®</sup>'s multi-thresholding function as shown in Figure 15, based on the calculated volume fractions and the X-ray linear attenuation coefficients. The values of the coefficients are material specific and are a function of density and effective atomic number. The Pt/C phase is denser and has a higher effective atomic number

compared to ionomer and air, resulting in higher X-ray attenuation; hence, the Pt/C contribution is at the highest grey scale values while the ionomer, with a lower atomic number, is between the air and Pt/C phases. The details on the methodology of assigning grey scale values to each pixel of a 2D XCT micrograph can be found in the literature [56].

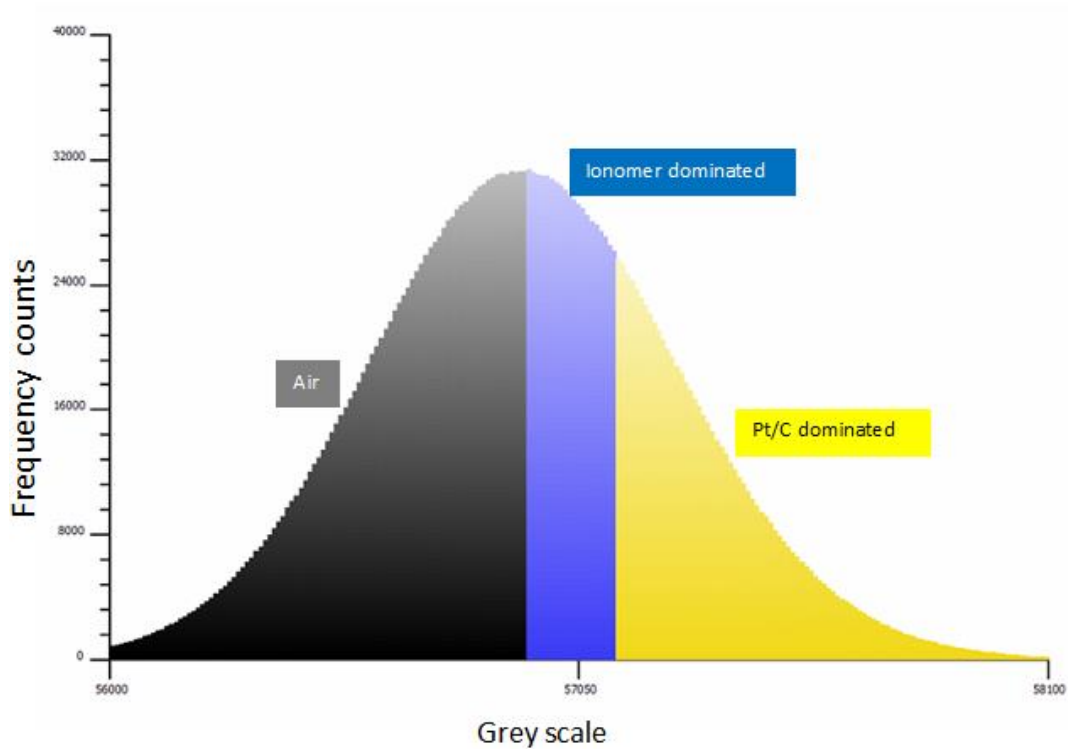


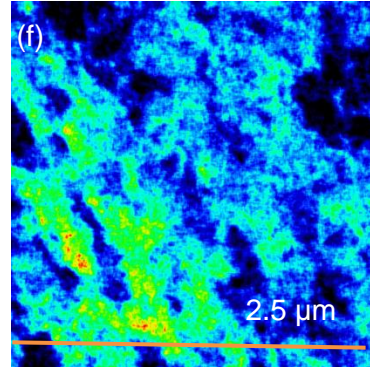
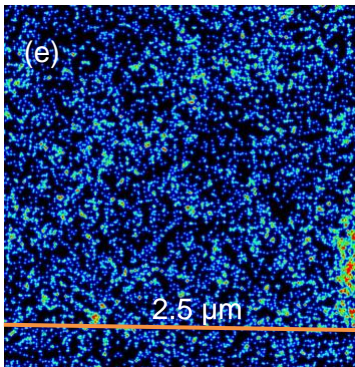
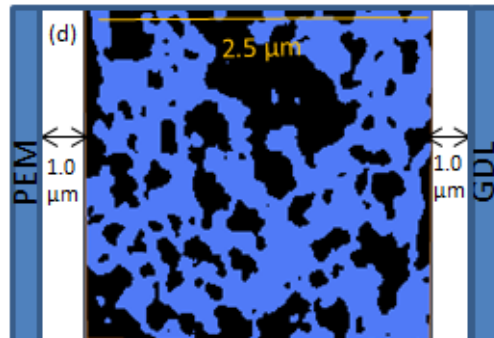
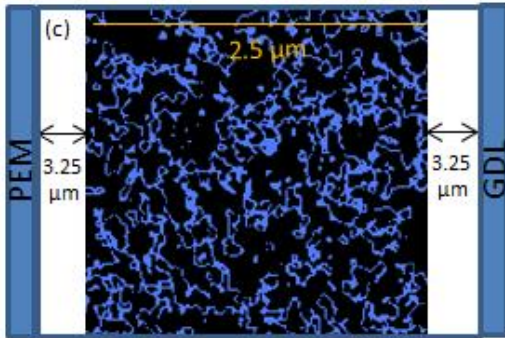
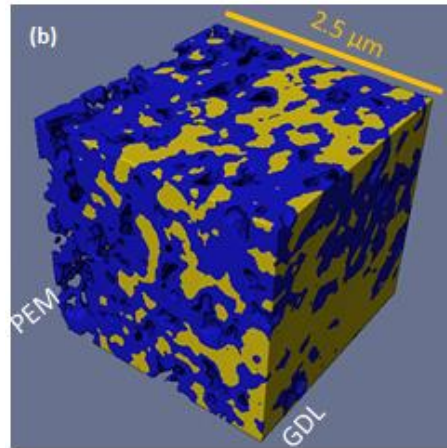
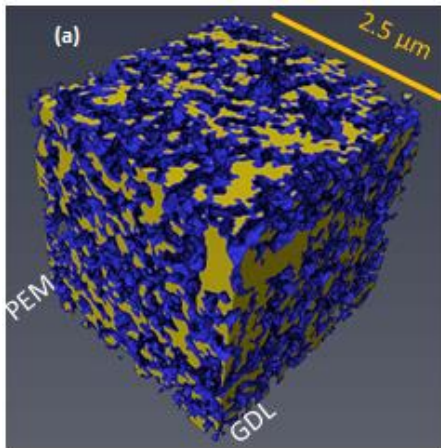
**Figure 15: Grey scale histogram of the cathode catalyst layer phase segmentation with x-axis representing grey scale values and y-axis representing frequency. Air portion is represented by black, ionomer dominated region represented by blue, and Pt/C dominated region is represented by yellow.**

In the analysis of the EOT CCL it was assumed that ionomer loss is negligible during the voltage cycling AST [30] and that the 57% catalyst layer thinning is primarily due to carbon corrosion and associated collapsing of the layer. Equation (9) can thus be derived to calculate the ionomer dominated volume fraction ( $x$ ) at EOT, where  $b$  is the Pt/C to ionomer ratio at BOT,  $a$  is the CL thinning fraction from BOT to EOT, and  $c$  is the total solid volume fraction at EOT. In this study,  $b$ ,  $a$ , and  $c$  were calculated to be 1.23, 0.57, and 0.77 from Section 3.2.1, 3.1, and 3.2, respectively.

$$x+bx(1-a)=c \quad (9)$$

Solving the equation resulted in 51% ionomer dominated volume, which further implies 26% Pt/C dominated volume, given the previously determined porosity of 23% at EOT. The grey scale histogram of the reconstructed EOT 3D sub-domain was then segmented using the same procedure as for the BOT structure. The obtained phase segmented BOT and EOT CCL structures are illustrated in Figure 16. The BOT structure shows a homogenous Pt/C and ionomer dominated phase distribution from the PEM side across to the GDL side of the sub-domain. It can be observed that the ionomer dominated phase forms a film around the Pt/C dominated phase, as normally expected from fabrication. However, in the EOT structure, the distribution of Pt/C and ionomer dominated phases is inhomogeneous.

The comparison of the ionomer dominated phase in Figure 16 (c) for BOT and (d) for EOT visually confirms that the interconnected ionomer dominated structure has increased in volume fraction from 21% to 51%. A supporting TEM analysis and subsequent fluorine elemental mapping using dark field EDX for similar BOT and EOT CCL was obtained and is shown in Figure 16 (e) and (f) respectively. The color scheme used in the elemental map indicates fluorine concentration where red is the most concentrated followed by green and blue. The 2D XCT views of the ionomer dominated phases at BOT and EOT are in good visual agreement with fluorine elemental mapping, where it can be observed that the finer interconnected fluorine structure has become increasingly concentrated and volumized. The increased volume fraction is due to the loss of carbon support from carbon corrosion, resulting in the structure to collapse (i.e., loss of pore space), and increasing the ionomer concentration as the original ionomer amount is retained and packed into a thinner CCL.



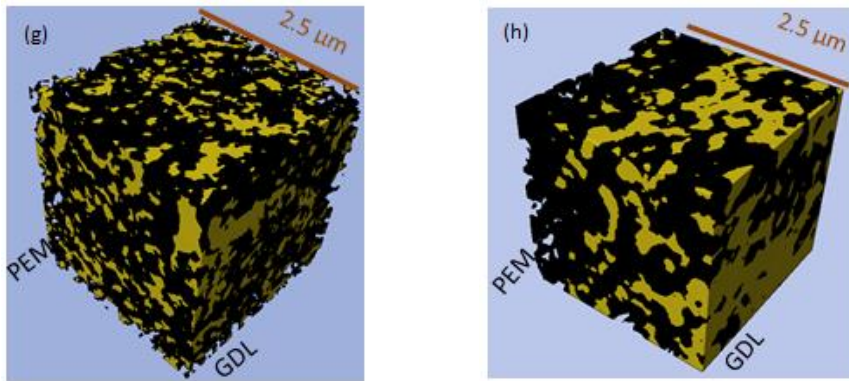


**Figure 16: 3D structure of cathode catalyst layer at (a) BOT and (b) EOT showing Pt/C dominated region as yellow, ionomer dominated region as blue, and pores as black. 2D image highlighting the ionomer dominant phase only from XCT at (c) BOT, (d) EOT, and fluorine elemental mapping obtained from EDX at (e) BOT, (f) EOT indicating highest fluorine concentration with red followed by green and blue, and 3D structure highlighting the Pt/C dominant phase only at (g) BOT, and (h) EOT.**

At EOT, the ionomer dominated phase exhibits large, interconnected features of several hundred nanometers in diameter which can resist the flow of electrons through the electrode, resulting in ohmic loss as indicated by the fuel cell performance in Figure 14. These ionomer rich features are also likely to inhibit reactant gas transport to the remaining active surface and thus be a critical source of mass transport losses in the degraded electrode. The BOT Pt/C dominated phase highlighted in Figure 16 (g) shows a uniform Pt/C size distribution, whereas at EOT (Figure 16 (h)), significant Pt/C particle agglomeration is observed. This observation is in good qualitative agreement with the 44% increase in Pt particle size and 89% loss in ECSA measured by X-ray diffraction (XRD) and cyclic voltammetry, respectively. Pt/C catalyst agglomeration has most likely occurred due to Pt dissolution via Ostwald ripening and/or coalescence of Pt nanoparticles, also known as sintering [22], while the reduced connectivity of the Pt/C phase and the poor local mass transport also contribute to ECSA loss. It can also be noted from Figure 16 (h) that there is a more porous structure and lack of Pt/C dominated phase at the membrane side when compared to the GDL side, which is an indication of higher carbon corrosion and Pt dissolution at the PEM interface, further contributing to kinetic losses in the fuel

cell as seen in the polarization curve at lower current densities in Figure 14. This observation is in good qualitative agreement with 56% decrease in double layer capacitance measured by EIS, indicating carbon oxidation and Pt dissolution [64], and also contributes to ohmic and activation losses as seen in the fuel cell performance curve in Figure 14. The highest rate of oxygen reduction occurs at the PEM interface [65], resulting in higher rate of local water production compared to other regions closer to the GDL, and the likely cause of higher local rate of carbon corrosion.

### 3.1.2.2. Edge of CCL island

A similar procedure was used to acquire tomography data sets of the FIB lift out sample from the edge of an identical cathode catalyst layer island as shown in Figure 17. Post-acquisition 3D image analysis was performed, obtaining a 3D structure of pores and solids. The porosity was calculated to be 35% at location 1 in contrast to 31% at location 2 as shown in Figure 17.

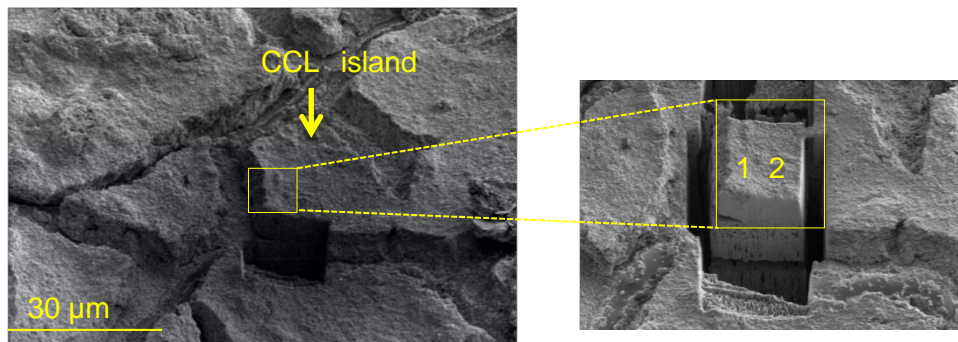


**Figure 17: A FIB lift out of a high potential degraded CCL sample at the edge of the island.**

When comparing this result to the 23% porosity of the sample at the center of CCL island as seen from section 3.1.2.1, a porosity gradient from edge of the island towards the center of the island can be observed with least being at the center. A comparison of the overall pore size distribution between edge of the CCL and the center of CCL shows that the pores in the center are smaller in comparison to the pores in the edges as shown in Figure 18.

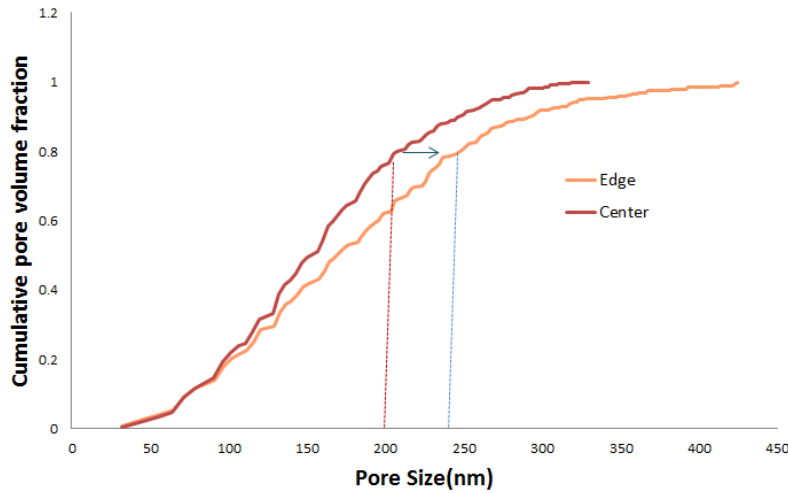


**Figure 18: Cathode catalyst layer pore size distribution at edge vs center of a high potential degraded CCL island.**

These results indicate that the catalyst layer structure is collapsed more at the center of the CCL island forming comparatively smaller pores and lower porosity. The catalyst layer structure at the edge of the island is relatively more porous and is likely due to combined effect of Pt/C erosion and corrosion from water flooding at the cracks. It can be observed from Table 3 that the EOT diffusivity values at the center of an island is lower compared to edge of the island and is due to lower porosity and smaller pore sizes. It can also be noted that the diffusion transport phenomenon is affected the most in the through-plane direction.

	$D_{\text{eff,O}_2}$ (Effective diffusivity) $10^{-7}$ (m <sup>2</sup> /sec)		$D_{\text{eff,O}_2}/D_{\text{O}_2,\text{air}}$ (Relative diffusivity)	
	Edge	Center	Edge	Center
Oxygen	15 24 6.3	2.6 (In-plane) 4.6 (In-plane) 0.5 (Through-plane)	0.05 0.09 0.02	0.01 0.02 0.002
Water Vapor	17 28 7.1	2.9 (In-plane) 5.2 (In-plane) 0.6 (Through-plane)	0.06 0.10 0.02	0.01 0.02 0.002

**Table 3: Diffusivity of oxygen and water vapor at edge and center of the high potential degraded high crack CCL island.**

## 3.2. Effect of upper potential limit

A high catalyst layer crack baseline BOT MEA is subjected to a lower UPL (1.2 V) AST, resulting in a degraded EOT MEA. The lower UPL AST degraded MEA is compared to the baseline higher UPL (1.3 V) AST degraded MEA to understand the differences in degradation due to applied upper potential.

### 3.2.1. Micro scale analysis

A virtually extracted 3D rendering and a cross-sectional view of the images of a 1.2 V degraded catalyst layer can be seen at Figure 19 (a) & (b) respectively. Cracks can be observed in the 3D rendering image at Figure 19 (a) whereas the CCL thickness can be seen at Figure 19 (b).

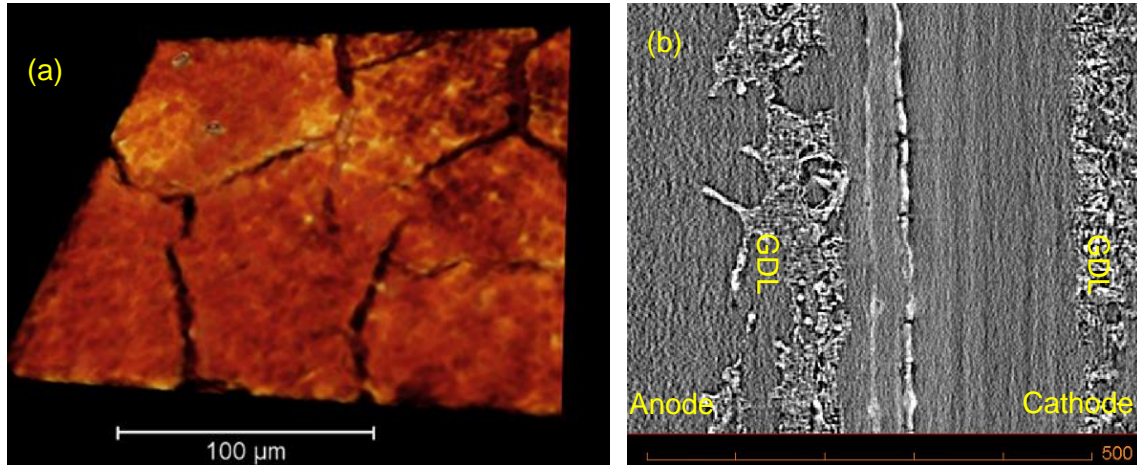


**Figure 19: 3D rendering of 1.2 V degraded cathode catalyst layer at a) and 2D virtual cross-sections of 1.2 V degraded EOT MEA at (b) showing the effects of cathode degradation.**

The total crack surface area fraction was measured to be 10% for 1.2 V degraded CCL in comparison to 6% for BOT CCL as shown in Section 3.1.1; a 1.6x increase in overall crack area for the 1.2 V degraded EOT CCL. In contrast, the total crack surface area fraction for 1.3 V degraded CCL was 30% as shown in Section 3.1.1; a 3x higher crack surface area compared to 1.2 V degraded CCL. The distribution of the crack widths presented in Figure 20 shows an increase in the cracks width from BOT to the 1.2 V degraded EOT CCL, and is highest in the 1.3 V degraded CCL. The cathode catalyst layer shows an uneven layer with gaps throughout its thickness and is indicative of cracks, forming island structures on the surface of the catalyst layer as shown by Figure 19 (a) & (b). The measured EOT thicknesses for 1.2 V degraded CCL is  $9 \pm 1 \mu\text{m}$ ; resulting in 36 % thinning in comparison to 57% thinning 1.3 V degraded CCL as shown in Section 3.1.1. It can be concluded that at lower UPL AST, crack growth and thinning is less severe than at higher UPL.

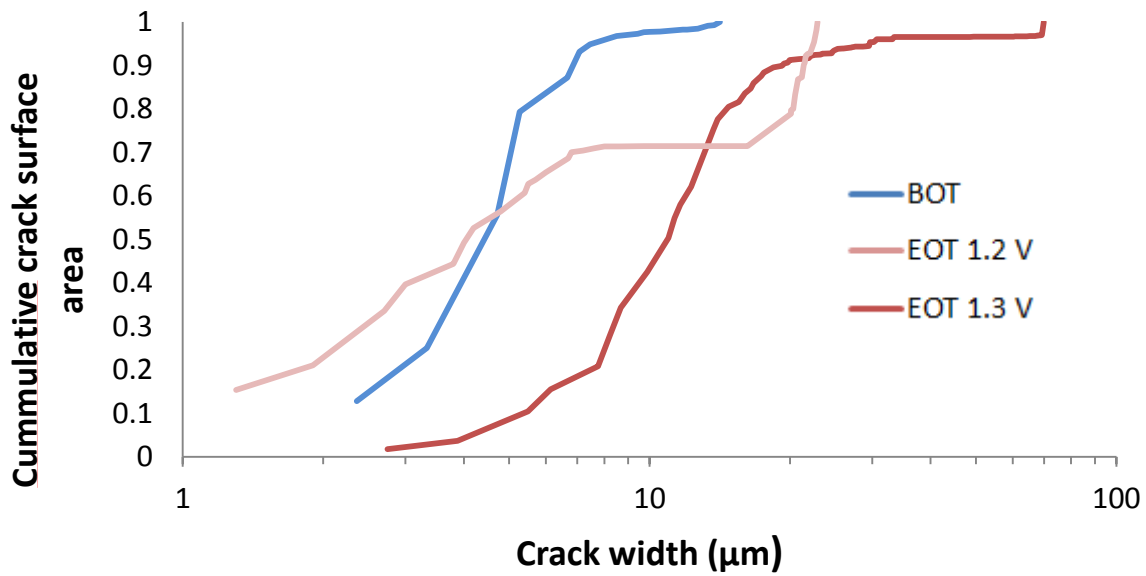


**Figure 20: Normalized cumulative crack surface area of the cathode catalyst layer crack width in baseline BOT, 1.2 V degraded EOT, and 1.3 V degraded EOT.**

### 3.2.2. Nano scale analysis

The HRES absorption contrast mode of the Zeiss Xradia 810 Ultra was used to acquire tomography data sets of the FIB lift out sample from the center of cathode catalyst layer island. A 3D sub-domain of the 1.2 V degraded CCL structure is obtained after image analysis, revealing an in-homogenous network of pores and solids phase in the CL as seen in Figure 21. The 3D structure in Figure 21 (a) is comparatively more compact compared to BOT CCL in Figure 12 (a). It can also be noted that smaller pores in the EOT structure are seen as compared to the BOT structure as shown in Figure 12 (d).

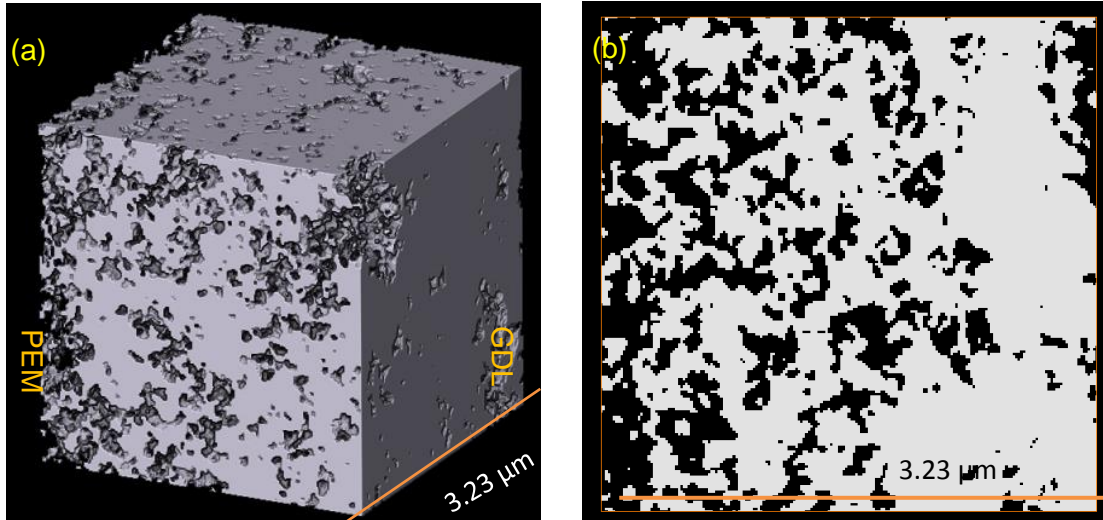


**Figure 21: A 3D structure of the 1.2 V potential degraded EOT CCL indicating PEM and GDL interfaces at (a) and a 2D representation of the CCL at (b) showing the effect of degradation.**

The solid volume fraction for the low potential degraded CCL was found to be 66%; hence, 34% porosity in comparison to 53% porosity at BOT as shown in Section 3.1.2. The calculated porosity of the 1.2 V degraded EOT sub-domain was deemed representative of the overall porosity of the FIB lift out sample after carefully examining the entire FIB lift out sample. A significant porosity gradient was observed across the GDL and PEM interface of the obtained 3D sub-domain. A partial collapsing of the CL structure is seen towards the GDL interface, whereas a more porous structure is observed towards the PEM interface. Carbon corrosion is not a dominant failure mechanism at 1.2 V UPL AST [30], hence loss of carbon solid phase is not solely responsible for such a porous structure at the PEM interface. However, at 1.2 V UPL, platinum dissolution is a dominant failure mechanism in fuel cell electrodes [30], which is a likely factor in contributing to a more porous structure at the PEM interface. The comparison of the overall pore size distribution between the BOT and the two different upper potential AST degraded CCLs indicates that the pores in the 1.2 V degraded CCL are smaller, whereas the pores in the 1.3 V degraded CCL are bigger as seen in Figure 22. This result in addition to overall porosity decrease and CCL thinning seen from micro scale analysis for 1.2 V degraded

CCL is indicative of catalyst layer structure collapsing, resulting in smaller pores. However, only partial collapsing of the catalyst layer structure was observed as seen in Figure 21 (a), indicating a need for further investigation, and will be discussed further in Section 3.2.2.1. In contrast, at 1.3 V UPL AST, the pores are comparatively bigger, indicating larger pores are likely due to carbon corrosion and Pt dissolution prior to and after collapsing of the structure as discussed in Section 3.1.2.1.

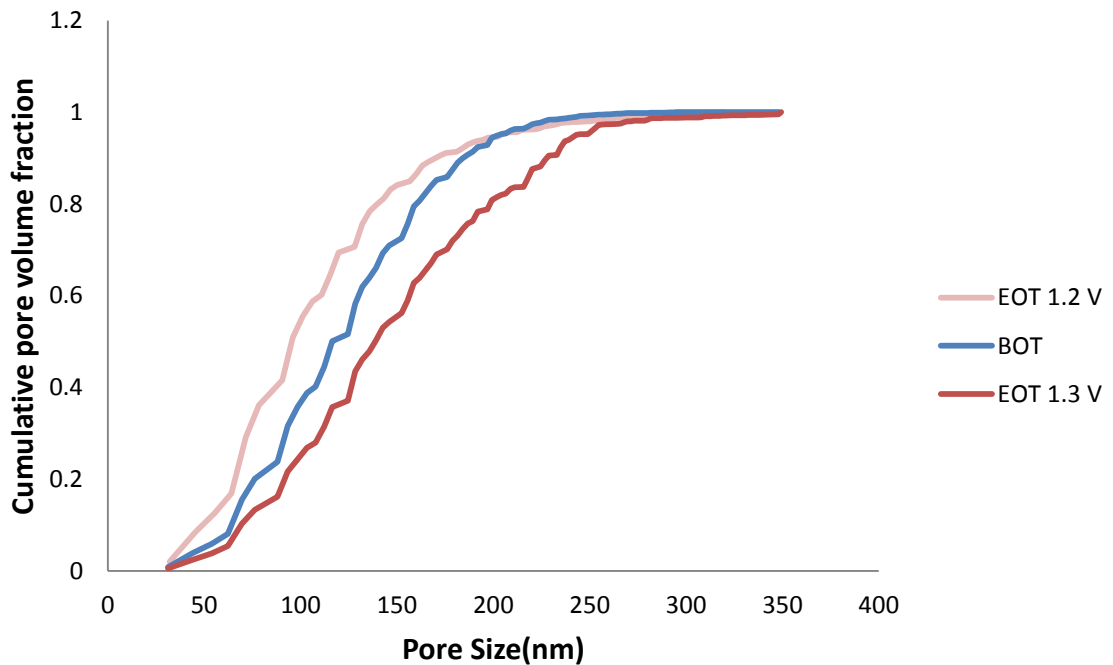


**Figure 22: Cathode catalyst layer pore size distribution at baseline BOT, 1.2 V degraded EOT, and 1.3 V degraded EOT.**

The numerical simulations used to calculate the effective diffusivity of oxygen and water vapor in the three principal through-plane and in-plane directions of the catalyst layer sub domain for the BOT CCL was found to be isotropic whereas for the 1.2 V degraded CCL, it was found to be anisotropic with respect to the through-plane and in-plane directions, as shown by the results reported in Table 4. It can be observed that 1.2 V degraded EOT diffusivity values for

the through plane direction are lower than for BOT due to the lower porosity and smaller pores: overall, the EOT through-plane diffusivities are an order of magnitude lower than at BOT, while the in-plane diffusivities at EOT are comparable to BOT. The more severe reduction in the through-plane direction is most likely due to the partial collapsing of the cathode catalyst layer structure from carbon corrosion. Hence, the diffusion transport phenomenon is affected the most in the through-plane direction. It can be observed from Table 2 and Table 4 that diffusivities for 1.3 V degraded CCL are lower compared to 1.2 V degraded CCL in both in-plane and through-plane directions.

	$D_{\text{eff,O}_2}$ (Effective diffusivity) $10^{-5}$ (m <sup>2</sup> /sec)		$D_{\text{eff,O}_2}/D_{\text{O}_2,\text{air}}$ (Relative diffusivity)	
	BOT	EOT (1.2 V)	BOT	EOT (1.2 V)
Oxygen	0.2	0.3 (In-plane) 0.2 (In-plane) 0.03 (Through-plane)	0.06	0.1 0.06      0.01
Water Vapor	0.2	0.4 (In-plane) 0.2 (In-plane) 0.04 (Through-plane)	0.06	0.1 0.06 0.01

**Table 4: Diffusivity of oxygen and water vapor in CCL at baseline BOT and a low potential degraded EOT.**

The reduction of CCL diffusivity in the through plane direction will therefore contribute to fuel cell performance losses at EOT as seen in Figure 23, where the voltage loss in the 1.3 V UPL degraded EOT MEAs is highest when compared to original performance of the pristine BOT MEA and 1.2 V UPL degraded EOT MEA at similar current densities.

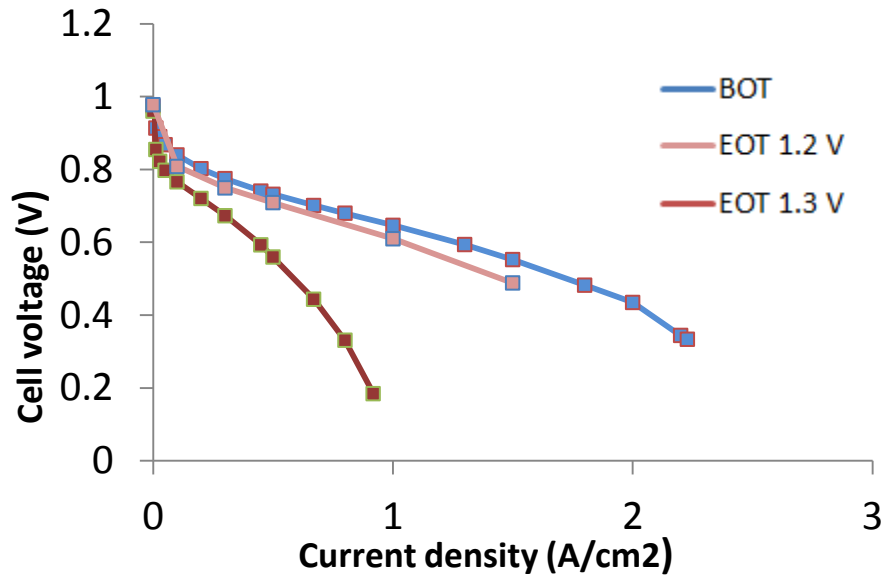
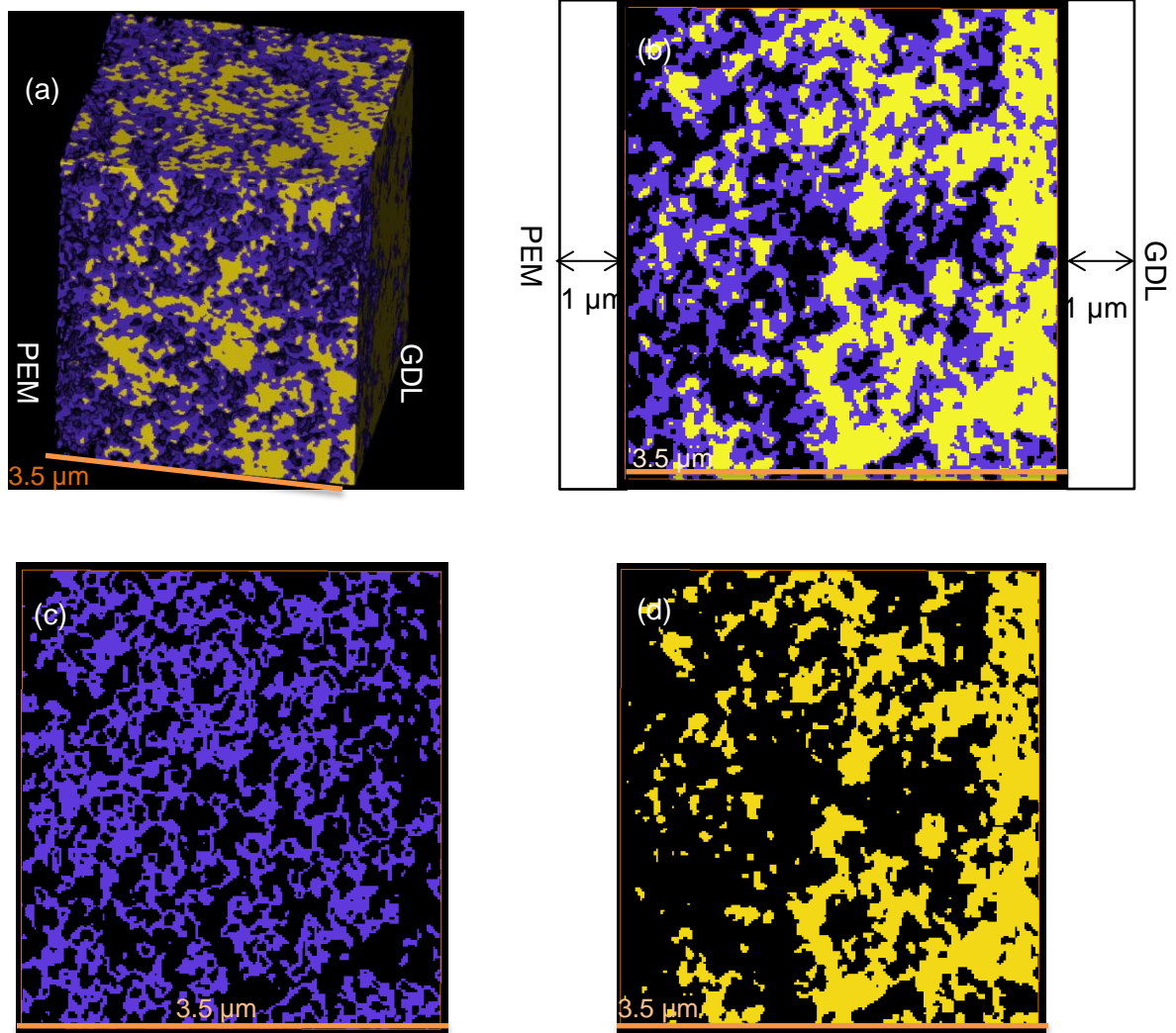


Figure 23: A fuel cell polarization curve for baseline BOT, 1.2 V degraded EOT, and 1.3 V degraded EOT MEA's showing higher voltage drop at 1.3 V EOT in comparison to 1.2 V EOT.

### 3.2.2.1. Catalyst layer segmentation

A similar approach as discussed in Section 3.1.2.1.1 was used to perform segmentation of EOT CL structure into pores, ionomer dominated phase, and Pt/C dominated phase. Equation 9 was used to obtain 37% ionomer dominated volume and 29% Pt/C dominated volume while 34% pore volume was calculated in Section 3.2.2. The obtained phase segmentation of 1.2 V degraded EOT CCL 3D sub domain is shown in Figure 24 (a).



**Figure 24: A 1.2 V degraded 3D phase segmented CCL structure at (a), 2D representation of the structure indicating imaging location from the PEM and GDL interfaces at (b), 2D representation of the ionomer dominated phase at (c), and 2D representation of the Pt/C dominated phase at (d), where blue is ionomer dominated, yellow is Pt/C dominated, and black is pores.**

The 1.2 V degraded EOT 3D structure shows a relatively inhomogeneous distribution of ionomer and Pt/C dominated phases as compared to BOT while relatively homogenous as compared to 1.3 V degraded EOT as seen in Section 3.1.2.1.1. The 2D representation of the structure in Figure 24 (b) shows a Pt/C depleted region close to PEM interface while Pt/C rich region towards the GDL interface. Figure 24 (c) shows a homogenous distribution of interconnected ionomer dominated structure which has increased in volume fraction from 21%

at BOT as seen in Section 3.1.2.1.1 to 37% at EOT. The ionomer volume fraction at 1.2 V degraded CCL is comparatively lower in comparison to 51% at 1.3 V degraded CCL as seen in Section 3.1.2.1.1, indicating lower ohmic losses from electron resistance and lower mass transport losses from gas flow resistance to the reaction sites for 1.2 V degraded CCL as seen in the fuel cell performance curve in Figure 23.

The 2D Pt/C images of the structure at Figure 24 (d) for 1.2 V degraded EOT shows Pt/C agglomeration close to the GDL interface while possible Pt dissolution and carbon corrosion close to the PEM interface. This observation is in good qualitative agreement with the 40% increase in Pt particle size and 57% loss in ECSA which is lower in comparison to 44% increase in Pt particle size and 89% loss in ECSA for 1.3 V degraded CCL, further contributing to lower ohmic losses for 1.2 V degraded CCL as seen in the fuel cell performance curve in Figure 23. However, since Pt dissolution is dominant at 1.2 V UPL AST [30], the visual observation of higher carbon corrosion close to PEM interface might not be conclusive since Pt particles contribution to the overall grey scale value of Pt/C is significant and the absence of Pt close to the interface might possibly cause the carbon particles, which attenuates the X-ray less than ionomer to be mixed with partial air voxel, resulting in lower overall grey level voxel value, and consequently getting removed during air/solid segmentation. This theory also explains why a significant porosity gradient was observed across the CCL 3D sub-domain as discussed in Section 3.2.2.

### **3.3. Effect of pre-existing cracks**

A BOT MEA with lower catalyst crack surface area in comparison to the baseline BOT MEA is subjected to a 1.3 V AST, resulting in a degraded EOT MEA. The low crack BOT and EOT MEA are further compared to a baseline high crack BOT and EOT MEA, to understand the differences in degradation due to variant catalyst surface area cracks.

### 3.3.1. Micro scale analysis

A comparison of the reconstructed surface views for the BOT and EOT low crack CCL at the micro scale can be seen in Figure 25 (a) & (b). The initial mud cracks [31] are seen in the BOT sample which may be due to stress and strain during the manufacturing process attributable to solvent evaporation [62]. However, in the EOT sample, mud cracks appear to be more prevalent, and the surface of the catalyst layer can be observed to form island structures.

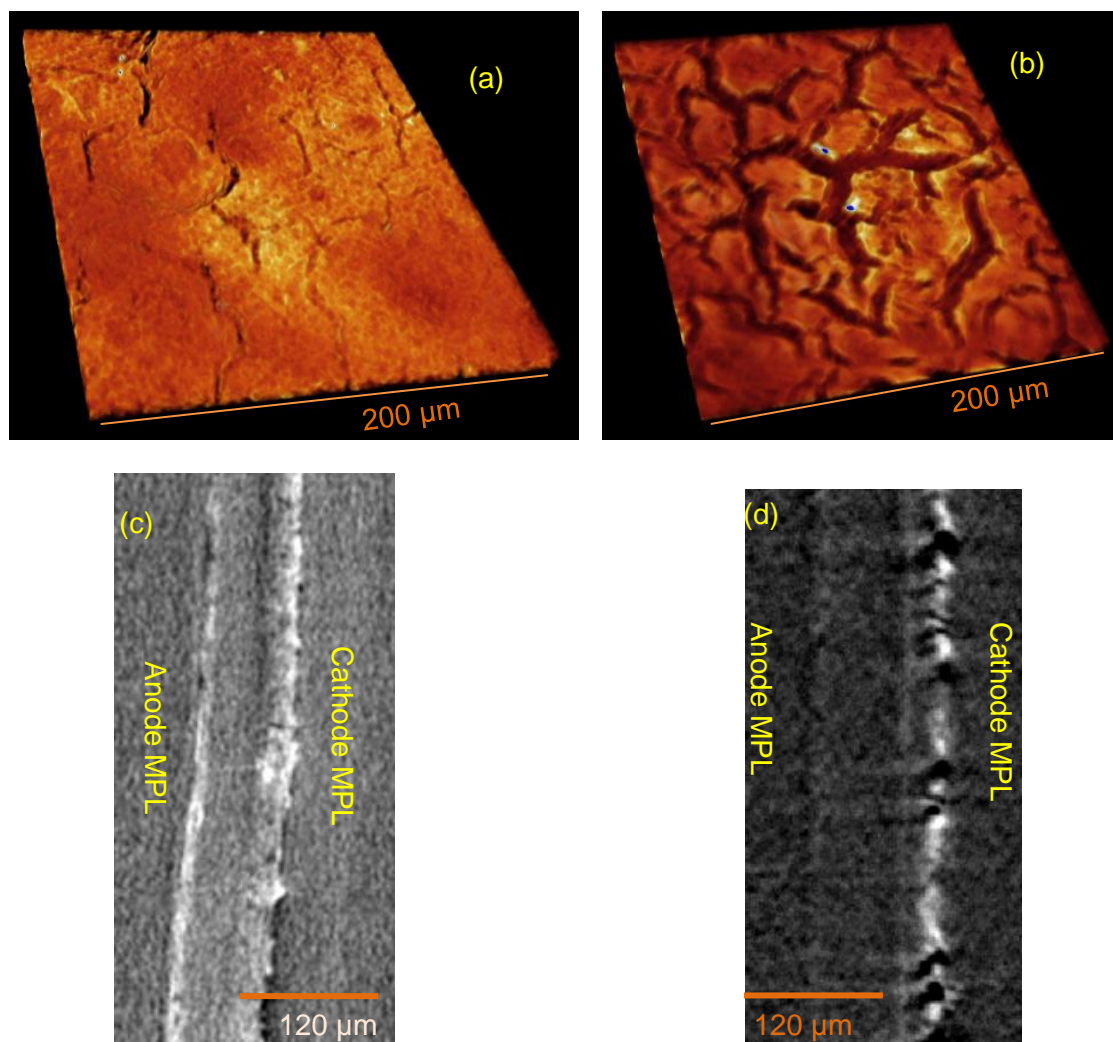


**Figure 25: 3D rendering of cathode catalyst layers at a) low crack BOT MEA, b) low crack degraded EOT MEA and 2D virtual cross-sections of (c) low crack BOT MEA and (d) low crack degraded EOT MEA showing the effects of cathode corrosion.**

The total crack surface area fraction was measured to be 3% and 13% for the BOT and EOT CCL respectively; a 5.5x increase in crack area for the EOT sample. The distribution of the crack widths presented in Figure 26 shows slight increase in the crack width from BOT to EOT. Figure 25 (c) and (d) shows a cross-sectional view of the reconstructed images of the full BOT and EOT MEAs. The cathode catalyst layer in the EOT shows an uneven layer with gaps throughout its thickness when compared to BOT and is indicative of cracks. In addition, a thin, bright layer observed close to the cathode catalyst layer interface is indicative of PITM, associated with Pt dissolution from the cathode catalyst layer. The measured BOT and EOT CCL thicknesses was  $14 \pm 1 \mu\text{m}$  and  $6 \pm 1 \mu\text{m}$  respectively; resulting in 57 % thinning.

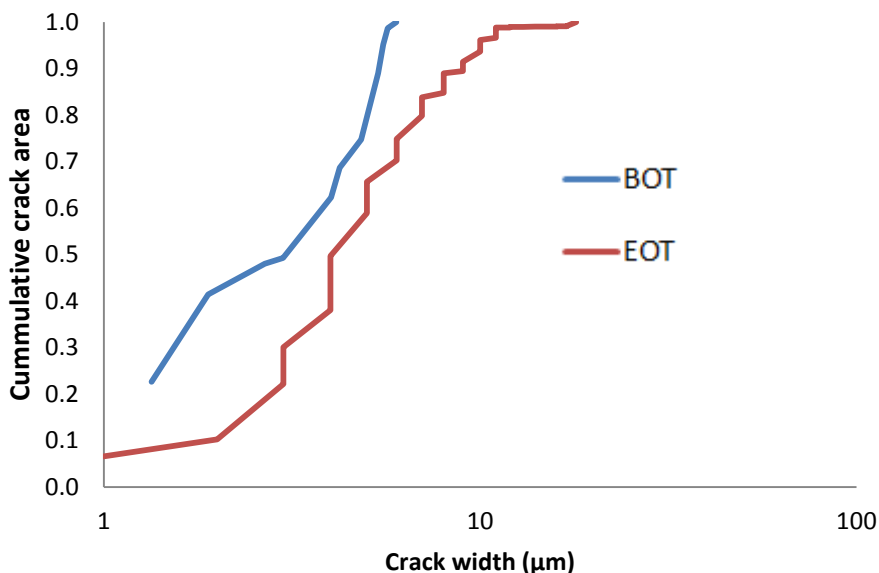


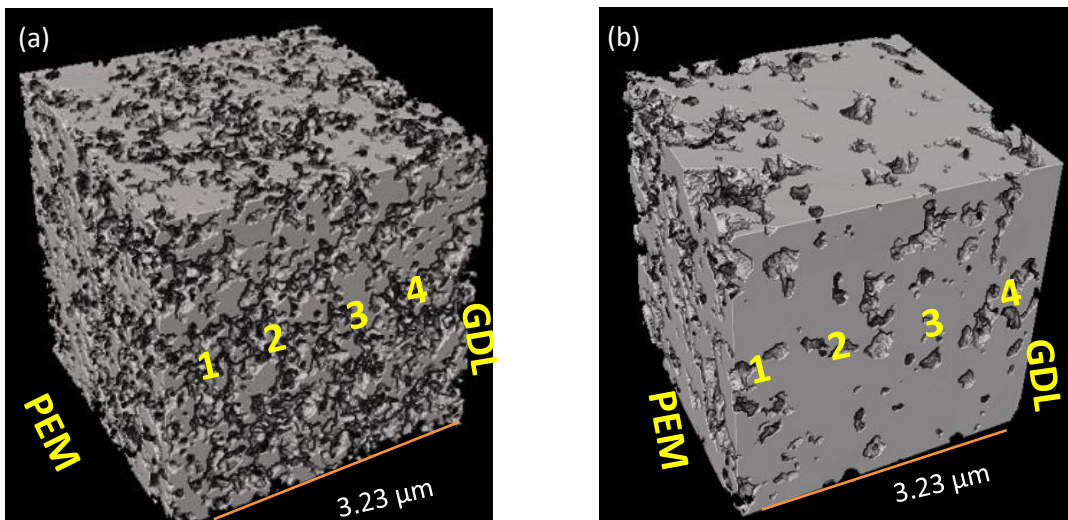
**Figure 26: Normalized cumulative crack surface area of the cathode catalyst layer crack width in low crack BOT and low crack degraded EOT MEA.**

It can be observed that the total crack surface area for low crack BOT CCL is only 3% compared to 6% for high crack BOT CCL as seen in Section 3.1.1, which may be attributed to the manufacturing processes [66]. In addition, the total crack surface area for low crack EOT CCL is 13% compare to 30% for high crack EOT CCL as seen in Section 3.1.1. It can be concluded that the rate of increase in CCL crack area for both degraded electrodes are

comparable. However, the overall crack surface area for the high crack EOT CCL is significantly higher which can lead to water flooding [67], and consequently result in gas transport resistance [68]. Additionally, cracks can lead to increased resistance within catalyst layers [68], and areas susceptible to catalyst erosion [32]. Catalyst layers with higher catalyst crack area show higher carbon corrosion degradation [33]. Hence, catalyst layers with low crack surface area are desirable.

### 3.3.2. Nano scale analysis

A 3D sub-domain of the BOT CCL structure is obtained from image analysis of 3D tomography data sets, revealing a homogenous network of pores and solids phase in the CL as seen in Figure 27 (a). A similar procedure yielded a two phase (solid, pore) 3D sub-domain of the EOT CCL structure, which shows a more compact structure compared to BOT as shown in Figure 27 (b). A uniform porosity distribution across the 3D sub-domain of the BOT CCL can be seen as shown in Figure 27 (c) whereas the structure of the EOT CCL is inhomogeneous as seen through the non-uniformity of porosity across 3D sub-domain in Figure 27 (d).



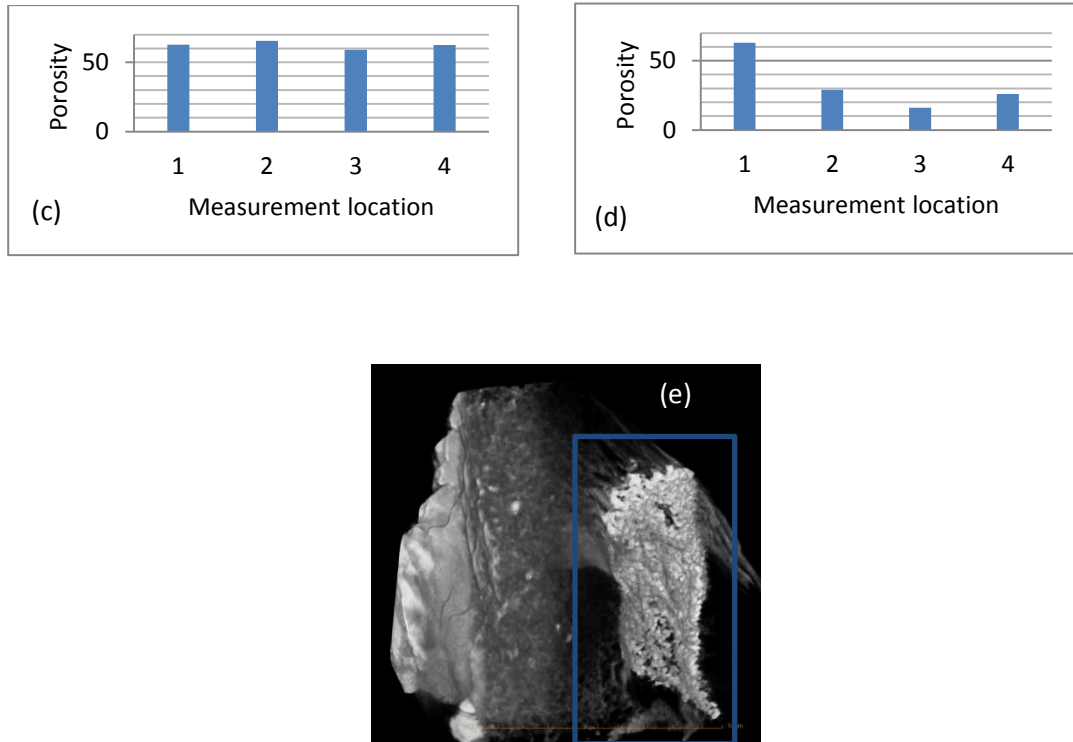


**Figure 27: A 3D structure of the CCL indicating the PEM & GDL interfaces, porosity measurement locations, and porosity chart at low crack BOT (a) & (c) and at low crack degraded EOT (b) & (d). PITM band (indicated by blue box) at (e) is formed in the membrane of the low crack degraded EOT CCL after catalyst layer degradation.**

At EOT, it can be noted that more porous structure is seen closer to the PEM interface in comparison to the GDL interface, which is likely due to the higher rate of oxygen reduction reaction at the PEM interface [65] resulting in locally enhanced carbon corrosion rate. In addition, the formation of a Pt band in the membrane from Pt migration as shown by Figure 27 (e) is likely a contributing factor to the more porous structure closer to the PEM interface of the CCL. Micro scale analysis also supports this finding as PTIM is seen in Figure 25 (d). The overall volume fraction for the BOT CCL sub domain was found to be 40%; hence, 60% porosity. In contrast, the overall volume fraction for the EOT CCL sub domain was found to be 74%; hence, 26% porosity. It is thus evident that substantial pore space has been lost during the degradation process, indicating collapsing of the catalyst layer structure. The comparison of the pore size distributions of the BOT and EOT CCLs indicates that the EOT material contains

larger pore sizes, as shown in Figure 28. New pores may have formed in the EOT catalyst layer after redistribution of the structure following carbon corrosion and compaction. Larger pores were not expected in a comparatively compact catalyst layer structure; however, larger pores may have mostly formed closer to the PEM interface prior to and after collapsing from carbon corrosion and Pt dissolution.

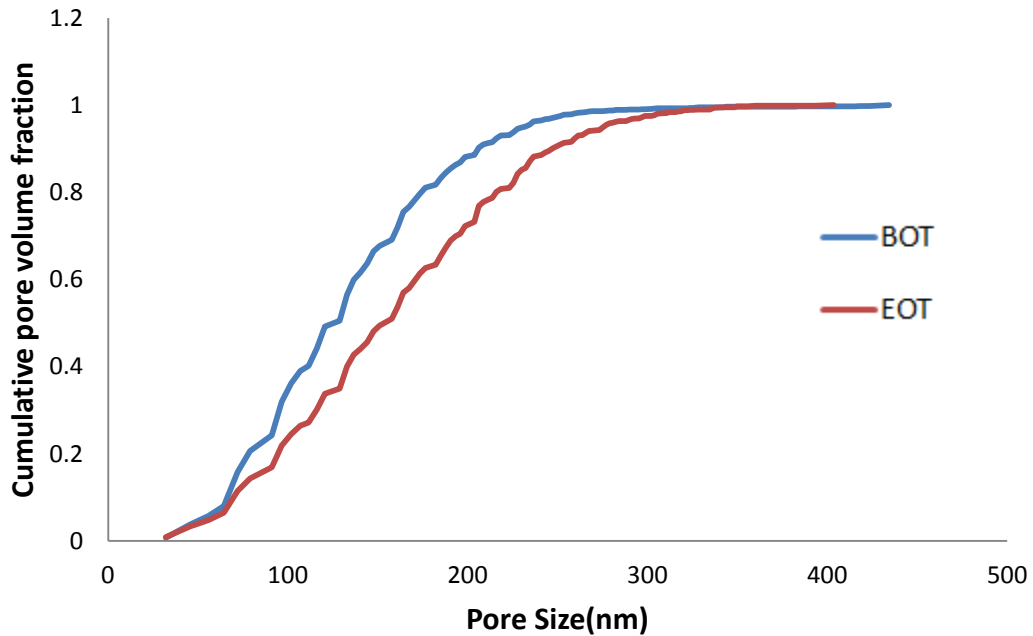


**Figure 28: Cathode catalyst layer pore size distribution at low crack BOT and 1.3 V degraded low crack EOT.**

Numerical simulations were used to estimate the effective diffusivity through the catalyst layer sub domain. In the BOT sub-domain, the effective diffusivity of oxygen and water vapor was found to be isotropic whereas in the EOT sub-domain it was found to be anisotropic in all directions, as shown in Table 5. It can be observed that the EOT diffusivity values are lower compared to BOT and are due to lower porosity. It can also be noted that the diffusion transport phenomenon is affected the most in the through-plane direction.

	$D_{\text{eff,O}_2}$ (Effective diffusivity) $10^{-5} \text{ (m}^2/\text{sec)}$		$D_{\text{eff,O}_2}/D_{\text{O}_2,\text{air}}$ (Relative diffusivity)	
	BOT	EOT	BOT	EOT
Oxygen	1	0.2 (In-plane) 0.1 (In-plane) 0.05 (Through-plane)	0.5	0.07 0.05 0.02
Water Vapor	1	0.2 (In-plane) 0.1 (In-plane) 0.05 (Through-plane)	0.4	0.07 0.05 0.02

**Table 5: Diffusivity of oxygen and water vapor of a low crack CCL at BOT and a 1.3 V degraded low crack EOT.**

A 62% increase in Pt particle size and 86% loss in ECSA for the degraded CCL were measured by XRD and CV respectively. A 53% decrease in double layer capacitance was also measured by EIS, indicating carbon oxidation and Pt dissolution [64]. The reduction in CCL diffusivity, ECSA, and double layer capacitance will therefore contribute to fuel cell performance losses at EOT as seen in Figure 29, where the voltage loss in the degraded EOT MEA is significant when compared to the original performance of the pristine BOT MEA at similar current densities. It can also be observed that the fuel cell voltage drop at higher current density is comparatively greater, indicating dominance of mass transport losses at higher current densities, which can be attributed to decrease in effective diffusivity of oxygen and water vapor. Furthermore, the reduction in double layer capacitance indicates decrease in Pt/C surface area, contributing to activation and ohmic losses as seen in the fuel cell performance curve in Figure 29.

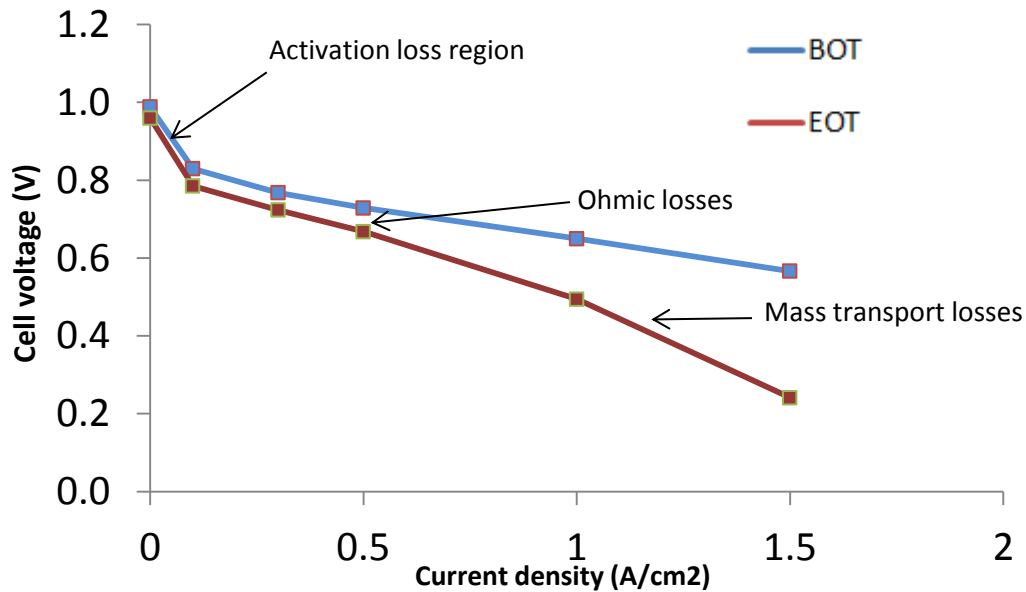


**Figure 29: A fuel cell polarization curve comparison at low crack BOT and low crack degraded EOT showing the effect of reduction in CCL ECSA and diffusivity on the performance of the fuel cell.**

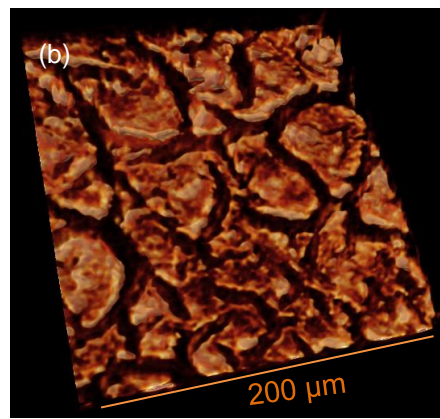
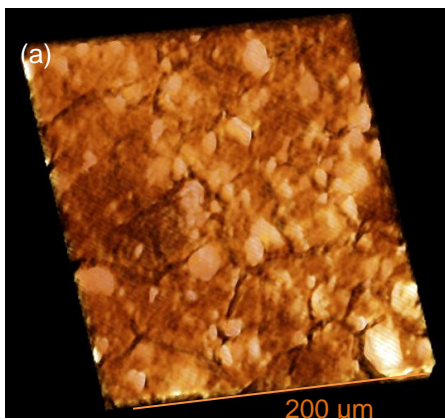
It can be observed that the overall porosity of a low crack BOT and EOT CCL is 11% higher compared to the baseline high crack BOT and EOT CCL respectively as seen in Section 3.1.2. It seems that the magnitude of cracks surrounding a catalyst layer island plays a role in the porosity of the island since the catalyst layer with lower crack widths seems to have comparatively higher porous island and vice-versa. Therefore, the effective diffusivity of oxygen and water vapor at low crack BOT and EOT are an order of magnitude higher than at high crack BOT and EOT. Overall, it is concluded that higher effective diffusivity will result in better fuel cell performance for low crack BOT and EOT, which can likely be traced back to the uniformity of porosity distribution across the 3D sub-domain.

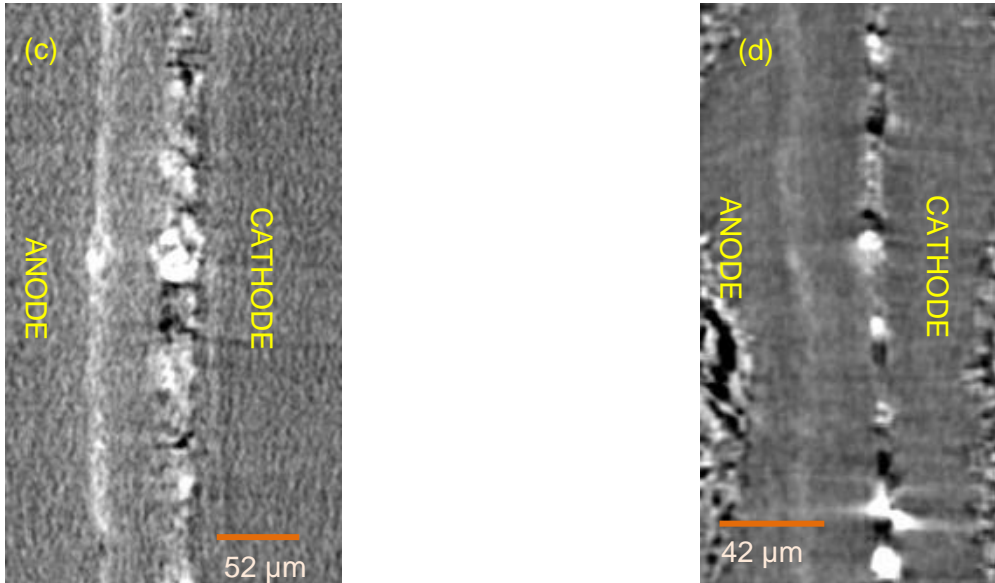
### 3.4. Effect of catalyst support type

A high crack BOT MEA with HSAC catalyst support was subjected to a 1.2 V UPL AST cycling, resulting in a degraded EOT MEA. The HSAC BOT and HSAC EOT MEA were further compared to a baseline BOT MEA and low potential AST degraded MEA with LSAC catalyst support (Section 3.2) to understand the differences in degradation due to the type of carbon support used.

#### 3.4.1. Micro scale analysis

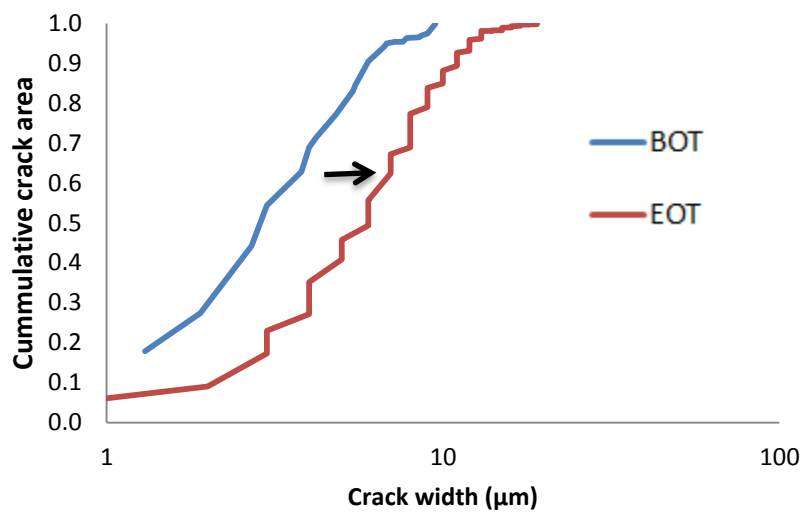
A comparison of the reconstructed surface views for the BOT and EOT CCL at the micro scale can be seen in Figure 30 (a) & (b). The initial mud cracks [31] seen in the BOT sample are similar to previous observation in Section 3.3.1 [62]. In the EOT image, mud cracks appear to be more prevalent, and the remaining catalyst layer material can be observed to form island structures.





**Figure 30: 3D rendering of cathode catalyst layers at a) HSAC BOT MEA, b) HSAC degraded EOT MEA and 2D virtual cross-sections of (c) HSAC BOT MEA and (d) HSAC degraded EOT MEA showing the effects of cathode corrosion.**

The total crack surface area fraction was measured to be 3% and 21% for the BOT and EOT CCL respectively; a 7x increase in crack area for the EOT sample. The distribution of the crack widths presented in Figure 31 shows a considerable increase in the crack width from BOT to EOT.



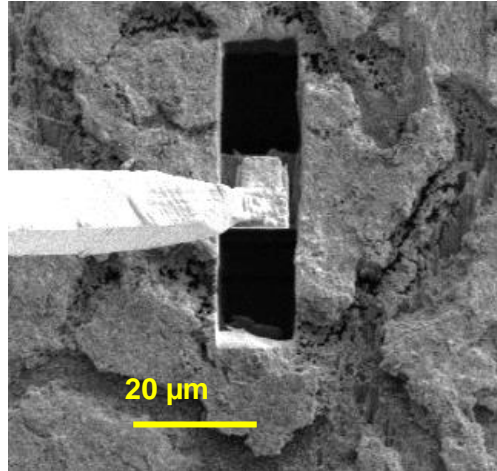
**Figure 31: Normalized cumulative crack area of the cathode catalyst layer crack width in HSAC BOT and HSAC degraded EOT MEA sample.**

Figure 30 (c) and (d) shows a cross-sectional view of the reconstructed images of the full BOT and EOT MEAs similar to Section 3.3.1. The cathode catalyst layer in the EOT shows an uneven layer with gaps throughout its thickness when compared to BOT and is indicative of cracks. In addition, bright spots are observed at the edge of the cracks and are most likely due to locally concentrated platinum [63]. The measured BOT and EOT CCL thickness was  $13 \pm 1 \mu\text{m}$  and  $7 \pm 1 \mu\text{m}$  respectively; resulting in 46 % thinning.

The crack growth and CCL thinning for 1.2 V degraded CCL with HSAC support is significantly higher in comparison to 1.6x and 36% for low potential degraded CCL with LSAC support as seen in Section 3.2.1. A considerably higher degradation rate at low potential AST protocol was not expected, since carbon corrosion is mostly dominant at potentials higher than 1.2 V [30]. However, HSAC support catalyst layer has higher amount of catalyst anchor sites, hence catalyst particles are well dispersed in the carbon support, and are susceptible to higher carbon corrosion rate [69] [70].

### **3.4.2. Nano scale analysis**

The high resolution (HRES) absorption contrast mode of the Zeiss Xradia 810 Ultra was used to acquire tomography data sets of the FIB lift out sample from the center of cathode catalyst layer island for both EOT and BOT as shown in Figure 32. It can be observed that the samples were lifted out from a crack free location for the EOT CCL.



**Figure 32: FIB lift out using a manipulator from the center of CCL island for HSAC degraded EOT.**

A 3D sub-domain of the BOT CCL structure is obtained after post acquisition of the 3D tomography data sets, revealing a homogenous network of pores and solids phase in the CL as seen in Figure 33 (a). A similar procedure yielded a two phase (solid, pore) 3D sub-domain of the EOT CCL structure, which shows a more compact structure compared to BOT as shown in Figure 33 (b). Additionally, the structure also shows a network of pores and solids phase which is inhomogeneous. The volume fraction for the BOT 3D sub domain was found to be 43%; hence, 57% porosity. In contrast, the volume fraction for the EOT 3D sub domain was found to be 66%; hence, 34% porosity. It is thus evident that substantial pore space was lost during the cathode degradation process, indicating that the CCL structure collapsed due to loss of solid phase integrity from carbon corrosion. The CCL thinning measured from the micro scale analysis also supports this finding.

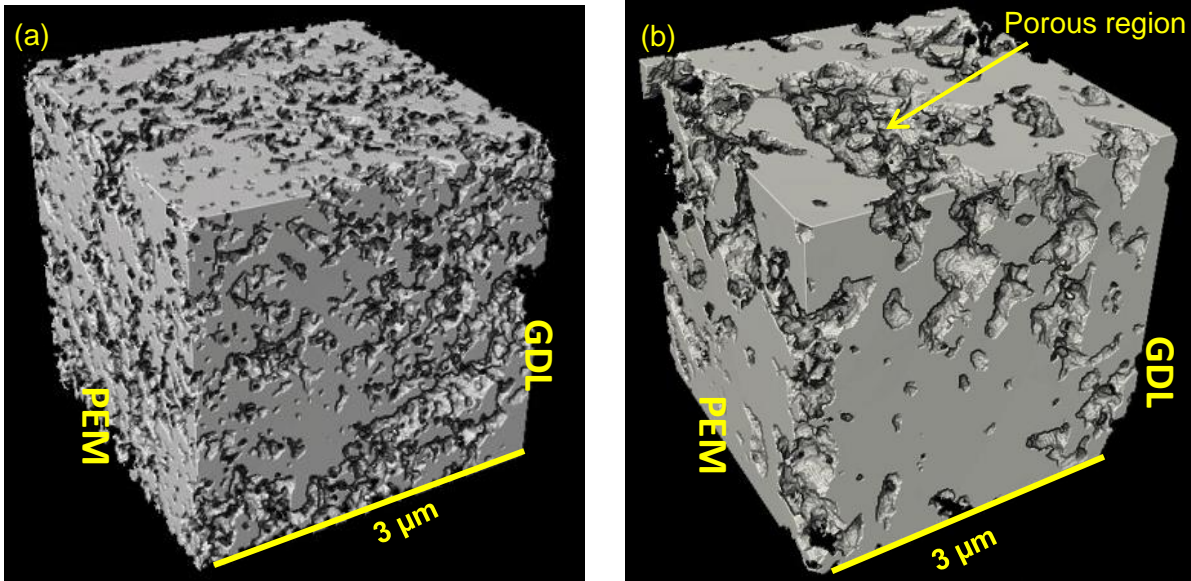


**Figure 33: A 3D structure of CCL sub domain indicating the PEM and GDL interfaces at (a) HSAC BOT and at (b) HSAC degraded EOT.**

The comparison of the PSD between BOT and EOT samples indicates that the EOT material contains larger pore sizes as seen in Figure 34. Larger pores were not expected since the catalyst layer had collapsed in the through plane direction; however, larger pores may have formed prior to and after collapsing from carbon corrosion and Pt dissolution and are most likely located in the porous regions of the EOT sub-domain as shown in Figure 33 (b)

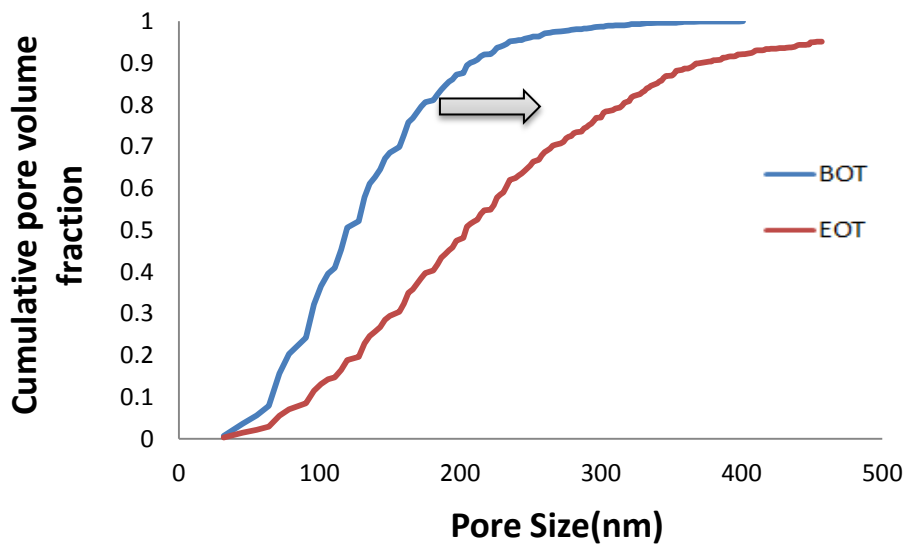


**Figure 34: Cathode catalyst layer pore size distribution at HSAC BOT and low potential degraded HSAC EOT showing larger pores at EOT.**

Numerical simulations were used to estimate the effective diffusivity in the catalyst layer sub domain. In the BOT and EOT sample, the effective diffusivity of oxygen and water vapor was found to be isotropic as shown in Table 6. It can be observed that the EOT diffusivity values are lower compared to BOT and are due to lower porosity. Hence, the diffusion transport phenomenon is affected equally in all direction of flow, resulting in mass transport losses in fuel cells.

	<b>D<sub>eff,O2</sub> (Effective diffusivity)</b> <b>10<sup>-5</sup> (m<sup>2</sup>/sec)</b>		<b>D<sub>eff,O2</sub>/D<sub>O2,air</sub></b> <b>(Relative diffusivity)</b>	
	BOT	EOT	BOT	EOT
Oxygen	0.7	0.2	0.3	0.1
Water Vapor	0.7	0.3	0.3	0.1

**Table 6: Diffusivity of oxygen and water vapor of a HSAC CCL at BOT and a degraded HSAC EOT.**

A 174% increase in Pt particle size and 87% loss in ECSA for the degraded CCL were measured similarly as in Section 3.3.2 contributing to kinetic losses in the fuel cell. A 78% decrease in double layer capacitance was measured using EIS indicating further evidence of carbon corrosion and Pt dissolution, and contributing to ohmic and activation losses in the fuel cell. The reduction in CCL diffusivity, ECSA, and double layer capacitance will therefore contribute to fuel cell performance losses at EOT as seen in Figure 35.

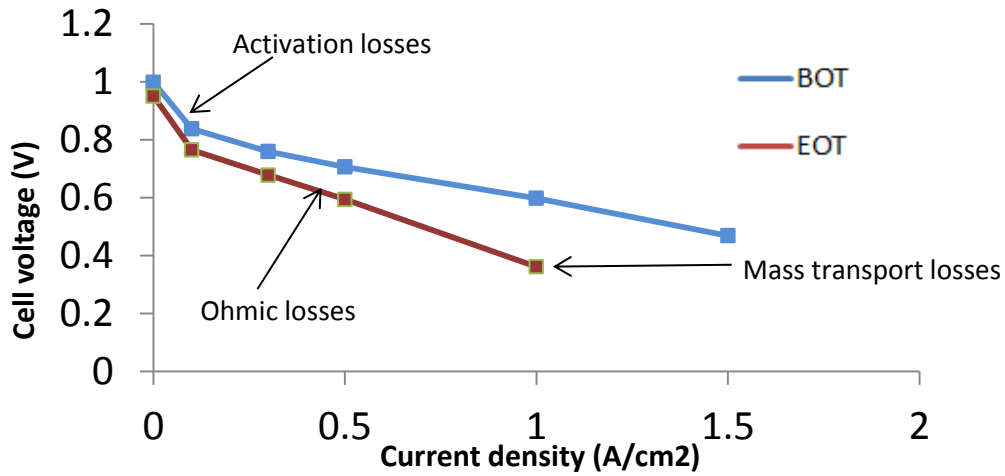


**Figure 35: A fuel cell polarization curve at HSAC BOT and degraded HSAC EOT showing the effect of collapsing of the CL structure on the performance of fuel cell.**

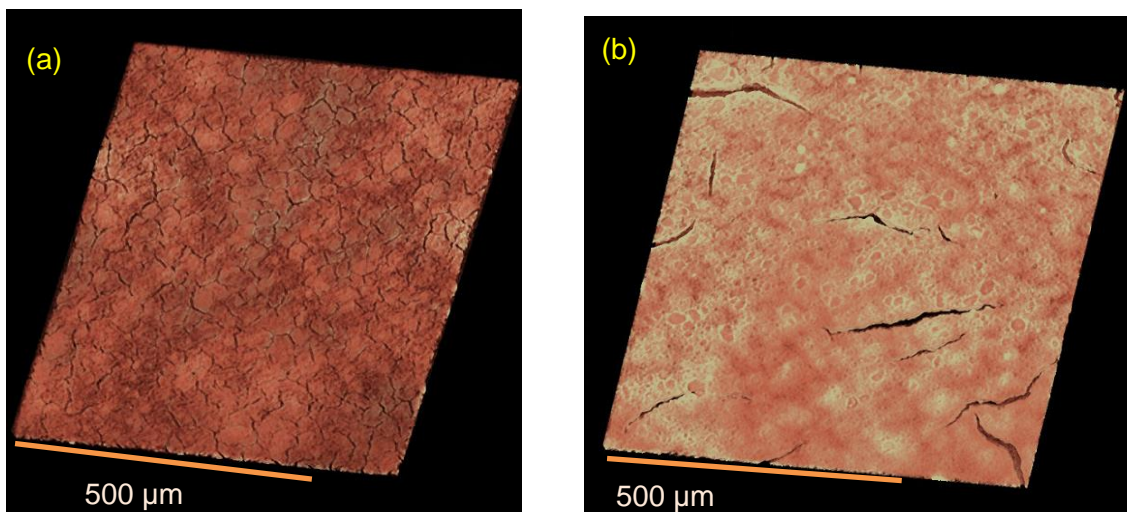
It can be observed that the overall 3D sub domain porosity of HSAC BOT and EOT CCL is 53% and 34% in comparison to 57% and 34% for LSAC BOT and EOT CCL respectively as studied in Section 3.2.1. However, Pt particle size and ECSA loss is significantly higher for HSAC EOT CCL, which indicates higher carbon corrosion rate resulting in detachment of Pt particles, and forming agglomerates. In contrast, the effective diffusivity of oxygen and water vapor at HSAC EOT CCL are an order of magnitude higher than at LSAC EOT CCL in the through-plane direction respectively, which is most likely due to larger pore sizes, resulting in comparably lower mass transport losses. Overall, it can be concluded that despite similar porosity for LSAC EOT and HSAC EOT CCL, it is evident through the diagnostics that carbon corrosion is comparably higher for HSAC EOT CCL, resulting in larger pore formation prior to and after collapsing of the catalyst layer structure as discussed earlier.

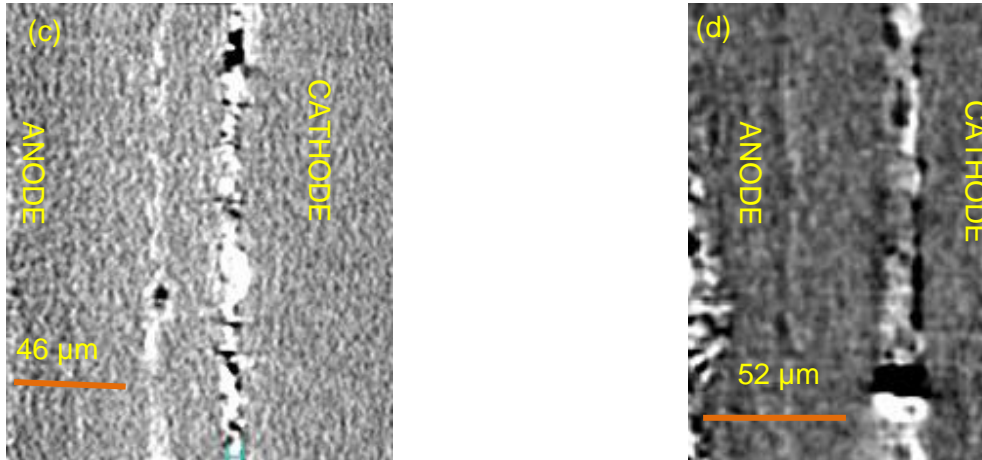
### 3.5. Effect of ionomer loading amount

A high ionomer loading BOT MEA is subjected to a 1.2 V potential AST cycling, resulting in a degraded EOT MEA. Subsequently, the BOT and EOT MEA are compared to the baseline BOT and a 1.2 V UPL AST degraded EOT MEA with comparatively lower ionomer loading (Section 3.2) to understand the differences in CCL degradation.

#### 3.5.1. Micro scale analysis

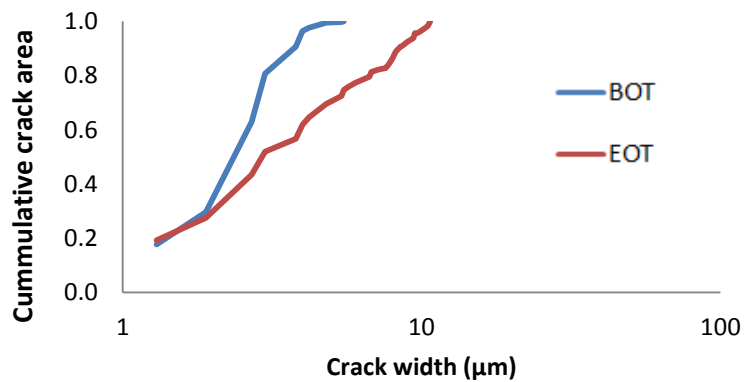
A comparison of the reconstructed surface views for the BOT and EOT CCL at the micro scale can be seen in Figure 36 (a) & (b). The initial mud cracks [31] are seen in the BOT sample which is similar to the previous observation in Section 3.4.1 [62]. However, in the EOT sample, some of the mud cracks on the surface of the catalyst layer can be observed to elongate into “I” shape cracks.





**Figure 36: 3D rendering of cathode catalyst layers at a) high ionomer BOT sample, b) high ionomer degraded EOT sample and 2D virtual cross-sections of (c) high ionomer BOT MEA and (d) high ionomer degraded EOT MEA showing the effects of cathode corrosion.**

The total crack surface area fraction was measured to be comparable at 10% and 9% for the BOT and EOT CCL respectively. However, the distribution of the crack widths presented in Figure 37 shows an increase in the crack width from BOT to EOT, which can be attributed to a joint catalyst layer failure mode in the form of bulk carbon corrosion and local erosion [32] from water flooding in the pre-existing “I” crack and mud cracks.



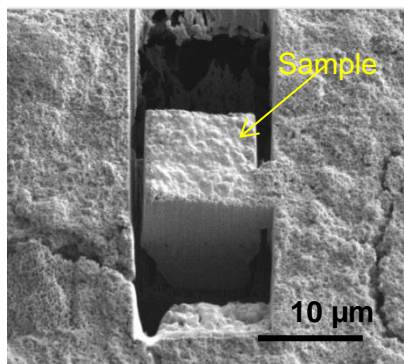
**Figure 37: Normalized cumulative crack surface area of the cathode catalyst layer crack width in high ionomer BOT and high ionomer degraded EOT MEA.**

Figure 36 (c) and (d) shows a cross-sectional view of the reconstructed images of the full BOT and EOT MEAs. The cathode catalyst layer at both BOT and EOT shows an uneven layer

with gaps throughout its thickness and are indicative of the “I” and mud cracks. The measured BOT and EOT CCL thicknesses was  $11 \pm 2 \mu\text{m}$  and  $12 \pm 2 \mu\text{m}$  respectively; which is comparable. The CCL thinning with lower ionomer loading as seen in Section 3.2.1 is 36% in comparison to no thinning with higher ionomer loading. Hence, it can be concluded that higher ionomer loading in the catalyst layer may be beneficial in preventing thinning.

### 3.5.2. Nano scale analysis

The high resolution (HRES) absorption contrast mode of the Zeiss Xradia 810 Ultra was used to acquire tomography data sets of the FIB lift out sample from the center of cathode catalyst layer island as shown in Figure 38.



**Figure 38: FIB lift out sample of high ionomer BOT CCL from the center of CCL island.**

A 3D sub-domain of the BOT CCL structure is obtained after image analysis, revealing a non-homogenous network of pores and solids phase in the CL as seen in Figure 39 (a). A similar procedure yielded a two phase (solid, pore) 3D sub-domain of the EOT CCL structure, which also shows a non-uniform distribution of pores and solids across the 3D sub-domain as shown in Figure 39 (d).

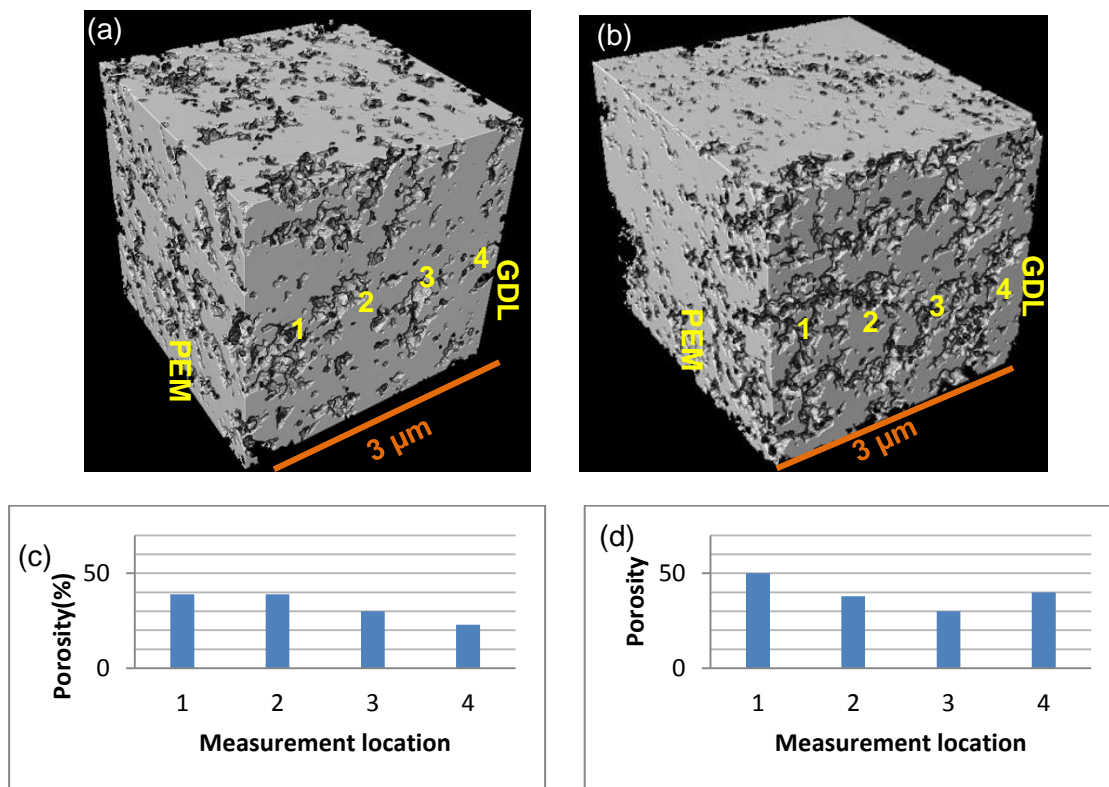


**Figure 39: A 3D structure of the CCL indicating the PEM and GDL interfaces and porosity measurement location at high ionomer BOT (a) & (c) and at high ionomer degraded EOT (b) & (d).**

The overall volume fraction for the BOT 3D sub domain was found to be 65%; hence, 35% porosity. Similarly, the overall volume fraction for the EOT 3D sub domain was found to be 66%; hence, 34% porosity. These results also support the micro scale finding in Section 3.2.1, where CCL thinning was not observed since it is evident that overall catalyst layer porosity of the 3D sub domain did not change, indicating neither collapsing nor compaction of the catalyst layer structure. A lower rate of carbon corrosion and the presence of high ionomer loading are possibly the reasons for the catalyst layer structure to avoid collapsing and consequent thinning. The comparison of the pore size distribution between BOT and EOT 3D subdomain as shown in Figure 40 indicates that the pore sizes are relatively comparable and are within the expected variation as seen in the pore size distribution in Figure 39 (c) & (d).

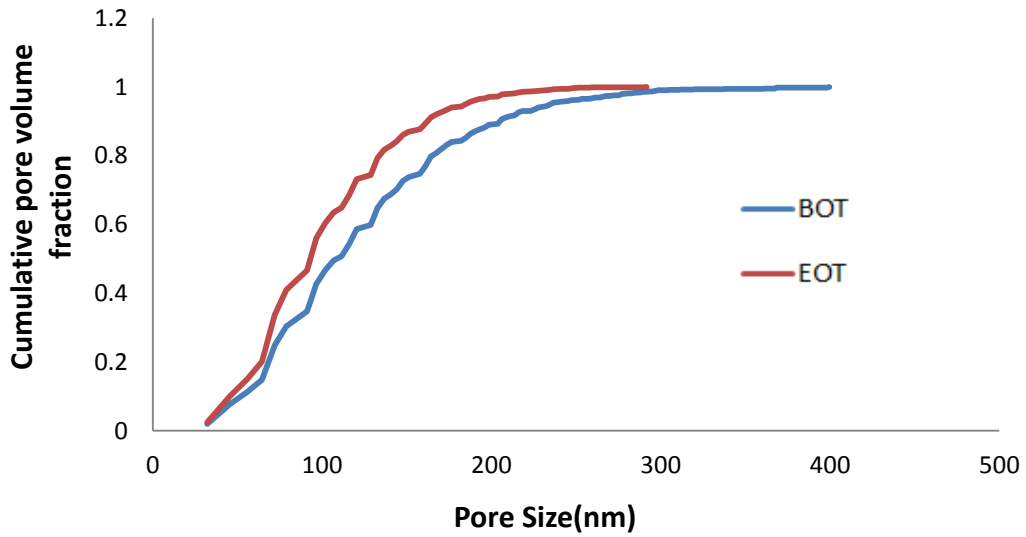


**Figure 40: Pore size distribution of BOT CCL and 1.2 V degraded EOT CCL with high ionomer loading.**

Numerical simulations were used to estimate the effective diffusivity in the catalyst layer sub domain. In the BOT and EOT sample, the effective diffusivity of oxygen and water vapor was found to be isotropic in all directions of flow, as shown in Table 7. It can be observed that the EOT diffusivity is comparable to BOT which is likely due to similar porosity.

	<b>D<sub>eff,O2</sub> (Effective diffusivity)</b> <b>10<sup>-5</sup> (m<sup>2</sup>/sec)</b>		<b>D<sub>eff,O2</sub>/D<sub>O2,air</sub></b> <b>(Relative diffusivity)</b>	
	BOT	EOT	BOT	EOT
Oxygen	0.3	0.3	0.13	0.13
Water Vapor	0.3	0.3	0.12	0.12

**Table 7: Diffusivity of oxygen and water vapor of a high ionomer CCL at BOT and high ionomer degraded EOT.**

A 66% loss in ECSA was measured for the degraded EOT CCL while Pt particle size at BOT and EOT CCL were comparable at 4.6 and 5.1 nm respectively; indicating ECSA loss is primarily due to Pt dissolution. The reduction in ECSA can lead to activation losses at EOT as seen in Figure 41. A 10% reduction in double layer capacitance was measured, indicating no significant carbon corrosion, and hence insignificant ohmic losses as seen in the fuel cell performance curve.

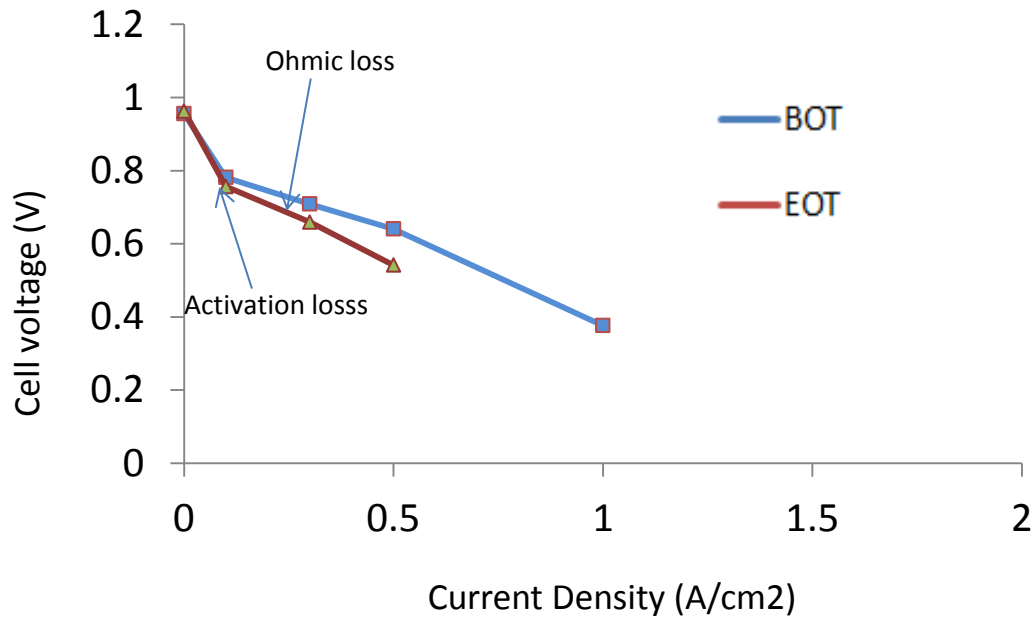


**Figure 41: A fuel cell polarization curve at high ionomer BOT MEA and high ionomer degraded EOT MEA showing the effect of reduction in CCL ECSA on the performance of the fuel cell.**

It can be observed that the porosity of high ionomer BOT and EOT CCL is ~35%, in comparison to low ionomer BOT and EOT CCL porosity of 53% and 34% respectively as seen in section 3.2.2. In addition, Pt particle size is significantly higher for low ionomer EOT CCL, indicating higher carbon corrosion, resulting in detachment of Pt particles and forming agglomerates. However, the ECSA loss is comparable for high and low ionomer CCL at EOT.

The effective diffusivity of oxygen and water vapor at high ionomer EOT CCL are an order of magnitude higher than at low ionomer EOT CCL in the through-plane direction which is likely due to larger pores, resulting in comparably lower mass transport losses for higher ionomer degraded CCL. Overall, higher ionomer content in the catalyst layer is seen to be favorable for maintaining the overall structure of the catalyst layer and helps in avoiding catalyst layer collapsing. However, 50 wt% might not necessarily be the optimized amount of required ionomer content and further study to determine this is desirable.

## Chapter 4. CONCLUSION

3D failure analysis of fuel cell electrodes was performed by using X-ray computed tomography. A multi-length scale approach was used to investigate crack growth, thinning, and structural change in the catalyst layer. This was accomplished by analyzing end of test MEAs and comparing to pristine, conditioned MEAs. At first; a baseline study on a conditioned BOT and voltage cycled EOT MEA is performed to qualify the multi-length scale approach XCT technique for 3D failure analysis of *in situ* degraded fuel cell electrodes. In addition, a parametric study using the same approach is performed to investigate the effect of changes in AST, composition, and morphology of the catalyst layer on the degradation process and failure modes.

A baseline MEA with high CL crack density on the cathode subjected to 4,700 voltage cycles at 1.3 V upper potential limits showed 57% thinning of the cathode catalyst layer accompanied by a five-fold increase in crack size, indicating widespread action of carbon corrosion. It was concluded that catalyst layer crack growth and thinning can occur in parallel with comparable dimensional rates, which can be attributed to a combination of carbon corrosion and erosion from water flooding. A complementary nano length scale analysis at the center of a cathode CL island showed a reduction in porosity from 54% at BOT to 23% at EOT with comparatively more isolated and larger pores in the degraded CCL. The combination of microscopic reduction in porosity and macroscopic reduction in thickness, uniquely observed through the present multi-length scale failure analysis approach, conclusively verifies collapsing of the catalyst layer structure as a result of severe carbon corrosion and associated loss of physical integrity. Diffusion simulations inside the reconstructed nano scale structure showed

dramatic reduction of the effective diffusivity of oxygen and water vapor in the degraded material. Thus, in terms of diffusive mass transport to and from the active sites, the reduced porosity and more isolated pores at EOT considerably outweighed the positive effect of the larger pore size. In contrast to BOT, the EOT effective diffusivities were found to be anisotropic in the three principal directions, with the through-plane diffusivities being substantially lower than in the in-plane direction. The low EOT fuel cell performance at high current densities as seen in the polarization curve can thus be attributed to mass transport losses in the degraded cathode. Moreover, examining the edge of a CL island at EOT revealed a porosity gradient from the edge to the center of the island, which indicates that catalyst layer structure collapse is more severe at the center of the CL island.

In addition, a novel image processing technique was developed for three-phase segmentation of the 3D reconstructed nano scale structure into pore, Pt/C, and ionomer dominated phases. The ionomer content was assumed to be retained during voltage cycling while the pore and Pt/C dominated phases were reduced in volume by collapsing and dissolution/corrosion, respectively. The ionomer dominated phase was observed to morph from a thin film structure at BOT to a dense structure with large, interconnected features of several hundred nanometers in diameter that dominate the remaining solid phase at EOT. The dense ionomer structure reduces the space available for reactant transport in the pore phase and electron conduction in the Pt/C phase and is thus expected to contribute to both mass transport and ohmic losses, as observed from the fuel cell performance at EOT. Particle isolation and agglomeration was observed in the remaining Pt/C dominated phase in the degraded structure, which is in good qualitative agreement with the high ECSA loss measured by CV and the increased Pt particle size measured by XRD, and can be attributed to extensive loss of carbon support combined with catalyst dissolution via Ostwald ripening and/or coalescence of Pt nanoparticles. Furthermore, carbon corrosion and Pt dissolution were observed to be

comparatively more severe at the membrane side of the catalyst layer, which further contributes to the high kinetic performance losses measured at EOT.

As part of the parametric study, a 1.2 V UPL cycled EOT MEA imaged at the micro scale showed that the total crack surface area in the catalyst layer increased by 1.6x in comparison to 5x at 1.3 V UPL. In addition, CCL thinning is 36% at 1.2 V UPL AST in comparison to 57% at 1.3 V UPL AST. Combined, these observations provide experimental evidence that carbon corrosion preferentially increases crack width and thinning at higher UPL. A complementary nano scale analysis of the 1.2 V UPL degraded CCL showed a 19% overall porosity reduction with evidence of partial collapsing of the structure and significant porosity gradient across the 3D sub-domain. Phase segmentation of the sub-domain revealed that the absence of platinum particles closer to the PEM interface due to platinum dissolution is most likely the cause for such gradient. A 40% increase in Pt particle size for the 1.2 V UPL degraded CCL in comparison to 44% for 1.3 V UPL degraded CCL confirms that Pt agglomeration is not significantly higher at higher UPL. Additionally, the diffusion simulations inside the reconstructed structure were significantly higher for 1.2 V degraded CCL compared to 1.3 V degraded CCL, resulting in better fuel cell performance. The solid phase segmentation of the catalyst layer structure showed evidence of calculated 37% ionomer volume fraction at 1.2 V degraded CCL in comparison to 51% at 1.3 V degraded CCL, indicating lower ohmic losses from electron resistance and lower mass transport losses for 1.2 V degraded CCL as seen from the fuel cell performance curve.

Moreover, a MEA with low cathode CL crack density subjected to 4,700 voltage cycles with 1.3 V UPL also showed 58% CL thinning and ~5 fold increase in crack surface area, identical to the high crack density EOT results. However, the overall total crack surface area for the high crack EOT CCL was significantly higher which can lead to water flooding, and consequently result in gas transport resistance. The same sample imaged at the nano scale showed a 34% overall decrease in porosity for the degraded CCL with more porous

structure at the membrane interface compared to GDL interface, which is most likely due to locally enhanced carbon corrosion and Pt migration, resulting in voltage loss due to slower ORR kinetics as seen in the fuel cell performance curve. In addition, a significant decrease in double layer capacitance was observed, indicating Pt/C surface area loss, and contributing to activation and ohmic losses. Additionally, the reduction in effective diffusivity of oxygen and water vapor contributed to mass transport losses. The overall porosity of a low crack BOT and EOT CCL is 11% higher compared to the high crack BOT and EOT CCL. Hence, the effective diffusivity of oxygen and water vapor at low crack BOT and EOT are an order of magnitude higher than at high crack BOT and EOT respectively, resulting in better fuel cell performance.

Furthermore, a MEA with HSAC cathode CL subjected to 4,700 voltage cycles with 1.2 V UPL showed 46% CL thinning and 5.4 fold increase in crack surface area which is significantly higher in comparison to 36% and 1.6x for similar AST degraded MEA with LSAC support, and is most likely due to larger catalyst anchor sites and less graphitic carbon support in the HSAC catalyst layer. Hence, it is experimentally evident that LSAC is a more stable catalyst support than HSAC at 1.2 V UPL AST. At the nano scale, it was observed that the overall porosity of degraded HSAC EOT subdomain was 23% lower compared to BOT subdomain, attributed to carbon corrosion. A 78% decrease in double layer capacitance and 89% loss in ECSA for the degraded EOT CCL were measured, indicating Pt/C surface area loss, and contributing to ohmic and activation losses as seen in the fuel cell performance curve. In contrast, the porosity of degraded LSAC EOT was 19% lower compared to LSAC BOT sub domain. Hence, Pt particle size and ECSA loss was significantly higher for HSAC EOT CCL, which indicates higher carbon corrosion rate resulting in detachment of Pt particles, and forming agglomerates. The simulated effective diffusivity in the CCL 3D sub domain for oxygen and water vapor at HSAC EOT CCL were an order of magnitude higher than at LSAC EOT CCL in the through-plane direction which

is most likely due to larger pores from carbon corrosion and Pt dissolution, resulting in comparably lower mass transport losses for HSAC EOT CCL.

Finally, a MEA with high ionomer loading (50 wt%) cathode CL subjected to 4,700 voltage cycles with 1.2 V UPL showed no significant CL thinning nor increase in crack surface area, whereas for low ionomer loading with identical AST, catalyst layer thinning was 36%, while the crack surface area increased by 1.6x. The overall porosity for the BOT and EOT sub domain was comparable at ~35% indicating no collapsing of catalyst layer structure, and no consequent thinning as seen by the micro scale analysis, hence mitigating thinning. This observation is in good agreement with only 10% decrease in double layer capacitance for the degraded EOT CCL, indicating no significant carbon corrosion and associated ohmic losses as seen in the fuel cell performance curve. The measured Pt particle size for low ionomer degraded EOT CCL was higher in comparison to high ionomer degraded EOT CCL, indicating relatively higher carbon corrosion, resulting in detachment of Pt particles, and contributing to comparatively higher fuel cell activation losses for low ionomer degraded EOT CCL. However, the ECSA loss is comparable for high and low ionomer CCL at EOT. The simulated effective diffusivity in the 3D sub domain for oxygen and water vapor for high ionomer EOT CCL are an order of magnitude higher than at low ionomer EOT CCL in the through-plane direction which is likely due to larger pores, resulting in comparably lower mass transport losses for higher ionomer degraded CCL at high current densities. In conclusion, use of higher ionomer loading in the catalyst layer is proven to help retain the BOT catalyst layer structure at EOT, and may be beneficial in preventing catalyst layer thinning after carefully identifying the optimal ionomer loading needed by repeating the presented work.

Overall, the 3D multi-length scale approach demonstrated in this work provided detailed and valuable insight into the failure mode of the cathode catalyst layer via micro scale analysis of crack growth and thinning combined with nano scale analysis of structural and compositional

features that cannot be observed through conventional diagnostic techniques. A comprehensive understanding of the complex failure modes in fuel cell electrodes was accomplished by examining a range of degraded electrodes. The new insight regarding the electrode structure enabled by this approach is expected to be useful for a wide range of failure analysis assignments from lab-scale research to field operation of fuel cells, and can also be extended to other electrochemical devices such as batteries and supercapacitors.

## References

- [1] M. . Mench, *Fuel cell Engines*. John Wiley & Sons, 2008.
- [2] J. Zhang, *PEM fuel cell electrocatalysts and catalyst layers: Fundamentals and applications*. Springer, 2008.
- [3] U.Bossell, "The birth of the Fuel Cell 1835–1845," Oberrohrdorf, 2000.
- [4] "H2 INFRASTRUCTURE." [Online]. Available: <https://cleanenergypartnership.de/en/faq/hydrogen-infrastructure/?scroll=true>. [Accessed: 16-Aug-2016].
- [5] J. B. Russell, "Investigation of the Effect of Catalyst Layer Composition on the Performance of PEM Fuel Cells Investigation of the Effect of Catalyst Layer Composition on the Performance of PEM Fuel Cells," Virginia Polytechnic Institute and State University, 2003.
- [6] M. K. Kadirov, A. Bosnjakovic, and S. Schlick, "Membrane-derived fluorinated radicals detected by electron spin resonance in UV-irradiated nation and Dow ionomers: Effect of counterions and H<sub>2</sub>O<sub>2</sub>," *J. Phys. Chem. B*, vol. 109, no. 16, pp. 7664–7670, 2005.
- [7] D. S. Hwang, C. H. Park, S. C. Yi, and Y. M. Lee, "Optimal catalyst layer structure of polymer electrolyte membrane fuel cell," *Int. J. Hydrogen Energy*, vol. 36, no. 16, pp. 9876–9885, 2011.
- [8] T. H. Yang, G. G. Park, W. Y. Lee, S. . Choi, and C. S. Kim, "Proceedings of First European PEFC Forum," 2001, p. 231.
- [9] M. Uchida, Y. Aoyama, N. Eda, and A. Ohta, "Investigation of the microstructure in the catalyst layer and effects of both perfluorosulfonate ionomer and PTFE-Loaded carbon

- on the catalyst layer of polymer electrolyte fuel cells,” *J. Electrochem. Soc.*, vol. 142, no. 12, pp. 4143–4149, 1995.
- [10] W. K. Epting, J. Gelb, and S. Litster, “Resolving the three-dimensional microstructure of polymer electrolyte fuel cell electrodes using nanometer-scale X-ray computed tomography,” *Adv. Funct. Mater.*, vol. 22, no. 3, pp. 555–560, 2012.
- [11] M. Kutz, “Environmentally Conscious Alternative Energy Production,” 2007, p. 78.
- [12] A. . Weber and J. Newman, “Effects of Microporous Layers in Polymer Electrolyte Fuel Cells,” *J. Electrochem. Soc.*, vol. 152, no. 4, p. A677, 2005.
- [13] A. Lindermeir, G. Rosenthal, U. Kunz, and U. Hoffmann, “On the question of MEA preparation for DMFCs,” *J. Power Sources*, vol. 129, no. 2, pp. 180–187, 2004.
- [14] W. Liu, L. Wan, J. Liu, M. Zhao, and Z. Zou, “Performance improvement of the open-cathode proton exchange membrane fuel cell by optimizing membrane electrode assemblies,” *Int. J. Hydrogen Energy*, vol. 40, no. 22, pp. 7159–7167, 2015.
- [15] C. H. Hsu and C. C. Wan, “An innovative process for PEMFC electrodes using the expansion of Nafion film,” *J. Power Sources*, vol. 115, no. 2, pp. 268–273, 2003.
- [16] H. P. Brack, M. Slaski, L. Gubler, G. G. Scherer, S. Alkan, and A. Wokaun, “Characterisation of fuel cell membranes as a function of drying by means of contact angle measurements,” *Fuel Cells*, vol. 4, no. 3, pp. 141–146, 2004.
- [17] A. . Appleby, *Fuel cell systems*. New York: Plenum press, 1993.
- [18] “Multi-Year Research, Development, and Demonstration Plan,” 2016.
- [19] J. Wu, X. Z. Yuan, J. J. Martin, H. Wang, J. Zhang, J. Shen, S. Wu, and W. Merida, “A review of PEM fuel cell durability: Degradation mechanisms and mitigation strategies,” *J. Power Sources*, vol. 184, no. 1, pp. 104–119, 2008.
- [20] H. Uchida, M. Aoki, and M. Watanabe, “New evaluation method for degradation rate of polymer electrolytes,” *ECS Trans.*, vol. 3, no. 1, pp. 485–492, 2006.

- [21] J. Xie, D. L. Wood, D. M. Wayne, T. A. Zawodzinski, P. Atanassov, and R. L. Borup, "Durability of PEFCs at High Humidity Conditions," *J. Electrochem. Soc.*, vol. 152, no. 1, p. A104, 2005.
- [22] S. Zhang, X. Z. Yuan, J. N. C. Hin, H. Wang, J. Wu, K. A. Friedrich, and M. Schulze, "Effects of open-circuit operation on membrane and catalyst layer degradation in proton exchange membrane fuel cells," *J. Power Sources*, vol. 195, no. 4, pp. 1142–1148, 2010.
- [23] H. R. Colón-Mercado and B. N. Popov, "Stability of platinum based alloy cathode catalysts in PEM fuel cells," *J. Power Sources*, vol. 155, no. 2, pp. 253–263, 2006.
- [24] T. W. Hansen, A. T. Delariva, S. R. Challa, and A. K. Datye, "Sintering of catalytic nanoparticles: Particle migration or ostwald ripening?," *Acc. Chem. Res.*, vol. 46, no. 8, pp. 1720–1730, 2013.
- [25] N. Macauley, K. H. Wong, M. Watson, and E. Kjeang, "Favorable effect of in-situ generated platinum in the membrane on fuel cell membrane durability," *J. Power Sources*, vol. 299, pp. 139–148, 2015.
- [26] K. Kinoshita, *Carbon, Electrochemical and Physicochemical Properties*. New York: John Wiley & Sons, 1988.
- [27] K. H. Kangasniemi, D. a. Condit, and T. D. Jarvi, "Characterization of Vulcan Electrochemically Oxidized under Simulated PEM Fuel Cell Conditions," *J. Electrochem. Soc.*, vol. 151, no. 4, pp. E125–E132, 2004.
- [28] A. Taniguchi, T. Akita, K. Yasuda, and Y. Miyazaki, "Analysis of degradation in PEMFC caused by cell reversal during air starvation," *Int. J. Hydrogen Energy*, vol. 33, no. 9, pp. 2323–2329, 2008.
- [29] H. Schulenburg and B. Schwanitz, "3D imaging of catalyst support corrosion in polymer electrolyte fuel cells," *J. Phys. Chem. C*, vol. 115, pp. 14236–14243, 2011.
- [30] A. P. Hitchcock, V. Berejnov, V. Lee, M. West, V. Colbow, M. Dutta, and S. Wessel, "Carbon corrosion of proton exchange membrane fuel cell catalyst layers studied by

- scanning transmission X-ray microscopy,” *J. Power Sources*, vol. 266, pp. 66–78, Nov. 2014.
- [31] F. Rong, C. Huang, Z. S. Liu, D. Song, and Q. Wang, “Microstructure changes in the catalyst layers of PEM fuel cells induced by load cycling. Part I. Mechanical model,” *J. Power Sources*, vol. 175, no. 2, pp. 699–711, 2008.
- [32] S. Kundu, M. W. Fowler, L. C. Simon, and S. Grot, “Morphological features (defects) in fuel cell membrane electrode assemblies,” *J. Power Sources*, vol. 157, no. 2, pp. 650–656, 2006.
- [33] S. Wessel and D. Harvey, “2013 Annual Merit Review Proceedings: Fuel Cells, ProjectID#FC049,” in *2013 Annual Merit Review Proceedings: Fuel Cells, ProjectID#FC049*, 2013.
- [34] F. Migliardini and P. Corbo, “CV and EIS study of hydrogen fuel cell durability in automotive applications,” *Int. J. Electrochem. Sci.*, vol. 8, no. 9, pp. 11033–11047, 2013.
- [35] K. Lin, Y. Lu, S. Du, X. Li, and H. Dong, “The effect of active screen plasma treatment conditions on the growth and performance of Pt nanowire catalyst layer in DMFCs,” *Int. J. Hydrogen Energy*, vol. 41, no. 18, pp. 7622–7630, 2016.
- [36] S. . Chan, K. . Khor, and Z. . Xia, “A complete polarization model of a solid oxide fuel cell and its sensitivity to the change of cell component thickness,” *J. Power Sources*, vol. 93, no. 1–2, pp. 130–140, 2001.
- [37] T. Ous and C. Arcoumanis, “Degradation aspects of water formation and transport in Proton Exchange Membrane Fuel Cell: A review,” *J. Power Sources*, vol. 240, pp. 558–582, 2013.
- [38] J. P. Owejan, T. A. Trabold, and M. M. Mench, “Oxygen transport resistance correlated to liquid water saturation in the gas diffusion layer of PEM fuel cells,” *Int. J. Heat Mass Transf.*, vol. 71, pp. 585–592, 2014.
- [39] M. S. Çögenli, S. Mukerjee, and A. B. Yurtcan, “Membrane electrode assembly with ultra

- low platinum loading for cathode electrode of PEM fuel cell by using sputter deposition,” *Fuel Cells*, vol. 15, no. 2, pp. 288–297, 2015.
- [40] M. Eikerling and A. . Kornyshev, “Electrochemical impedance of the cathode catalyst layer in polymer electrolyte fuel cells,” *J. Electroanal. Chem.*, vol. 475, no. 2, pp. 107–123, 1999.
- [41] R. Chebbi, A. Beicha, W. R. W. Daud, and R. Zaaouch, “Surface analysis for catalyst layer (PT/PTFE/C) and diffusion layer (PTFE/C) for proton exchange membrane fuel cells systems (PEMFCs),” *Appl. Surf. Sci.*, vol. 255, no. 12, pp. 6367–6371, 2009.
- [42] F. E. Hizir, S. O. Ural, E. C. Kumbur, and M. M. Mench, “Characterization of interfacial morphology in polymer electrolyte fuel cells: Micro-porous layer and catalyst layer surfaces,” *J. Power Sources*, vol. 195, no. 11, pp. 3463–3471, 2010.
- [43] T. Fuller, H. . Gasteiger, S. Cleghorn, V. Ramani, T. Zhao, T. . Nguyen, A. Haug, C. Bock, C. Lamy, and K. Ota, “Proton exchange membrane fuel cells 7,” *ECS Trans.*, vol. 11, no. 1, p. 1141, 2007.
- [44] N. Hodnik, M. Zorko, B. Jozinovi, M. Bele, G. Dra, S. Hovevar, and M. Gaberek, “Severe accelerated degradation of PEMFC platinum catalyst: A thin film IL-SEM study,” *Electrochem. commun.*, vol. 30, pp. 75–78, 2013.
- [45] J. Kim, J. Lee, and Y. Tak, “Relationship between carbon corrosion and positive electrode potential in a proton-exchange membrane fuel cell during start/stop operation,” *J. Power Sources*, vol. 192, no. 2, pp. 674–678, 2009.
- [46] R. F. Egerton, P. Li, and M. Malac, “Radiation damage in the TEM and SEM,” *Micron*, vol. 35, no. 6, pp. 399–409, 2004.
- [47] B. Wu, M. Zhao, W. Shi, W. Liu, J. Liu, D. Xing, Y. Yao, Z. Hou, P. Ming, J. Gu, and Z. Zou, “The degradation study of Nafion/PTFE composite membrane in PEM fuel cell under accelerated stress tests,” *Int. J. Hydrogen Energy*, vol. 39, no. 26, pp. 14381–14390, 2014.

- [48] a. S. Aricò, "Analysis of the Electrochemical Characteristics of a Direct Methanol Fuel Cell Based on a Pt-Ru/C Anode Catalyst," *J. Electrochem. Soc.*, vol. 143, no. 12, p. 3950, 1996.
- [49] S. S Manickam and J. R. McCutcheon, "Characterization of polymeric nonwovens using porosimetry, porometry and X-ray computed tomography," *J. Memb. Sci.*, vol. 407–408, pp. 108–115, 2012.
- [50] H. R. Q. Jhong, F. R. Brushett, and P. J. A. Kenis, "The effects of catalyst layer deposition methodology on electrode performance," *Adv. Energy Mater.*, vol. 3, no. 5, pp. 589–599, 2013.
- [51] R. T. White, M. Najm, M. Dutta, F. P. Orfino, and E. Kjeang, "Communication—Effect of Micro-XCT X-ray Exposure on the Performance of Polymer Electrolyte Fuel Cells," *J. Electrochem. Soc.*, vol. 163, no. 10, pp. F1206–F1208, 2016.
- [52] J. Roth, J. Eller, and F. N. Buchi, "Effects of Synchrotron Radiation on Fuel Cell Materials," *J. Electrochem. Soc.*, vol. 159, no. 8, pp. F449–F455, 2012.
- [53] A. Schneider, C. Wieser, J. Roth, and L. Helfen, "Impact of synchrotron radiation on fuel cell operation in imaging experiments," *J. Power Sources*, vol. 195, no. 19, pp. 6349–6355, 2010.
- [54] Z. Xu, Z. Qi, C. He, and A. Kaufman, "Combined activation methods for proton-exchange membrane fuel cells," *J. Power Sources*, vol. 156, no. 2, pp. 315–320, 2006.
- [55] J. F. Barrett and N. Keat, "Artifacts in CT: recognition and avoidance.," *Radiographics*, vol. 24, no. 6, pp. 1679–91, 2004.
- [56] M. Andisheh-Tadbir, F. Orfino, and E. Kjeang, "Three-dimensional, phase distinguished nano-scale X-ray computed tomography of micro-porous layers for fuel cells," *J. Power Sources*, vol. 310, pp. 61–69, 2015.
- [57] M. El Hannach and E. Kjeang, "Stochastic Microstructural Modeling of PEFC Gas Diffusion Media," *J. Electrochem. Soc.*, vol. 161, no. 9, pp. F951–F960, 2014.

- [58] M. El Hannach, R. Singh, N. Djilali, and E. Kjeang, "Micro-porous layer stochastic reconstruction and transport parameter determination," *J. Power Sources*, vol. 282, pp. 58–64, 2015.
- [59] K. J. Lange, P. C. Sui, and N. Djilali, "Using an ILU/deflation preconditioner for simulation of a pemfuel cell cathode catalyst layer," *Commun. Comput. Phys.*, vol. 14, no. 3, pp. 537–573, 2013.
- [60] K. Lange, P. Sui, and N. Djilali, "Pore scale simulation of transport and electrochemical reactions in reconstructed PEMFC catalyst layers," *J. Electrochem. Soc.*, vol. 157, no. 10, p. B1434, 2010.
- [61] a. P. Young, J. Stumper, S. Knights, and E. Gyenge, "Ionomer Degradation in Polymer Electrolyte Membrane Fuel Cells," *J. Electrochem. Soc.*, vol. 157, no. 3, p. B425, 2010.
- [62] D. C. Huang, P. J. Yu, F. J. Liu, S. L. Huang, K. L. Hsueh, Y. C. Chen, C. H. Wu, W. C. Chang, and F. H. Tsau, "Effect of dispersion solvent in catalyst ink on proton exchange membrane fuel cell performance," *Int. J. Electrochem. Sci.*, vol. 6, no. 7, pp. 2551–2565, 2011.
- [63] A. P. Young, J. Stumper, and E. Gyenge, "Characterizing the Structural Degradation in a PEMFC Cathode Catalyst Layer: Carbon Corrosion," *J. Electrochem. Soc.*, vol. 156, no. 8, pp. B913–B922, 2009.
- [64] S. Basu, *Recent Trends in Fuel Cell Science and Technology*. New delhi: Springer, 2007.
- [65] P. K. Das, X. Li, and Z. S. Liu, "A three-dimensional agglomerate model for the cathode catalyst layer of PEM fuel cells," *J. Power Sources*, vol. 179, no. 1, pp. 186–199, 2008.
- [66] C. Bois, A. Blayo, D. Chaussy, R. Vincent, A. G. Mercier, and C. Nayoze, "Catalyst layers for PEMFC manufactured by flexography printing process: Performances and structure," *Fuel Cells*, vol. 12, no. 2, pp. 199–211, 2012.
- [67] A. Mehmood, M. G. An, and H. Y. Ha, "Physical degradation of cathode catalyst layer: A major contributor to accelerated water flooding in long-term operation of DMFCs," *Appl.*

*Energy*, vol. 129, pp. 346–353, 2014.

- [68] Y. Matsui, T. Suzuki, P. Deevanhxay, S. Tsushima, and S. Hirai, “Crack Generation in Catalyst Layer and Micro Porous Layer by Wet-Dry Cycles and its Impact on PEMFC Performance,” *Asme*, vol. 18099, p. V001T01A005, 2013.
- [69] J. Melorose, R. Perroy, and S. Careas, “Accelerated testing of carbon corrosion and membrane degradation in PEM fuel cells,” *Statew. Agric. L. Use Baseline 2015*, vol. 1, no. 2, pp. 1003–1010, 2015.
- [70] A. Patel, K. Artyushkova, P. Atanassov, A. P. Young, M. Dutta, Z. Ahmad, V. Colbow, S. Wessel, and S. Ye, “Structural and morphological properties of carbon support: Effect on catalyst degradation,” *ECS Trans.*, vol. 33, no. 1, pp. 425–431, 2010.